Publ. Astron. Soc. Japan (2017) 00(0), 1–46
doi: 10.1093/pasj/xxx000

Diffuse X-Ray Sky in the Galactic Center

Katsuji KOYAMA

Department of Physics, Graduate School of Science, Kyoto University, Sakyo-ku, Kyoto, 606-8502, Japan

*E-mail: koyama@cr.scphys.kyoto-u.ac.jp

Received 2017 January 25; Accepted 2017 June 9

Abstract

The Galactic Diffuse X-ray Emission (GDXE) in the Milky Way Galaxy is spatially and spectrally decomposed into the Galactic Center X-ray Emission (GCXE), the Galactic Ridge X-ray Emission (GRXE) and the Galactic Bulge X-ray Emission (GBXE). The X-ray spectra of the GDXE are characterized by the strong K-shell lines of the highly ionized atoms, the brightest are the K-shell transition (principal quantum number transition of $n = 2 \rightarrow 1$) of neutral iron (Fe I-Kα), He-like iron (Fe XXV-Heα) and He-like sulfur (S XV-Heα) lines. Accordingly, the GDXE is composed of a high-temperature plasma of $\sim$7 keV (HTP) and a low-temperature plasma of $\sim$1 keV (LTP), which emit the Fe XXV-Heα and S XV-Heα lines, respectively. The Fe I-Kα line is emitted from nearly neutral irons, and hence the third component of the GDXE is a Cool Gas (CG). The Fe I-Kα distribution in the GCXE region is clumpy (Fe I-Kα clump), associated with giant molecular cloud (MC) complexes, Sagittarius A, B, C, D and E, in the central molecular zone. The origin of the Fe I-Kα clumps is the fluorescence and Thomson scattering from the MCs irradiated by past big flares of the super massive black hole Sagittarius A*. The scale heights and equivalent widths of the Fe I-Kα, Fe XXV-Heα and Fe XXVI-Lyα ($n = 2 \rightarrow 1$ transition of H-like iron) lines are different among the GCXE, GBXE and GRXE. Therefore the structure and origin are separately examined. This paper overviews the research history and the present understandings of the GDXE, in particular focus on the origin of the HTP and CG in the GCXE.

Key words: ISM:supernova remnants — Galaxy:center — X-ray: diffuse background — X-ray: ISM

Contents

1 Introduction

The center of our Milky Way Galaxy (the Galactic Center: GC) and Sagittarius A* (Sgr A*) are the nearest galactic center and the Super Massive Black hole (SMBH) from the Earth, and hence are unique and ideal laboratories for the study of various astrophysical processes. Therefore, many observations and theoretical works have been made in the wide band of electromagnetic radiations. The recent reviews of the GC and Sgr A* are found in Genzel et al. (2010) and Morris et al. (2012), which focused mainly on the infrared and radio bands, respectively. This paper, therefore, focuses on the review of the X-ray sky near the GC and related activities of Sgr A*.

The X-ray astronomy was opened by the discovery of a bright extraterrestrial X-ray source with the sounding rocket (Giacconi et al. 1962). This source is now known as Sco X-1, the brightest Galactic X-ray star. Diffuse X-ray emissions, later called the Cosmic X-ray Background (CXB), were also found. After many studies and debates, the origin of the CXB, at least in the energy range below $\sim$10 keV, has come to a common consensus that the CXB is an integrated emission of the extragalactic sources such as Active Galactic Nuclei (AGN) and active galaxies.

The first X-ray satellite, Uhuru discovered many point-like sources, majority of the bright sources are concentrated in the Galactic plane (e.g., see the fourth Uhuru catalog; Forman et al. 1978). Most of them are close binaries of neutron star (NS) or black hole (BH) with normal stars, and are named the X-ray Binary (XB). Sco X-1 is the brightest XB observed from the Earth. In addition to the CXB and XBs, diffuse X-rays of the Galactic origin were found with Uhuru, Ariel 5 and HEAO-1. These emissions extended to a high Galactic latitude of the scale height (SH) of $\gtrsim$500 pc – 1.5 kpc. Since the surface brightness is very faint, less than $\sim$10 % of the CXB, any quantitative study has been limited, which places this emission out of the scope of this review. Soon after, the Galactic diffuse X-ray emission with the surface brightness nearly or larger than the CXB, has been discovered. This emission is more concentrated toward the Galactic plane, with the SH of less than a few 100 pc (see section 2). This review specifies this X-ray emission as the Galactic Diffuse X-ray Emission (GDXE).

In this review, the transition lines from the first excited to the ground states (the principle quantum number $n = 2 \rightarrow 1$) in the neutral or low ionization atoms, He-like (ions with two electrons), and H-like (ions with one electron) atoms are designated as the Kα, Heα and Lyα lines, respectively. Likewise, the transition lines from the second excited to the ground states (the principle quantum number $n = 3 \rightarrow 1$) are the Kβ, Heβ and Lyβ lines, while the transitions from the third excited to the ground states (the principle quantum number $n = 4 \rightarrow 1$) are the Heγ and Lyγ lines [1]. The Equivalent Width (EW) and Scale Height (SH) of these iron lines are expressed as $\mathrm{EW}_{6.4}$, $\mathrm{EW}_{6.7}$, $\mathrm{EW}_{6.97}$, $\mathrm{SH}_{6.4}$, $\mathrm{SH}_{6.7}$, and $\mathrm{SH}_{6.97}$, where the subscript is the energy of the lines. For brevity and / or in the case that the Fe I-Kα, Fe XXV-Heα and Fe XXVI-Lyα lines are not resolved, the notation of Fe-Kα with the EW of $\mathrm{EW}_{\mathrm{Fe-K}}$ ($\mathrm{EW}_{6.4}$, $\mathrm{EW}_{6.7}$ and $\mathrm{EW}_{6.97}$) and the SH of $\mathrm{SH}_{\mathrm{Fe-K}}$ ($\mathrm{SH}_{6.4}$, $\mathrm{SH}_{6.7}$ and $\mathrm{SH}_{6.97}$) are used. These and the other abbreviations and symbols frequently used in this review are summarized in table 1.

After long and extensive studies, the GDXE is now decomposed to three spatial components, the Galactic Center X-ray Emission (GCXE), the Galactic Bulge X-ray Emission (GBXE) and the Galactic Ridge X-ray Emission (GRXE). The GDXE exhibits various atomic lines, the brightest are the K-shell transition lines from the He-like Fe (Fe XXV-Heα), He-like S (S XV-Heα) and from the neutral or low ionized Fe (Fe I-Kα). These atomic lines are emitted from a High-temperature Plasma (HTP) and a Low-temperature Plasma (LTP) and an X-ray re-emitting Cool Gas (CG), respectively.

This paper reviews the early studies of the GDXE, then moves on the reviews of the separate study of the GCXE, GBXE and GRXE. The reviews gradually focus on the origins and structures of the HTP and CG in the GCXE and its implications. The GBXE and GRXE are also reviewed, because the origin and structure of the GCXE are closely related to those of the GBXE and GRXE. Since the EW and SH of the Fe-Kα lines are significantly different among the GCXE, GBXE and GRXE, the long-standing debate, the origin and structure of the GDXE, are re-examined by the separate, but coordinated studies on the GCXE, GBXE and GRXE.

The contents are organized as follows. The early results taken before Chandra, XMM-Newton and Suzaku on the GRXE are reviewed in section 2. The structure of the GRXE and its possible origin are discussed in section 2.1. Discoveries of new components, the GCXE and GBXE, and their characteristics are given in sections 2.2 and 2.3, respectively.

Section 3 overviews the recent observational results of the GDXE made with Chandra, XMM-Newton and Suzaku. Section 3.1 gives the global spatial structure of the Fe-Kα, S XV-Heα and S XVI-Lyα lines in the GDXE, along and perpendicular to the Galactic plane, which leads to the decomposition of the GDXE into the GCXE, GBXE and GRXE. Section 3.2 reports the X-ray spectra and luminosity of the GCXE, GBXE and GRXE. The spectra are significantly different among these components, and hence verify the decomposition of the GDXE into these components. Section 3.3 discusses the characteristics of the HTP and CG in the central region of the GCXE, based mainly on the observed flux of Fe-Kα and $\mathrm{EW}_{\mathrm{Fe-K}}$.

Section 4 reviews the local enhancements of the HTP and LTP in the GCXE obtained mainly with Suzaku. Sections 4.1 is devoted to the description of young Supernova Remnants

[1] In some of the reference papers, notation of Kα, β, γ is used instead of Heα, β, γ or Lyα, β, γ.

Table 1. Abbreviations and Symbols frequently used in this text.

Symbol, Acronym	Explanation
GC	Galactic Center, The center of our Milky Way Galaxy
GDXE	Galactic Diffuse X-ray Emission which is composed of GCXE, GBXE and GRXE
GCXE	Galactic Center X-ray Emission
GBXE	Galactic Bulge X-ray Emission
GRXE	Galactic Ridge X-ray Emission
CXB	Cosmic X-ray Background
NXB	Non X-ray Background, the cosmic ray induced background
Fe I-Kα	$n = 2 \rightarrow 1$ transition of the neutral or low ionization iron at the energy of $\sim$6.40 keV
Fe I-Kβ	$n = 3 \rightarrow 1$ transition of the neutral or low ionization iron at the energy of $\sim$7.06 keV
Fe XXV-Heα	$n = 2 \rightarrow 1$ transition of the He-like (two electrons are left) iron at the energy of $\sim$6.68 keV
Fe XXV-Heβ	$n = 3 \rightarrow 1$ transition of the He-like iron at the energy of $\sim$7.88 keV
Fe XXVI-Lyα	$n = 2 \rightarrow 1$ transition of the H-like (one electron is left) iron at the energy of $\sim$6.97 keV
Fe-Kα	$n = 2 \rightarrow 1$ transition of the neutral, He-like and H-like iron
Ni XXVII-Heα	$n = 2 \rightarrow 1$ transition of the He-like nickel at the energy of $\sim$7.80 keV
Si XVIII-Heα	$n = 2 \rightarrow 1$ transition of the He-like silicon at the energy of $\sim$1.86 keV
Si XVIV-Lyα	$n = 2 \rightarrow 1$ transition of the H-like silicon at the energy of $\sim$2.00 keV
S XV-Heα	$n = 2 \rightarrow 1$ transition of the He-like sulfur at the energy of $\sim$2.46 keV
S XVI-Lyα	$n = 2 \rightarrow 1$ transition of the H-like sulfur at the energy of $\sim$2.62 keV
EW	Equivalent Width, the flux ratio of the line to the continuum emission.
$\mathrm{EW}_{6.4}$	Equivalent width of the 6.4 keV line, Fe I-Kα line
$\mathrm{EW}_{6.7}$	Equivalent width of the 6.7 keV line, Fe XXV-Heα line
$\mathrm{EW}_{6.97}$	Equivalent width of the 6.97 keV line, Fe XXVI-Lyα line
$\mathrm{EW}_{\mathrm{Fe-K}}$	Equivalent width of the iron K-shell line, the sum of $\mathrm{EW}_{6.4}$, $\mathrm{EW}_{6.7}$ and $\mathrm{EW}_{6.97}$
SH	Scale Height, the longitude distance from the Galactic plane where the flux falls by a factor of $1/e$.
$\mathrm{SH}_{6.4}$	Scale Height of the 6.4 keV line, Fe I-Kα line
$\mathrm{SH}_{6.7}$	Scale Height of the 6.7 keV line, Fe XXV-Heα line
$\mathrm{SH}_{6.97}$	Scale Height of the 6.97 keV line, Fe XXVI-Lyα line
$\mathrm{SH}_{\mathrm{Fe-K}}$	Scale height of the iron K-shell line, the mean of $\mathrm{SH}_{6.4}$, $\mathrm{SH}_{6.7}$ and $\mathrm{SH}_{6.97}$
HTP	High temperature Plasma (kT $\sim$6–7 keV) in the GDXE
LTP	Low temperature Plasma (kT $\sim$0.8–1 keV) in the GDXE
CG	Cool Gas in the GDXE which emits the K-shell lines of neutral atoms
MC	Molecular Cloud
CMZ	Central Molecular Zone
XRN	X-ray Reflection Nenula: Fluorescence/Thomson scattered X-ray nebula by the flare of Sgr A*.
NTF	Non Thermal Filaments, mostly radio source
PWN	Pulsar Wind Nebula as a non thermal X-ray source
CV	Cataclysmic Variable, Binary of normal star and white dwarf
mCV	Magnetized CV which are intermediate polar, polar and symbiotic stars
non-mCV	Non magnetized CV, or dwarf nova
AB	Coronal Active close Binary of low mass star like RS CVn and Algol types.
XAS	X-ray Active Stars. The main components are mCV, non-mCV and AB
SMD	Stellar Mass Distribution made from the infrared flux
SMBH	Super Massive Black Hole
SN	Supernova
SNR	Supernova Remnant
LECR	Low Energy Cosmic Ray
LECRe	Low Energy Cosmic Ray electrons, typical energy is $\sim$ a few 10 keV
LECRp	Low Energy Cosmic Ray protons, typical energy is $\sim$ a few 10 MeV
CIE	Collisional Ionization Equilibrium
IP	Ionizing Plasma (Non Equilibrium Ionization: NEI)
RP	Recombining Plasma (Non Equilibrium Ionization: NEI)
XLF	Cumulative X-ray Luminosity as a Function of point source luminosity
FIM	Flux Integration Method of the point sources
SAM	Spectrum Accumulation Method of the point sources

(SNR) or candidates, which emit strong Fe XXV-Heα lines, while section 4.2 reviews the soft X-ray spots with strong S XV-Heα lines, which are intermediate aged SNRs or candidates.

Section 5 reviews the Fe I-Kα line emitting component, the CG components observed mainly with Suzaku, Chandra and XMM-Newton. The emission mechanisms of the Fe I-Kα line and resultant $\mathrm{EW}_{6.4}$ are given in section 5.1. Section 5.2 is devoted to the X-ray Reflection Nebula (XRN), which is a source of fluorescence and scattered X-ray by past activities (flares) of Sgr A*. Section 5.3 concerns the other Fe I-Kα clumps, which may be unrelated to the flares of Sgr A*.

Section 6 summarizes small size diffuse X-ray emissions, found mainly with Chandra and XMM-Newton in the central GCXE region (section 6.1) and outer GCXE region (section 6.2). These are mostly power-law (non-thermal) X-ray filaments of length $\lesssim$ a few $10''$.

Section 7 presents activity history of Sgr A*. The past activities are suggested by the XRNe, a Recombining Plasma (RP) and outflows or jet-like structures pointing to Sgr A*, which are given in sections 7.1, 7.2 and 7.3, respectively.

Sections 8 specified the methodology to the origin of the GDXE, together with the summary of the EW_{Fe-K} and SH_{Fe-K} of the magnetic Cataclysmic Variables (mCVs), non magnetic Cataclysmic Variables (non-mCVs) or dwarf nova and coronal Active Binaries (ABs). The spectral fit of the GCXE, GBXE and GRXE by a combination of the mCVs, non-mCVs (DN) and ABs spectra are presented.

Section 9 discuss on the origin of the GBXE, GRXE and GCXE based on the results given in section 8. The origin of the GDXE are separately discussed in section 9.1 (GBXE) section 9.2 (GRXE) and section 9.3 (GCXE).

In the reference papers, the physical parameters, luminosity, plasma size and the other physical parameters, have been derived under the assumption of the GC distance of 8.5 or 8.0 kpc. This review, therefore unifies the physical parameters assuming the GC distance to be 8.0 kpc. Then, the angular size and the X-ray flux of $1'$ and 10^{-12} erg cm^{-2} s^{-1} correspond to the physical size of 2.33 pc and X-ray luminosity of 7.63×10^{33} erg s^{-1}, respectively. The cited errors in the reference papers were either 90 %, or $1\,\sigma$ confidence levels depending on the physical parameters and / or authors. This paper unifies the error to be 90 % confidence level, unless otherwise stated. The metallic abundances of the solar photosphere are those in Anders and Grevesse (1989).

2 Early Studies of the Galactic Diffuse X-Ray Emission (GDXE)

This section reports the start lines in the studies of the GDXE, the early results of the GRXE (section 2.1), GCXE (section 2.2) and GBXE (section 2.3), using the results taken before the era of Chandra, XMM-Newton and Suzaku. In these sub-sections, the contents are not exactly in the chronological orders, but are organized in subject-oriented styles.

2.1 The Galactic Ridge X-Ray Emission (GRXE)

In this section, the history of the GRXE survey is reported. Section 2.1.1 is that oriented to the point source fraction of the GRXE, while section 2.1.2 is oriented to the GRXE spectrum. The discovery history of non-thermal emissions is given in section 2.1.3.

2.1.1 The GRXE and Point Sources

The global structure of the GRXE is first reported with HEAO-1 by Worrall et al. (1982). It is a diffuse X-ray emission in the 2 – 10 keV band along the Galactic plane. Due to the large beam size of $3^\circ \times 1.^\circ 5$ (FWHM), the regions free from contamination of bright XBs, are limited to be $l \gtrsim 50^\circ$ ($\gtrsim 7$ kpc from Sgr A*). Nevertheless, the overall profile is estimated to be an exponential function of the e-folding radius of ~ 3.5 kpc with the half thickness (SH) of ~ 240 pc. Extrapolating the flux distribution to a radius of $\lesssim 7$ kpc, the total luminosity of the GRXE is estimated to be $\sim 10^{38}$ erg s^{-1} (2 – 10 keV). They proposed that most probable origin of the GRXE is an integrated emission of many unresolved faint discrete sources.

Worrall & Marshall (1983) compared the results of Worrall et al. (1982) to the number density of serendipitous sources in the Galactic plane discovered with the Imaging Proportional Counter (IPC) on board the Einstein Observatory. They concluded that X-ray point sources with the 2 – 10 keV band luminosity of $8 \times 10^{32} - 3 \times 10^{34}$ erg s^{-1} are not dominant contributors to the GRXE. In particular, contributions of Be/neutron star systems such as X Persei would be minor, because these systems have the 2 – 10 keV band luminosity of $\sim 10^{33}$ erg s^{-1}, and have smaller SH than the GRXE. Lower luminosity stellar systems of $\leq 4 \times 10^{32}$ erg s^{-1} are likely major contributors to the GRXE. They predicted that coronal Active Binaries (ABs) and Cataclysmic Variables (CVs) with the 2 – 10 keV band luminosity of $2 \times 10^{30} - 4 \times 10^{32}$ erg s^{-1} may contribute 43 ± 18 % of the GRXE.

Hertz & Grindlay (1984) found 71 point-like sources with the IPC in the regions of the Galactic latitude of $|b| \leq 15^\circ$. In the sample, ∼46 %, ∼31 % and ∼23 % are coronal emission from non-degenerate stars, extragalactic sources and unidentified Galactic sources, respectively. The approximated number density of the Galactic sources is consistent with Cataclysmic Variables (CVs) and other accreting white dwarfs. Faint Galactic plane sources are concentrated toward the Galactic bulge, and have a flatter number-flux relation than that at higher Galactic latitude and longitude.

Warwick et al. (1985) observed the inner GRXE with EXOSAT having a small beam size of $0.^\circ 75 \times 0.^\circ 75$ (FWHM). The flux distribution (2 – 6 keV) of the unresolved emissions extends to the inner Galactic plane in the longitude of $|l| \lesssim 40^\circ$. They found very small SH of $|b| \lesssim 1^\circ$. This small SH excludes old population stars as the origin of the GRXE. The overall profile of the GRXE is exponential shape with the e-folding l and b of ~ 3.5 kpc and of ~ 100 pc, respectively. The total luminosity is $\sim 10^{38}$ erg s^{-1}, consistent with the results of Worrall et al. (1982).

With RXTE, Revnivtsev et al. (2006a) made the GRXE profile in the 3 – 20 keV band along the Galactic plane of $|l| \lesssim 100^\circ$, and perpendicular to the plane of $|b| \lesssim 6^\circ$ at $|l| \lesssim 4^\circ$. The SH at $l = 20^\circ$ is ∼130 eV. They found the longitude profiles are similar to the infrared surface brightness distribution. Revnivtsev et al. (2006b) further investigated the RXTE data of the inner Galaxy ($|l| \lesssim 25^\circ$) and the Galactic ridge emission up to $|l| \lesssim 120^\circ$. In

order to reduce possible contamination of bright point-sources (XBs) to the GRXE, they used the Fe-Kα (6.7 keV) line, instead of the continuum (3 – 20 keV) band following the Ginga results of Koyama et al. (1986a); Koyama (1989) (see section 2.1.2). The SH of the Fe-Kα line is similar to that of the continuum band by Revnivtsev et al. (2006a). They found that the surface brightness distributions along the Galactic plane of the Fe-Kα lines are similar to the infrared surface brightness distribution.

Revnivtsev et al. (2006a); Revnivtsev et al. (2006b) assumed that the infrared distribution represents the Galactic stellar mass distribution (SMD), then proposed that the origin of the GRXE is discrete stellar sources. The ratio of the X-ray luminosity in the 3 – 20 keV band to the near-infrared luminosity is $L_{3-20\,\mathrm{keV}}/L_{3-4\,\mu\mathrm{m}} \sim 4\times10^{-5}$, which corresponds to $\sim 3.5\times10^{27}\,\mathrm{erg\,s^{-1}}\,M_\odot^{-1}$. This luminosity per stellar mass agrees within an uncertainty of ∼50 % to that of the solar neighborhood (Sazonov et al. 2006). Then, they suggested that observations with the sensitivity limit of $\sim 10^{-16}\,\mathrm{erg\,cm^{-2}\,s^{-1}}$ (2 – 10 keV) may resolve ∼90 % of the GRXE into discrete stellar sources.

Revnivtsev & Molkov (2012) performed deep scans with RXTE across the Galactic plane in the energy band of 4.3 – 10.5 keV from $b = 0^\circ$ to -30° at $l = 18.^\circ5$. The SH of the GRXE is estimated to be ∼110 pc. In the point source origin, they argued that the candidate stars with SH∼ 260 pc contribute less than ∼0.3 of the total cumulative fractional emissivity of point sources in the Galactic plane. The cumulative fractional emissivity of the GRXE in the energy band of 2 – 10 keV is $\sim 3\times10^{27}\mathrm{erg\ s^{-1}}M_\odot^{-1}$, consistent with Revnivtsev et al. (2006a) in the energy band of 3 – 20 keV.

One note is that the spatial resolution of both the GDXE and SMD are sub arc-degree. Therefore, the comparison of the GDXE distribution to the SMD did not go into detailed spatial structure of the GDXE, but is limited in the GRXE. The scale heights (SHs) show large variations from author to author, possibly due the large and different beam sizes with each author, or due to the contribution of the GBXE (section 2.2). These prevents to judge the point source populations, e.g. whether high mass stars (SH$\lesssim$ 100 pc) or low mass stars (SH$\gtrsim$100 pc).

2.1.2 K-Shell Lines in the GRXE and Thermal Plasma Origin

The Gas Scintillation Proportional Counter (GSPC) on board the Tenma satellite had higher spectral resolution than the ordinary proportional counter. With the GSPC, Koyama et al. (1986a) discovered an intense emission line of Fe-Kα at ∼6.7 keV. Since the field of view of the GSPC is $3.^\circ1$ (FWHW), the observed sky, which is free from bright XBs are limited to be eight fields in the Galactic inner disk of $280^\circ < l < 340^\circ$ (GRXE). The $\mathrm{EW_{Fe-K}}$ is in the range of ∼500 – 700 eV. They interpreted that the Fe-Kα line is due to an optically thin plasma, because the line center energy of ∼6.7 keV is consistent with Fe XXV-Heα[2]. The plasma temperatures are variable from region to region in the range of ∼5 – 10 keV. They claimed that the temperature variations do not favor the origin of many faint point sources. Even from the limited sample of the eight fields, they determined that the intensity distribution in the 2 – 10 keV band is a disk-shape with the SH of ∼100 – 300 pc and the radius of ∼8 kpc. The total luminosity of the GRXE is estimated to be $\sim 10^{38}\,\mathrm{erg\,s^{-1}}$.

Koyama et al. (1986b) estimated a possible contribution of unidentified SNRs to explain the Fe-Kα line, and argued that if the Supernova (SN) rate is ∼10 / century, the observed GRXE flux and the value of $\mathrm{EW_{Fe-K}}$ would be explained. However, this SN rate is ∼3 – 10 times larger than the canonical value of ∼1 – 3 / century. The allowed region of n_e ($\mathrm{cm^{-3}}$) and t (s), where n_e ($\mathrm{cm^{-3}}$) and t (s) are the electron density and time after the shock heating, respectively, are $\sim 10^{-3} - 4\times10^{-1}$ $\mathrm{cm^{-3}}$ and $\lesssim 3\times10^{12}$ s. Then, the ionization parameter $n_\mathrm{e}t$ is $\lesssim 10^{12}\mathrm{cm^{-3}\,s}$. Therefore, the candidate sources for the origin of the GRXE are young-intermediated aged SNRs in Ionizing Plasma (IP) or in Non-Equilibrium Ionization (NEI). The candidate SNe may occur in a thin ISM so that the surface brightness of the SNRs would be below the resolving capability of the GSPC.

Koyama (1989) re-examined the thermal plasma in the GRXE using more extended GSPC data set of 27 XB-free fields in the Galactic plane, and analyzed the X-ray spectra. The best-fit temperature and $\mathrm{EW_{Fe-K}}$ are ∼3 – 14 keV and ∼0.24 – 1.5 keV, respectively. Thus, the extensive data set of the GSPC provides larger position-dependent variations in the temperatures and $\mathrm{EW_{Fe-K}}$ than those of Koyama et al. (1986a), and hence the argument of the point source origin for the GRXE (section 2.1.1) becomes more unlikely.

The Large Area proportional Counter (LAC) on board the Ginga satellite surveyed the Galactic plane in the Fe-Kα line band with the FWHM beam size of $1.^\circ1\times2.^\circ0$ (Koyama et al. 1989). Since the $\mathrm{EW_{6.7}}$ of XBs, the brightest point sources in the GRXE region, is only $\lesssim$ 50 eV (Hirano 1987), the Fe-Kα line profile is free from possible contamination of bright XBs (figure 1). This is an advantage of the Fe-Kα line over the continuum X-ray band (e.g. 2 – 10 keV band) for the study on the global spatial structure of the GRXE. The total flux of the Fe-Kα line is $\sim 10^{37}\,\mathrm{erg\,s^{-1}}$, about 10 % of the 2 – 10 keV band flux ($\sim 10^{38}\,\mathrm{erg\,s^{-1}}$).

Yamauchi & Koyama (1995) examined the center energy of the Fe-Kα line and $\mathrm{EW_{Fe-K}}$ as a function of the plasma temperature. Since the center energy of the Fe-Kα line and the $\mathrm{EW_{Fe-K}}$ are systematically lower than those expected from a

[2] Soon after, this 6.7 keV line was found to be a complex of the Fe I-Kα, Fe XXV-Heα and Fe XXVI-Lyα lines (section 2.2).

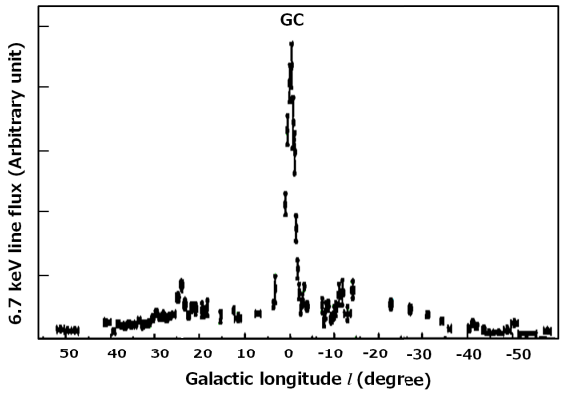

Fig. 1. The longitude distribution of the 6.7 keV line along the Galactic plane taken from the Ginga Galactic plane survey (From Koyama et al. 1989).

collisional ionization equilibrium (CIE) plasma of $\sim$5 – 10 keV temperature in one solar Fe abundance, they estimated the ionization parameter ($n_e t$) to be $10^{10} - 10^{11}$ cm^{-3} s. This is consistent with the scenario of Koyama et al. (1986b) that the GRXE is assembly of young-intermediate aged SNRs, in which the plasma is in IP or NEI. However soon after, the energy down-shift of the Fe-Kα line is found to be a mixture of Fe I-Kα (6.40 keV), Fe XXV-Heα (6.68 keV) and Fe XXVI-Lyα (6.97 keV) lines (see next paragraph), and hence the IP (NEI plasma) interpretation is questionable.

The X-ray CCD detectors on board ASCA had a better energy resolution than any other previous instruments. With ASCA, Yamauchi et al. (1996) and Kaneda et al. (1997) obtained the X-ray spectra from the Scutum Arm region at $l \sim 28^\circ.5$. They resolved the Fe-Kα line into Fe I-Kα (6.40 keV), Fe XXV-Heα (6.68 keV) and Fe XXVI-Lyα (6.97 keV) lines. They also detected the bright Si XVIII-Heα and S XV-Heα lines. Therefore, the GRXE spectra are not single-temperature plasmas, but are well fitted with a two-temperature plasma model, the LTP of $\sim$ 0.8 keV temperature for the Si XVIII-Heα and S XV-Heα lines, and the HTP of $\sim$7 keV temperature for the Fe XXV-Heα and Fe XXVI-Lyα lines.

Kaneda et al. (1997) reported that the surface brightness of the LTP and HTP at $(l, b) \sim (28^\circ.5, 0^\circ)$ are $\sim 2 \times 10^{-6}$ erg cm^{-2} s^{-1} str^{-1} and $\sim 5 \times 10^{-7}$ erg cm^{-2} s^{-1} str^{-1} (0.5 – 10 keV), respectively. The flux of the LTP is extended to $|b| \sim 2^\circ$, larger than the HTP of $|b| \sim 0^\circ.5$. However, taking into account of the differences of the optical depth, they proposed that the real SH of the LTP may be equal to the HTP of $\sim$ 70 pc. Yamauchi et al. (1996) found position-to-position fluctuations of the surface brightness, and concluded that point sources of the luminosity larger than $\sim 2 \times 10^{33}$ erg s^{-1} are not the major origin of the GRXE.

2.1.3 Non-Thermal Emission of the GRXE

In the wide band spectra of the LAC on board Ginga, Yamasaki et al. (1996); Yamasaki et al. (1997) found a hard X-ray tail over the hot plasma components above 10 keV (the non-thermal component) from the Galactic plane in the regions of $l = -20^\circ$ to 40° at $|b| \lesssim 3^\circ$. This non-thermal flux is smoothly extrapolated to the gamma-ray flux in the Galactic plane.

Valinia & Marshall (1998) made an averaged spectrum from the Galactic plane of $|l| \lesssim 30^\circ$ using RXTE. The averaged spectrum in the 3 – 35 keV band is fitted with a model of thermal plasma with $\sim$2 – 3 keV temperature and a power-law component of the photon index (Γ) of $\sim$1.8. Valinia et al. (2000) re-examined the ASCA data at $l \sim 28^\circ.5$, and confirmed the presence of the non-thermal emission. They proposed that the origin of the non-thermal emission is either bremsstrahlung by low energy cosmic-ray (LECR) electrons (LECRe), inverse Compton scattering of ambient microwave, infrared and optical photons by the high energy electrons associated to the LECRe, non-thermal emission from SNRs, or discrete X-ray sources. In the bremsstrahlung origin, the LECRe produce the Fe I-Kα lines at 6.4 keV (section 5.1), hence the Fe-Kα line energy becomes lower than 6.7 keV due to the mixture of the Fe I-Kα line and the Fe XXV-Heα line in a hot plasma. This energy down-shift is consistent with the result of Yamauchi and Koyama (1995).

Valinia & Marshall (1998); Valinia et al. (2000) proposed that the continuum shape is the sum of the non-thermal bremsstrahlung and the thermal plasma; the spectrum is a mixture of a high-temperature plasma (HTP) and bremsstrahlung of LECRe. The best-fit temperature of the HTP by this model is reduced to $\sim$2 – 3 keV from the simple model of $\sim$5 – 10 keV temperature with no bremsstrahlung component. This relaxes the potential difficulty of the production and gravitational confinement of the HTP. Since the HTP temperature is typical to SNRs, they re-visited the idea of Koyama et al. (1986b) that the origin of the HTP in the Galactic disk would be multiple SNe. The surface brightness of these SNRs would be too faint to be resolved into individual SNR (Koyama et al. 1986b). The SN rate is estimated to be $\lesssim$5 / century, which is not unreasonably large. This scenario, however has a serious problem that the $\sim$2 – 3 keV temperature of the HTP is too low to produce strong Fe XXVI-Lyα line, detected with ASCA (section 2.1.2).

2.2 The Galactic Center X-Ray Emission (GCXE)

The X-ray observations of the Galactic Center region were started from the Uhuru satellite (Kellogg et al. 1971). The early results in 1970's were summarized by Proctor et al. (1978). After 1980's, the Galactic center observations have been made by many instruments: Einstein (Watson et al. 1981), Spacelab-2 (Skinner et al. 1987), Spartan-1 (Kawai et al. 1988) and ROSAT (Predehl & Truemper 1994). These instruments (authors) found

a hint of diffuse extended emission near at the GC, in addition to many point sources.

As is shown in figure 1, Ginga found a bright peak at the Galactic center (GC) in the Fe-Kα line distribution along the Galactic plane (Koyama et al. 1989). Yamauchi et al. (1990) made the Fe-Kα line map near at the GC, and found the emission region is an ellipse of $\sim 1.^\circ 8 \times 1.^\circ 0$ size around Sgr A*. The $\mathrm{EW_{Fe-K}}$ is variable in the range of $\sim$500 – 1300 eV, which would be due to the position variable $\mathrm{EW_{6.4}}$, found later with ASCA. This is the first concrete result of the presence of diffuse Galactic center emission, and is referred as the Galactic Center X-ray Emission (GCXE). The surface brightness of the Fe-Kα line in the GCXE is about 10 times larger than that of the GRXE (Koyama et al. 1989). The total X-ray luminosity is estimated to be $(0.8-2.3)\times10^{37}$ erg s^{-1}.

The X-ray CCD detectors on board ASCA resolved the Fe-Kα line in the GCXE into Fe I-Kα (6.40 keV), Fe XXV-Heα (6.68 keV) and Fe XXVI-Lyα (6.97 keV) lines, and found Si XVIII-Heα, Si XVIV-Lyα, S XV-Heα, S XVI-Lyα, Ar XVII-Heα, Ar XVIII-Lyα and Ca XIX-Heα lines (Koyama et al. 1996). The spectra of the GCXE are fitted with a thermal bremsstrahlung of $\gtrsim 10$ keV temperature plus many Gaussian lines. These are similar from position to position except the regions of the Sgr A and Sgr B MC complexes. The plasma temperature of $\gtrsim 10$ keV is unusually high even for young SNRs. The total luminosity of the GCXE is estimated to be $\sim 10^{37}$ erg s^{-1}. Together with the uniformity over the GCXE, Koyama et al. (1996) suggested that the GCXE is due to a large scale diffuse plasma with very high temperature. In this case, however, the plasma is very difficult to be confined by the Galactic gravity.

Tanaka et al. (2000); Tanaka (2002) also examined the ASCA spectrum of the GCXE and those in the Scutum and Sagittarius ($l \sim 10^\circ$) regions (GRXE). They claimed that the Fe XXV-Heα and Fe XXVI-Lyα lines are significantly broadened to $\sim$80 eV (1σ), corresponding to a velocity dispersion of a few thousand km s^{-1}, higher than the thermal velocity of the $\sim$10 keV temperature plasma. They argued that the boarding is due to charge exchange (CX) of low-energy cosmic-ray irons. The low-energy cosmic-ray origin is consistent with the presence of a non-thermal component in the GRXE (section 2.1.3). They also obtained the $\mathrm{EW_{6.4}}$, $\mathrm{EW_{6.7}}$ and $\mathrm{EW_{6.97}}$ to be $\sim$110, $\sim$270 and $\sim$150 eV, respectively. However, these small $\mathrm{EW_{6.4}}$, $\mathrm{EW_{6.7}}$ and $\mathrm{EW_{6.97}}$ and the broadenings of the Fe XXV-Heα and Fe XXVI-Lyα lines are later rejected with Suzaku by Koyama et al. (2007c) (section 3.3).

The Fe I-Kα line is very clumpy with a strong peak at the giant molecular cloud (MC) Sgr B2. GRANAT found an elongated hard X-ray emission (8.5 – 19 keV) parallel to the Galactic plane in correlation to the map of MCs (Sunyaev et al. 1993). They suggested that the high energy X-rays come from nearby compact sources (XBs), which are Thomson scattering by a dense molecular gas. The scattered X-ray flux is expected to be more than 10 % of the observed hard X-ray flux from the GCXE. They proposed that the remaining flux is due to the past X-ray flare of Sgr A*.

The ASCA discovery of the Fe I-Kα clump from the Sgr B2 cloud (Koyama et al. 1996) strongly supports the idea of the past X-ray flare of Sgr A*. Murakami et al. (2000) examined the Sgr B2 cloud, and found a very peculiar spectrum, a strong emission line at $\sim$6.4 keV, a low-energy cutoff below $\sim$4 keV and a pronounced edge structure at $\sim$7.1 keV. The X-ray spectrum and the morphology are well reproduced by a scenario that X-rays from an external source located in the Galactic center direction are scattered by the molecular cloud Sgr B2 and come into our line of sight. They named the Fe I-Kα source at Sgr B2 as the X-ray Reflection Nebula (XRN). The 4 – 10 keV band luminosity of this XRN is $\sim 10^{35}$ erg s^{-1}. Soon after, other XRN candidates, Fe I-Kα clumps are found from the Sgr A and Sgr C MC complexes (section 5.1), and from the other selected regions (section 5.2).

2.3 The Galactic Bulge X-Ray Emission (GBXE)

In the early studies, Cooke et al. (1969); Protheroe et al. (1980); Warwick et al. (1980); Iwan et al. (1982) found an X-ray emission extended to a high Galactic latitude of SH $\gtrsim$ 500 pc – 1.5 kpc. The emission is also extended to a large Galactic longitude.

A secure detection of an extended emission near the GCXE with larger SH than those of the GRXE and GCXE was made with Ginga using the Fe-Kα line distribution. Yamauchi & Koyama (1993) found largely extended Fe-Kα lines by $\sim 5^\circ$ ($\sim$ 700 pc) above and below the Galactic plane, in addition to a narrow component of the SH$\sim$ 100 pc (GRXE). The longitude extension is estimated to be $\sim$1.4 kpc from Sgr A*. This diffuse X-ray emission is named the Galactic Bulge X-ray Emission (GBXE), because of the association to the Galactic bulge region. This is the third component of the GDXE recognized after the GRXE and GCXE.

Using RXTE, Valinia & Marshall (1998) examined the flux distribution in the central $l = \pm 30^\circ$ of the Galactic plane in more detail, and found two components, a thin and broad disks with the e-folding scales of $\lesssim 0.^\circ 5$ and $\sim 4^\circ$, or the SHs of $\lesssim$70 pc and $\sim$500 pc, respectively. The longitude extension of the later component (SH$\sim$500 pc) is, however, not constrained.

Revnivtsev (2003) observed the area of $|l| \lesssim 10^\circ$ and $|b| \lesssim 10^\circ$ around Sgr A* in the 3 – 10 keV band. They found that the intensity distribution in the $|b| > 2^\circ$ region is well described by an exponential model with the e-folding latitude of $\sim 3^\circ$. The e-folding longitude scale is not determined. The best-fit spectral parameters of the larger SH component (GBXE) are not

significantly different from those of the smaller SH component (GRXE).

Revnivtsev et al. (2006a) examined the longitude and latitude profiles at $3.^\circ0 < |b| < 3.^\circ5$, and $1^\circ < |l| < 4^\circ$. The e-folding latitude is $\sim 2^\circ - 3^\circ$, while the e-folding longitude is $\sim 8^\circ$. Thus, they confirmed the two components proposed by Yamauchi & Koyama (1993), the bulge/bar (GBXE) and the disk of the Galaxy (GRXE). The GBXE is more largely extended than the GRXE above and below the plane with the total luminosity of $\sim 4 \times 10^{37}\,\mathrm{erg\,s^{-1}}$. Revnivtsev et al. (2006b) further examined the two-dimensional distribution in the Fe-Kα line, from the central $15^\circ \times 15^\circ$ region around Sgr A*(section 2.1.4). They found that the linear correlations between near-infrared and the surface brightness of the Fe-Kα line are similar between the disk and bulge. Therefore, they proposed that the populations of the unresolved X-ray point sources in the disk (GRXE) and the bulge (GBXE) are not different with each other. Revnivtsev & Molkov (2012) also found two components of SH$\sim$110 pc and $\sim$260 pc. in the Galactic latitude of $-5^\circ < b < 0^\circ$ at $l = 18.^\circ5$.

In summary, Ginga and RXTE discovered the new component GBXE, which has a larger SH than that of the GRXE. With RXTE, Revnivtsev (2003); Revnivtsev et al. (2006a); Revnivtsev et al. (2006b) suggested no difference in the spectra and point source compositions between GRXE and GBXE. However, the limited spectral resolutions prevented reliable study whether or not the spectrum of the GBXE is different from that of GRXE. Also, the limited spatial resolution prevented to obtain reliable SH of the GBXE (section 2.1.1). These issues are solved later with Suzaku (section 3).

3 Global Structure of the GDXE

This section overviews the GDXE, the recent results of Chandra, XMM-Newton, Suzaku and partly NuSTAR. From the spatial distributions of the Fe-Kα, S XV-Heα and S XVI-Lyα lines, the GDXE is clearly decomposed into three separate components, GCXE, GBXE and GRXE (section 3.1). The X-ray luminosity and spectra of these components are given in section 3.2. The spectral difference among GCXE, GBXE and GRXE verify the decomposition of the GDXE. The detailed structure of the central region of the GCXE is discussed in section 3.3.

3.1 Decomposition of the GDXE into the GCXE, GBXE and GRXE

As are given in sections 2.1, 2.2 and 2.3, the GCXE and GBXE are separated from the GDXE. However a clear separation in both the spatial and spectral profiles has to wait the Suzaku satellite. Uchiyama et al. (2013) made Suzaku surveys around the Galactic center regions of $|b| \leq 0.^\circ5$, $|l| \leq 1^\circ$, and additional regions of larger $|b|$ and $|l|$ in the Galactic plane. Since the position of the Galactic center, Sgr A* is at $(l, b) = (-0.^\circ056, -0.^\circ046)$, new parameters of the Galactic coordinates (l_*, b_*) are defined hear and after, shifting l and b by $-0.^\circ056$ and $-0.^\circ046$, respectively.

They divided the surveyed regions into many rectangles of $\Delta l_* = 0.^\circ1$, $\Delta b_* = 0.^\circ2$, and analyzed the X-ray spectra from each rectangle. These spectra are fitted with a power-law continuum plus many Gaussians lines to represent the Kα, Heα and Lyα lines of S, Ar, Ca and Fe. The best-fit Fe-Kα (Fe I-Kα, Fe XXV-Heα and Fe XXVI-Lyα) fluxes in the positive l_* region near Sgr A* are larger than those in the negative l_* region (Uchiyama et al. 2013). This asymmetry is mainly due to the bright SNR Sgr A East, the Arches cluster and XRNe (see sections 4.1 and 5). Therefore, the line and continuum band distributions of the GDXE are made excluding these bright local spots. The profiles are shown by the black circles in figure 2.

Figure 2 shows the Galactic longitude distributions of the Fe-Kα, S XV-Heα and S XVI-Lyα line fluxes have two-exponential components, the small size ($|l_*| \leq 1^\circ - 2^\circ$), and largely extended ($|l_*| \geq 2^\circ - 3^\circ$) emissions. Therefore, Uchiyama et al. (2013) fitted the flux distributions by a phenomenological formula,

$$A_1 \exp(-|l_*|/l_1)\exp(-|b_*|/b_1) + A_2 \exp(-|l_*|/l_2)\exp(-|b_*|/b_2) \quad (1)$$

, where the unit of the flux is photons $\mathrm{s^{-1}\,cm^{-2}\,arcmin^{-2}}$. The best-fit curves of the Fe-Kα, S XV-Heα and S XVI-Lyα lines are given by the dotted lines in figure 2, while the best-fit parameters of these lines and those of the 2.3 – 5 keV and 5 – 8 keV band fluxes are listed in table 2. The best-fit e-folding longitude (l_1 and l_2) clearly indicate that the GDXE has two components: the small size ($|l_*| \lesssim 1^\circ$), and larger size ($|l_*| \geq 1^\circ$) emissions. The former and latter are the GCXE and GRXE, respectively.

Table 2. Fitting results of two-dimension & exponential function (after Uchiyama et al. 2013)*.

Component	A_1 (10^{-7}photon $\mathrm{s^{-1}\,cm^{-2}\,arcmin^{-2}}$)	A_2	l_1 (degree)	l_2
	Sulfur(S)			
Heα	7.8 ± 0.5	0.75 ± 0.08	0.58 ± 0.05	52 ± 13
Lyα	0.31 ± 0.24	0.32 ± 0.05	0.58†	52†
	Iron (Fe)			
Kα	6.2 ± 0.6	0.21 ± 0.09	0.62 ± 0.09	57 ± 50
Heα	14.6 ± 0.5	0.91 ± 0.08	0.63 ± 0.03	45 ± 10
Lyα	6.1 ± 0.3	0.18 ± 0.04	0.63‡	45‡
	Continuum Band			
2.3–5 keV	126 ± 15	16 ± 1	0.63 ± 0.07	59 ± 6
5–8 keV	101 ± 11	6.2 ± 0.6	0.72 ± 0.06	52 ± 9

$*$ Errors are 1 σ confidence levels.

† Fixed to S XV-Heα.

‡ Fixed to Fe XXV-Heα.

As is noted in section 2.3, another component, the GBXE, has been found near the GCXE. The SH of the GBXE is larger

than those of the GCXE and GRXE. Therefore, the e-folding latitudes of the GCXE and GRXE (b_1 and b_2) in equation (1) would be contaminated by that of the GBXE, while the e-folding longitudes (l_1 and l_2) are not significantly affected by the GBXE. Therefore, only the parameters of l_1 and l_2 are listed in table 2, but b_1 and b_2 are excluded from the original table given by Uchiyama et al. (2013).

The coexistence of the Fe XXV-Heα, Fe XXVI-Lyα, S XV-Heα, S XVI-Lyα and Fe I-Kα lines clearly indicates that the GDXE is composed of three components, the HTP (for the Fe XXV-Heα and Fe XXVI-Lyα lines), LTP (for the S XV-Heα and S XVI-Lyα lines) and CG (for the Fe I-Kα line). The profiles of figure 2 (upper panel) shows that the flux ratio of Fe XXVI-Lyα / Fe XXV-Heα in the GCXE ($|l_*| \lesssim 1^\circ$) is larger than that of the GRXE ($|l_*| \gtrsim 1^\circ$). An opposite trend is found in the flux ratio of S XVI-Lyα / S XV-Heα (figure 2, lower panel). The intensity profiles of the GCXE and GRXE regions in the other key elements, Ar and Ca are approximately in between those of S and Fe.

The temperatures of the LTP and HTP are estimated by the intensity ratios of S XVI-Lyα / S XV-Heα, and Fe XXVI-Lyα / Fe XXV-Heα, respectively. Then, the temperature of the LTP in the GCXE is lower than the GRXE, while that of the HTP in the GCXE is higher than the GRXE (see section 3.2). Thus, the flux distributions of the Fe XXV-Heα, Fe XXVI-Lyα, S XV-Heα and S XVI-Lyα lines in the GCXE and GRXE given in figure 2 (upper and lower panels) clearly demonstrate that the global spectra of the GCXE and GRXE are different with each other.

Yamauchi et al. (2016) separately estimated the e-folding latitudes (b_1 and b_2) using all the Suzaku archive data along and near the Galactic inner disk ($|b_*| \leq 3^\circ$, $|l_*| \leq 30^\circ$). To increase statistics, the data are grouped according to the positions of (a): $|l_*| \leq 0.^\circ5$, (b): $l_* = 358.^\circ5$, (c): $l_* = 330^\circ - 350^\circ$, and (d): $l_* = 10^\circ - 30^\circ$. The position (a) includes mainly the GCXE and some fractions of the GBXE, while the main component in the position (b) is the GBXE with small fractions of the GCXE. The data in the positions (c) and (d) are from the GRXE.

The intensity profile perpendicular to the Galactic plane in the 5 – 8 keV band and Fe-Kα line fluxes are made for the regions of (a) – (d). The profiles near potitoin (a) and (b) show two component shape. As examples, the Fe-Kα lines profiles at the region of (a) are shown in figure 3. In order to make clear the two-component structure, the profiles in the regions (a) and (b) are simultaneously fitted by a 2-exponatial model of,

$$A_1 \exp(-|b_*|/b_1) + A_2 \exp(-|b_*|/b_2) \quad (2)$$

, where the subscripts 1 and 2 represented the GCXE and GBXE, respectively. The free parameters of respective normalizations (A_1 and A_2) and the e-folding latitudes (b_1 and b_2) for the GCXE and GBXE, are linked in the (a) and (b) regions. The best-fit profiles of the Fe-Kα lines at the position (a) are shown by the two solid lines in figure 3.

Table 3. Parameters of e-folding latitude of the GCXE, GBXE and GRXE (after Yamauchi et al. 2016)*

Region	Component	Norm(A) (†)	e-fold (b_1, b_2)‡ (degree)
GCXE	Fe I-Kα	4.1±0.2	0.22±0.02
	Fe XXV-Heα	11.9±0.6	0.26±0.02
	Fe XXVI-Lyα	4.9±0.2	0.24±0.02
	5–8 keV	77±4	0.25±0.02
GBXE	Fe I-Kα	0.31±0.15	1.15±0.36
	Fe XXV-Heα	1.14±0.34	2.25±0.68
	Fe XXVI-Lyα	0.40±0.12	2.13±0.66
	5–8 keV	12±2	1.96±0.25
GRXE⋆	Fe I-Kα	0.26±0.03	0.50±0.12
	Fe XXV-Heα	0.65±0.02	1.02±0.12
	Fe XXVI-Lyα	0.09±0.02	0.71±0.29
	5–8 keV	5.4±0.4	1.04±0.20

∗ Errors are 1 σ confidence levels.

† In unit of 10^{-7}photons s^{-1}cm^{-2} arcmin^{-2}.

‡ The parameter b_1 is the e-folding latitude of the GCXE, while b_2 is that of the GBXE or GRXE.

⋆ Average of the $l_* = 10^\circ - 30^\circ$ and$l_* = 330^\circ - 350^\circ$

Table 4. The properties of the GCXE, GBXE and GRXE

Component	Norm(A) (†)	e-folding ‡ (l°)	(b°)	Luminosity (erg s^{-1})
GCXE				
Fe I-Kα	4.1	0.62	0.22	1.5×10^{34}
Fe XXV-Heα	12	0.63	0.26	5.8×10^{34}
5–8 keV	77	0.72	0.25	3.9×10^{35}
GBXE				
Fe I-Kα	0.31	-	1.15	-
Fe XXV-Heα	1.1	10	2.25	7.5×10^{35}
5–8 keV	12	8	1.96	5.3×10^{36}
GRXE				
Fe I-Kα	0.36	57	0.50	2.9×10^{35}
Fe XXV-Heα	1.0	45	1.02	1.4×10^{36}
5–8 keV	7.9	52	1.04	1.2×10^{37}

† The normalization (A) of the GCXE and GBXE are taken from Yamauchi et al. (2016) (table 3), while those of the GRXE are converted to the GC position using the e-fold (l) of Uchiyama et al. (2013) (table 2), in unit of 10^{-7}photons s^{-1}cm^{-2} arcmin^{-2}.

‡ The e-folding scales (b) are taken from Yamauchi et al. (2016) (table 3), while the e-folding longitude (l) for the GCXE and GRXE are taken from Uchiyama et al. (2013) (table 2), and those for the GBXE are from Yamauchi and Koyama (1993), and Revnivtsev et al. (2006a).

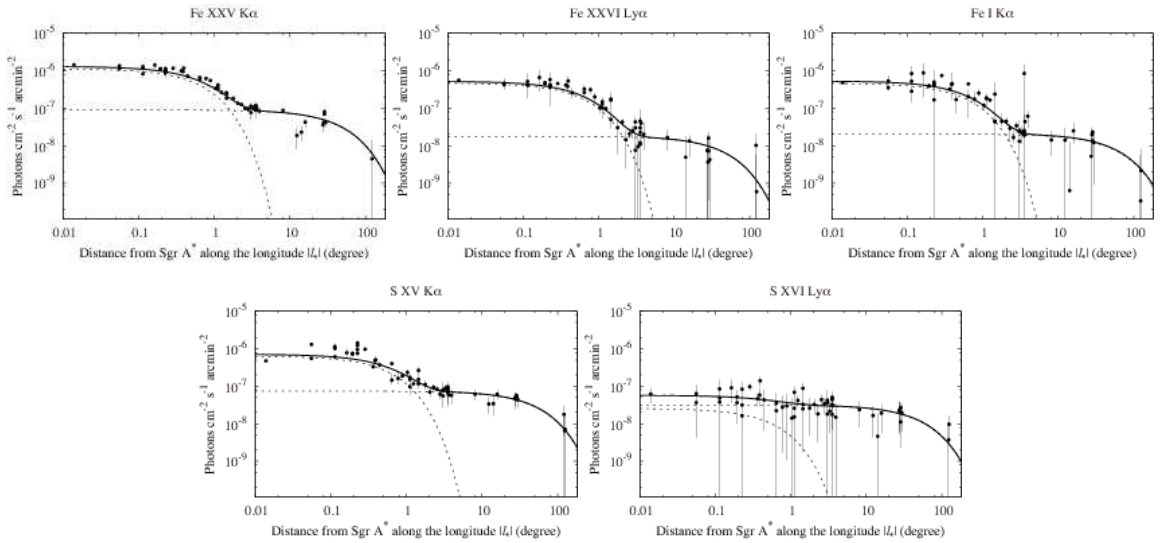

Fig. 2. Upper panel: the longitude profiles of Fe XXV-Heα (left), Fe XXVI-Lyα (center), and Fe I-Kα (right).Lower panel: the longitude profiles of S XV-Heα (left) and S XVI-Lyα (right). (From Uchiyama et al. 2013)

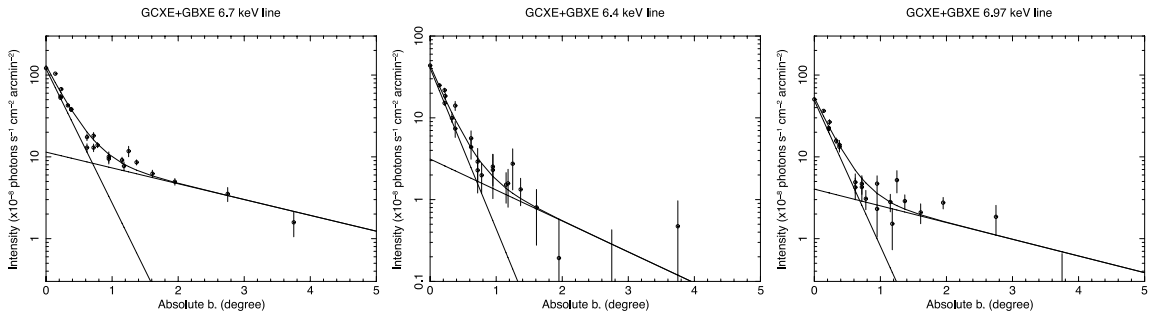

Fig. 3. The latitude distributions of Fe XXV-Heα (left), Fe XXVI-Lyα (center), and Fe I-Kα (right).(From Yamauchi et al. 2016)

On the other hand, the profiles of the (c) and (d) regions show one-exponential shape , and hence fitted with 1-exponatial model of,

$$A\exp(-|b_*|/b_2) \tag{3}$$

, where the e-folding latitudes (b_2) in the (c) and (d) regions are linked. The best-fit e-folding latitude of b_1 and b_2 for the Fe-Kα and the 5 – 8 keV band fluxes in the GCXE, GBXE and GRXE are listed in table 3.

The regions and luminosity of the Fe XXV-Heα and Fe I-Kα lines, and the 5-8 keV band in the GCXE, GBXE and GRXE are determined from the e-folding scales of the Fe XXV-Heα and Fe I-Kα lines, where the longitude and latitude scales are taken from tables 2 and 3, respectively. The longitude scale for the GBXE is unclear, and hence taken from the old data of Yamauchi and Koyama (1993), and Revnivtsev et al. (2006a). The normalization (A) at b_*=0 are taken from table 3, where those of the GRXE are calculated from the e-folding longitude (l_2) in table 2. Thus determined regions and luminosity of the Fe XXV-Heα and Fe I-Kα lines, and those of the 5 – 8 keV band, in the GCXE, GBXE and GRXE are summarized in table 4. Hear and after, the regions of the GCXE, GBXE, and GRXE are followed from table 4. The study of the GCXE, GBXE and GRXE spectra are given in the next section (section 3.2).

3.2 X-Ray Spectra and Luminosity of the GCXE, GBXE and GRXE

The Suzaku spectra in the selected regions of the GCXE and GRXE have been made by several authors (Koyama et al. 2007c; Ebisawa et al. 2008; Yuasa et al. 2008; Yamauchi et al. 2009; Heard & Warwick 2013a). Uchiyama et al. (2013) made the whole spectra of the GCXE and GRXE. However the regions of the GRXE are limited, and would be contaminated by the GBXE. The GCXE , on the other hand, is fur bright, and hence contamination from the GBXE is ignored. The spectrum of the GCXE is fitted with 2-CIE and one power-law model, which are associated with the highly ionized atomic lines and the Fe I-Kα line, respectively. The best fit temperatures are $\sim$0.95 keV and $\sim$7.5 keV with the iron abundance of $\sim$1.25 solar, while the best-fit photon index and EW$_{6.4}$ are $\sim$2.1 and $\sim$0.46 keV, respectively.

Table 5. The best-fit parameters of the GCXE, GBXE and GRXE spectra (after Nobukawa et al. 2016).∗

		GCXE		GBXE		GRXE	
Continuum							
$N_{\rm H}$ (10^{22} cm^{-2})		6 (fix)		3 (fix)		3 (fix)	
Fe K edge†		0.24 ± 0.01		0 (fix)		0 (fix)	
$kT_{\rm e}$ (keV)		$14.9^{+0.5}_{-0.6}$		5.1±0.4		5.0±0.4	
Emission lines							
Line‡	CE§	Flux⋆	EW§	Flux⋆	EW§	Flux⋆	EW§
Fe I-Kα	6400	3.54±0.04	175±2	0.14±0.02	84±10	0.16±0.01	118±9
Fe XXV-Heα	6680	9.40±0.05	500±3	0.70±0.02	463±13	0.60±0.02	487±13
Fe XXVI-Lyα	6966	3.45±0.04	198±2	0.24±0.02	173±13	0.10±0.01	96±11
Fe I-Kβ	7059	0.44#	26	0.01#	14	0.02#	19
χ^2/d.o.f.		331/265		117/84		107/72	

∗ Errors are 1 σ confidence levels.

† Absorption depth at 7.11 keV.

‡ ATOMDB 3.0.2 (http://www.atomdb.org/) and Wargelin et al. (2005).

§ Units of CE (line Center Energy) and EW are electron bolt (eV), respctively

⋆ Flux is in unit of 10^{-7} photon cm^{-2} s^{-1} arcmin^{-2}.

Fixed to 0.125×Fe I-Kα.

Nobukawa et al. (2016) made the global spectra of the GCXE, GRXE and GBXE in the 5 – 10 keV band from the regions of ($|l_*| < 0.^\circ 6, |b_*| < 0.^\circ 25$), ($|l_*| < 0.^\circ 6, 1.^\circ 0 < |b_*| < 3.^\circ 0$), and ($|l_*| = 10^\circ - 30^\circ$, $|b_*| < 1.^\circ 0$), respectively (following table 4). For the GBXE spectrum, the overlapping region to the GCXE ($|b_*| < 1.^\circ 0$) is excluded, to avoid a large contamination from the GCXE spectrum. For the GCXE spectrum, the bright spots of the Fe I-Kα and Fe XXV-Heα lines are excluded (see sections 4 and 5). They fitted the GCXE, GBXE and GRXE spectra with a model of a bremsstrahlung plus Gaussian lines at 6.40 keV, 6.68 keV and 6.97 keV (Fe I-Kα, Fe XXV-Heα and Fe XXVI-Lyα, respectively), including the other faint lines. The best-fit results are listed in table 5.

The flux ratio of Fe XXVI-Lyα / Fe XXV-Heα of the GCXE, GBXE and GRXE are ∼0.37, ∼0.34 and ∼0.17, which correspond to the CIE temperatures of ~ 6.8 keV, ~ 6.5 keV and ~ 5.0 keV, respectively. Thus the plasma temperatures of the GCXE, GBXE and GRXE determined by the line flux ratio of Fe XXVI-Lyα / Fe XXV-Heα are not largely difference with each other. However the continuum shape (bremsstrahlung) of the GCXE gives the temperature of ∼15 keV, which is significantly larger than those of the GBXE and GRXE of ∼5 keV (table 5). The reason of this apparent inconsistency in the temperatures is found in the different flux ratio of Fe I-Kα / Fe XXV-Heα. The flux ratio Fe I-Kα / Fe XXV-Heα in the GCXE is ∼0.38, which is significantly larger than those of the GBXE and GRXE of ∼0.20 and ∼0.27, respectively. This indicates that the hard X-rays of power-raw spectrum of the CG occupy larger fraction in the GCXE, and hence gives apparently higher bremsstrahlung temperature than those of the GBXE and GRXE.

Using the parameters of the GCXE, GBXE and GRXE regions in table 4 and table 5, the total X-ray fluxes of the GCXE, GBXE and GRXE in the 5 – 8 keV band are estimated, which are also given in table 4. The 5 – 8 keV band luminosity of $\sim 3.9 \times 10^{35}$ erg s^{-1}, $\sim 5.3 \times 10^{36}$ erg s^{-1} and $\sim 1.2 \times 10^{37}$ erg s^{-1} are converted to the 2 – 10 keV band luminosity of $\sim 1.2 \times 10^{36}$ erg s^{-1}, $\sim 1.6 \times 10^{37}$ erg s^{-1} and $\sim 3.8 \times 10^{37}$ erg s^{-1}, for the GCXE, GBXE and GRXE, respectively. These are smaller than the previous reports, due to the smaller e-folding longitude and latitude scales of the GCXE, GBXE and GRXE. However, the quality of the spectra of table 5 is the best, in particular, mutual mixing of the GCXE, GBXE and GRXE spectra are minimized.

3.3 Iron K-shell Line Property of the Central Region of the GCXE

Koyama et al. (2007c) studied the hard X-ray spectrum in the 5 – 10 keV band of the central GCXE region of $|l_*| < 0.^\circ 3, |b_*| < 0.^\circ 15$. They made the X-ray spectrum excluding the Sgr A East SNR (section 4.1.1), but including the bright XRNe at the north-east of Sgr A* (section 5.2.2). This spectrum is fitted by the same model of section 3.2, a phenomenological model of a bremsstrahlung continuum plus many Gaussian lines. The best-fit spectral parameters are given in table 6.

The Fe XXV-Heα line is a blend of the resonance, inter-combination and forbidden lines. The mixing ratios of these lines depend on the plasma nature such as charge exchange

(CX). Depending on the plasma temperature, satellite lines from iron of less ionized than He-like iron, such as the dielectronic recombination lines may be contained (Beiersdorfer et al. 1992; Beiersdorfer et al. 1993). All these processes shift the nominal Fe XXV-Heα energy of 6.68 keV to a lower energy; the line center of the Fe XXV-Heα produced by the CX process is 6666 ± 5 eV (Wargelin et al. 2005). The observed center energy and width of the Fe XXV-Heα line are 6680$\pm$1 eV and $\sim$40 eV, respectively, consistent with the proper mixing ratio of the resonance, inter-combination and forbidden lines in the normal CIE plasma of $\sim$6 – 7 keV temperature.

The flux ratio of Fe XXVI-Lyα / Hea is $\sim$0.33, which corresponds to the ionization temperature of $\sim$6 – 7 keV. The flux ratio of Fe XXV-Heβ / Fe XXV-Heα is $\sim$0.1, which gives the electron temperature of $\sim$6 – 7 keV. Thus, the center energy and width of the Fe XXV-Heα line, and the flux ratios of Fe XXVI-Lyα and Fe XXV-Heβ lines relative to the Fe XXV-Heα line (Fe XXVI-Lyα / Fe XXV-Heα and Fe XXV-Heβ / Fe XXV-Heα) favor a CIE plasma of $\sim$6 – 7 keV temperature for the HTP.

Then, Koyama et al. (2007c) fitted the GCXE spectrum with a model of CIE plasma. The best-fit temperature and iron abundance are consistent with those of Uchiyama et al. (2013) and Nobukawa et al. (2016) in the whole GCXE area of $|l_*| < 0.^\circ6, |b_*| < 0.^\circ25$ (see sections 3.1 and 3.2). This indicates that the HTP spectrum in the central GCXE region of $|l_*| < 0.^\circ3, |b_*| < 0.^\circ15$ is nearly the same as the whole GCXE; no significant variation of the HTP is found over the whole GCXE region.

Koyama et al. (2009) made correlation plot of the $EW_{6.7}$ and $EW_{6.4}$ taken from small areas of $4.'5 \times 4.'5$. The correlation plots are shown in figure 4. The solid line shows the correlation function, which is $EW_{6.4} + 2 \times EW_{6.7} \simeq 1.2$ keV. The scattered correlation plots indicate that the mixing ratio of the HTP (Fe XXV-Heα) and CG (Fe I-Kα) are different from position to position. In the extreme case, where the $EW_{6.7}$ is 0 keV (HTP = 0), the $EW_{6.4}$ is $\sim$ 1.2 keV, or the CG has the $EW_{6.4}$ of $\sim$ 1.2 keV. This large $EW_{6.4}$ favors that the origin of the Fe I-Kα line is due to the irradiation of external X-ray sources or low energy cosmic ray proton (LECRp) on MCs (see section 5). The $EW_{6.7}$ is $\sim$0.6 keV at $EW_{6.4}$ = 0 keV (CG = 0). This value is consistent with Koyama et al. (2007c) that the HTP has a CIE spectrum with temperature and abundances of $\sim$6 – 7 keV and nearly one solar, respectively.

Figure 4 shows that the scatter of the $EW_{6.4}$ is larger than that of the $EW_{6.7}$, which means that the Fe I-Kα flux (CG) is more clumpy than the Fe XXV-Heα flux (HTP). The $EW_{6.4}$ and $EW_{6.7}$ of the west region of Sgr A* (GC west), where free from the bright Fe I-Kα and Fe XXV-Heα spots, are given by the filled circles in figure 4. The $EW_{6.4}$ and $EW_{6.7}$ are concentrated in the small parameter space of $EW_{6.7}$ $\sim$510 eV and $EW_{6.4}$ $\sim$ 180 eV, which are consistent with those of the whole GCXE (table 5), but are significantly larger than the ASCA results of (Tanaka 2002). Since Suzaku had a larger correcting area and better spectral resolution, the results of Suzaku would be more reliable than ASCA.

Table 6. The best-fit parameters of the GCXE spectrum (after Koyama et al. 2007c)*.

Continuum			
$N_{\rm H}$ (cm^{-2})	6×10^{22}		
$N_{\rm Fe}$ (cm^{-2})	$9.7^{+0.7}_{-0.4} \times 10^{18}$		
$kT_{\rm e}$ (keV)	15^{+2}_{-1}		
Emission lines			
Identification	Center Energy (eV)	Width (eV)	Intensity (‡)
Fe I† Kα	6409$\pm$1	33^{+2}_{-4}	$43.2^{+0.5}_{-0.8}$
Fe XXV Heα	6680$\pm$1	39$\pm$2	$51.0^{+0.8}_{-0.6}$
Fe XXVI Lyα	6969^{+6}_{-3}	15^{+8}_{-15}	$16.6^{+0.9}_{-1.1}$
Fe I† Kβ	7069*	38§	$6.91^{+1.12}_{-0.96}$
Ni I† Kα	7490^{+12}_{-14}	0 ($<$28)	$3.05^{+0.73}_{-0.57}$
Ni XXVII Heα	7781^{+24}_{-31}	39$^\vert$	$3.97^{+1.06}_{-0.65}$
Fe XXV Heβ	7891$^\#$	30 (fixed)	$4.69^{+0.81}_{-0.61}$
Fe XXVI Lyβ	8220^{+31}_{-22}	30 (fixed)	$2.29^{+1.35}_{-1.31}$
Fe XXV Heγ	8264**	30 (fixed)	$3.08^{+1.32}_{-1.34}$
Fe XXVI Lyγ	8681^{+33}_{-32}	0 ($<$91)	$1.77^{+0.62}_{-0.56}$

$*$ Errors are 1σ confidence levels.

† Neutral or low ionization state.

‡ In unit of 10^{-5} photons s^{-1} cm^{-2}.

$\star$ Fixed to 1.103 $\times E$ (Fe I Kα).

§ Fixed to 1.103 $\times$ σ (Fe I Kα).

| Fixed to σ (Fe XXV Heα).

$\#$ Fixed to $110 + E$ (Ni XXVII Heα).

$**$ Fixed to $44 + E$ (Fe XXVI Lyβ).

The large and scattered $EW_{6.4}$ of the GC east (open circles in figure 4) are due to the XRNe (open squares) and / or the Fe I-Kα line contamination of the surrounding XRNe. The XRNe are associated with non-thermal power-law emissions (section 5.2.2). Yuasa et al. (2008) discovered a power-law emission from the GCXE with the photon index of $\sim$2. Most of them would be due to the XRNe, because Mori et al. (2015) found hard X-ray excesses in the 10 – 20 keV band with NuSATR, at the positions of the XRNe in the Sgr A complex, MC1, MC2, Bridge, and G0.11$-$0.11 and another Fe I-Kα source, the Arches cluster (see tables 9 and 11). The photon index of MC1 and Bridge are $\sim$2.2 and $\sim$1.8, respectively, similar to the power-law emission of Yuasa et al. (2008).

In the close vicinity of Sgr A*, the region of $4' - 13'$ from Sgr A*, using XMM-Newton, Heard & Warwick (2013a) found that the $EW_{6.4}$, $EW_{6.7}$, and $EW_{6.97}$ are $\sim$220 eV, $\sim$730 eV, and $\sim$320 eV, respectively, which are 1.3 – 1.5 times larger than

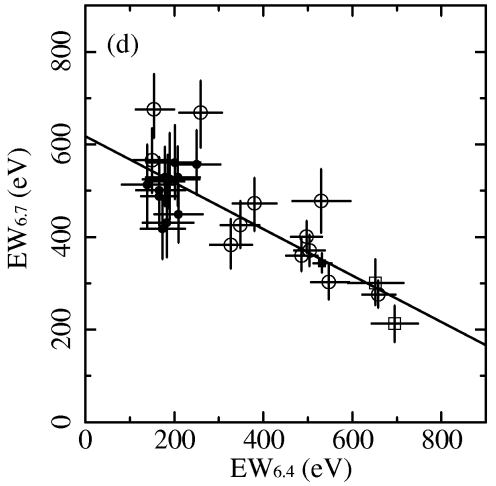

Fig. 4. The scarred plots of $EW_{6.7}$ and $EW_{6.4}$. The solid line shows the best-fit relation of $EW_{6.4}$ +2×$EW_{6.7}$≃1.2 keV. The open and filled circles are data from the Galactic east and west fields, respectively. The data from bright Fe I-Kα regions near the Radio arc are plotted by the open squares (From Koyama et al. 2009).

those of the whole GCXE region (Nobukawa et al. 2016). The larger EW_{Fe-K} would be due to a lower continuum flux than Nobukawa et al. 2016; Heard & Warwick (2013a) assumed a 7.5 keV- plasma for the continuum flux, while Nobukawa et al. (2016) included a power-law component associated to the Fe I-Kα line, with the best-fit bremsstrahlung temperature of ∼15 keV, significantly higher than 7.5 keV.

Uchiyama et al. (2013) more explicitly fitted the GCXE spectra with a model of 7.3 keV-plasma and power-law of $\Gamma = 1.4$. The $EW_{6.4}$ and $EW_{6.7}$ in the GC west (Koyama et al. 2009) (filled circles in figure 4) are ∼180 eV and ∼510 eV, respectively. These are consistent with Nobukawa et al. (2016).

Muno et al. (2004a) made the Chandra X-ray spectrum in the region of $< 9'$ from Sgr A*. They fitted the spectrum with a 2-CIE model, and found that the best-fit temperatures are ∼0.81 keV and ∼7.7 keV. The best-fit Fe abundance is ∼0.7 solar. However their model did not include power-law component. Adding a power-law component of the same flux of Uchiyama et al. (2013), the Fe abundance is revised to be ∼1.1 solar, in agreement with Uchiyama et al. (2013).

In the $3'.5 - 5'$ ring around Sgr A*, Uchiyama et al. (2017) analyzed the Suzaku spectrum. In order to take into account of overflow flux from the bright SNR Sgr A East, they did simultaneous fit for the GCXE and Sgr A East. The best-fit $EW_{6.4}$, $EW_{6.7}$ and $EW_{6.97}$ in the GCXE are ∼160 eV, ∼520 eV and ∼190 eV, respectively, in good agreement with Nobukawa et al. (2016) for the whole GCXE spectrum (table 5).

In summary, in spite of significant enhancement of the GCXE fluxes near at Sgr A*(section 9.3), the $EW_{6.7}$ and $EW_{6.97}$ are nearly the same in the whole GCXE regions. The $EW_{6.4}$ is highly variable from position to position in the GCXE.

4 Local Diffuse Hot Plasma

This section reviews local hot plasmas in the hard X-ray band, or Fe XXV-Heα emitting plasmas (section 4.1) and in the soft X-ray band, or S XV-Heα emitting plasmas (section 4.2). The relevant region is $|l| \lesssim 1^\circ$ and $|b| \lesssim 0^\circ.5$, which includes the full GCXE region (section 3.1).

4.1 Hot Plasmas with the Fe XXV-Heα Line (HTP)

This section reports individual local hot plasma with the Fe XXV-Heα line. The 2 – 10 keV band luminosity of Sgr A East is $\sim 10^{35}$ erg s^{-1} , $\lesssim$10 % of the GCXE, while that of sum of the other hot diffuse sources with the Fe XXV-Heα line is $\lesssim 6 \times 10^{34}$ erg s^{-1} (2 – 10 keV), only $\lesssim$ 5 % of the GCXE luminosity.

4.1.1 Sgr A East, the Brightest SNR in the GCXE Region

Sgr A East is a non-thermal radio shell with the size of $3'.6 \times 2'.7$ (Ekers et al. 1983). Within 20 pc (∼ 10′) from Sgr A*, Sgr A East is a unique object surely identified as a young SNR. Roberts et al. (2001) found diffuse hard X-ray emissions from the position of Sgr A East with ASCA. Then, Sakano et al. (2002) detected K-shell lines from highly ionized Si, S, Ar, Ca and Fe, and established that Sgr A East has a thermal plasma.

Sakano et al. (2004) made the XMM-Newton spectra from the three annual regions of Sgr A East, the regions of radius $r < 28''$ (Center), $28'' < r < 60''$ (Middle), and $r > 60''$ (Outer). The spectra are fitted with two thermal plasmas of ∼0.9 keV and ∼3 keV (Center), ∼ 1 keV and ∼5.5 keV (Middle), and ∼ 0.9 keV and ∼4.4 keV temperatures (Outer). The highly ionized Fe-rich ejecta shows significant concentration towards the center; the Fe abundances are ∼4 solar, ∼1.5 solar and ∼0.5 solar in Center, Middle and Outer, respectively. The other elements, S, Ar and Ca are roughly uniformly distributed in the range of ∼1 – 3 solar. They interpreted that Sgr A East is a young SNR of either Type Ia (Ia-SNR) or Core-Collapsed SNR (CC-SNR) of a relatively low mass progenitor star.

With Chandra, Maeda et al. (2002) found a diffuse plasma of ∼2 keV temperature and abundances of ∼4 solar inside the radio shell. They proposed that Sgr A East is a CC-SNR with the progenitor star mass of $\sim 13 - 20 M_\odot$, and that Sgr A East is a member of young mixed-morphology (MM-SNR) (Rho & Petre 1998). Park et al. (2005) confirmed the center-filled X-ray structure. They made X-ray spectra from the three regions, named Center, North and Plume. The spectra are fitted with two-thermal plasmas of ∼ 1 keV and ∼5 keV temperatures in Center, but in North, the temperatures are ∼ 1 keV and

$\sim$11 keV. The Fe abundance shows clear concentration toward the SNR center, from $\sim$1 solar (Plume) and $\sim$2.5 solar (North), to $\sim$6 solar (Center). The iron mass of Sgr A East is estimated to be $\lesssim 0.27 M_\odot$. The abundances of lighter elements, S, Ar and Ca are roughly 1 solar, but are higher in Plume and North than Center. Therefore, the plasma in North and Plume would be the shock-heated ISM.

Park et al. (2005) found a hard point-like source, CXOGC J174545.5$-$285829 (Cannonball) at the northern edge of the SNR. It has a power-law spectrum of index $\sim$1.6, which is typical to a non-thermal synchrotron emission from a NS magnetosphere. The absorption ($N_{\rm H}$) is $\sim 17 \times 10^{22}$ cm^{-2}, similar to that of Sgr A East of $13-19\times10^{22}$ cm^{-2}, and hence Cannonball is associated to the Sgr A East SNR at the same distance. Then, the X-ray luminosity is estimated to be $\sim 3 \times 10^{33}$ erg s^{-1} (2–10 keV), which is typical to a pulsar and / or pulsar wind nebula (PWN). From these facts, they suggested that Sgr A East is a CC-SNR, and Cannonball is a high-velocity NS born in the CC-SN.

Koyama et al. (2007b) obtained a high quality X-ray spectrum of Sgr A East with Suzaku. They discovered many K-shell emission lines from highly ionized atoms, which are S XV-Heα, S XVI-Lyα, S XV-Heβ, Ar XVII-Heα, Ar XVIII-Lyα, Ar XVII-Heβ, Ca XIX-Heα, Fe XXV-Heα, Fe XXVI-Lyα, Fe XXV-Heβ+Ni XXVII-Heα and Fe XXV-Heγ+Fe XXVI-Lyβ. The flux ratios of these lines indicate that Sgr A East has, at least two thermal plasmas. With the 2-temperature CIE model fit, the plasmas temperature are found to be $\sim$ 1.2 keV and $\sim$6.0 keV, the mean abundance of Fe is$\sim$ 2.6 solar, while the other elements are $\sim$1 solar. The total and iron masses are $\sim 27 M_\odot$ and $\sim 0.15 M_\odot$, respectively, consistent with a CC-SN origin. A hint of the Mn XXIV-Heα line is found at 6.1 keV, but no hint of the Cr XXIII-Heα line at 5.6 keV is found in spite of larger abundance than Mn.

In addition to the two CIE plasmas, a non-thermal component is found, which occupies the major fraction above $\sim$7 keV. Perez et al. (2015) and Mori et al. (2015) found strong hard X-rays in the 10–40 keV band with NuSTAR from the regions including some fractions of Sgr A East. The flux at the Fe XXV-Heα lines is nearly comparable to the thermal emissions, which roughly agree to the power-law component of Koyama et al. (2007b). Perez et al. (2015) proposed that the origin of the power-law component is many faint mCVs in the region of Sgr A East. In this case, significant Fe I-Kα line flux should be observed, because mCVs are strong Fe I-Kα emitter (table 14). However no hint of strong Fe I-Kα line is found from Sgr A East.

Another possibility of the power-law component is assembly of non-thermal filaments listed in table 12 (Muno et al. 2008) plus unresolved non-thermal sources. These would be due to synchrotron emissions by HECRe accelerated by a shock wave of Sgr A East. The LECRe and possibly LECRp, may ionize the Fe XXV to higher ions of Fe XXVI, hence emit extra Fe XXVI-Lyα lines. This may lead to the large flux ratio of Fe XXVI-Lyα / Fe XXV-Heα of $\sim$0.05, corresponding to the plasma temperature of $\sim$4–6 keV, an unusually high among any known SNRs. The center energy of the Fe XXV-Heα at $\sim$6.65 keV is also the highest among the normal CC-SNRs.

Uchiyama et al. (2017) re-analyzed the Suzaku spectrum of Sgr A East spectrum by the simultaneous fitting with the GCXE spectrum of nearby sky (see section 3.3). They found a hint of recombining plasma (RP) in Sgr A East. These very high temperature plasma of $\sim$4–6 keV, RP and strong power-law component are unusual even in the normal CC-SNRs, where presence of circumstellar matter (or MC), a possible origin to make a RP, is more likely than Type Ia SNRs. These unusual structures would be related to extreme environments at the Galactic center (GC) region.

Sgr A East is an SNR of $\sim 10^3$ years age, and is located in the close vicinity of Sgr A*. Maeda et al. (2002) predicted that the dust / molecular ridge was compressed by the forward shock of the SN Sgr A East. When the blast wave passed over the black hole Sgr A*, the compressed dense dust and gas had accreted onto Sgr A*, and produced X-ray flares in $\sim$ a few 100 years ago (sections 5.2).

Totani (2006) proposed another idea that the mean accretion rate onto Sgr A* during the past $\sim 10^7$ yr had been extremely higher than the current rate. The accretion energy in the past was sufficient to produce and keep the HTP gas in the GCXE. Also a significant amount of positrons should had been created, which might produce the observed 511 keV annihilation line from the Galactic bulge. After the passage of the blast wave of the SN Sgr A East in $\sim$ a few 100 years ago, the ambient gas had been cleaned-up, leading Sgr A* to the present quiet level (section 7.1).

Sgr A East is the brightest Fe XXV-Heα source in the GCXE region. The 2–10 keV band luminosity is $\sim 10^{35}$ erg s^{-1} (Maeda et al. 2002; Sakano et al. 2004; Koyama et al. 2007b), this is only $\sim$8 % of the GCXE.

4.1.2 G0.61+0.01

Although the Fe XXV-Heα line is smoothly distributed over the Sgr B region. Koyama et al. (2007a) found a local excess of $\sim 5' \times 2'.4$ size with Suzaku. The position of the center is $(l, b) = (0.^\circ61, 0.^\circ01)$, and named Suzaku J1747.0$-$2824.5 (G0.61+0.01). The deep XMM-Newton image shows a hint of very weak enhancement near this position in the low energy band of 2–4.5 keV (Ponti et al. 2015). This source is, therefore very peculiar dominated mainly in the Fe XXV-Heα line.

The X-ray spectrum is fitted with an IP (NEI) plasma model (Koyama et al. 2007a). The best-fit plasma temperature, ionization time scale and iron abundance are $\sim$ 3 keV, $n_{\rm e}t \sim 2 \times 10^{11}$

s cm^{-3}, and $5.1^{+1.2}_{-1.1}$ solar, respectively. Then the dynamical age and ionization age are estimated to be $\sim 4 \times 10^3$ yr and $\sim 7 \times 10^3$ yr, respectively. From these results, G0.61+0.01 is likely a new ejecta dominant type Ia SNR. The absorption column density $N_{\rm H}$ is $\sim 1.6 \times 10^{23}$ cm^{-2}, and hence this SNR would be behind the Sgr B MC complex. Assuming the distance of 8 kpc, the plasma mass is estimated to be $\sim 1.3 M_\odot$, a bit smaller than the typical ejecta mass of Ia SNR.

Faint emissions are extending around G0.61+0.01. The south of this emission would be another SNR G0.57−0.001 (see section 4.1.3), but the northeast emission would be a part of G0.61+0.01. In this case, the whole plasma of G0.61+0.01 may be a bit larger than $\sim 1.3 M_\odot$, consistent with an ejecta of young Ia SNR. The X-ray luminosity of G0.61+0.01, including the faint emission at the northeast, would be at most $\sim 2 \times 10^{34}$ erg s^{-1} (2 – 10 keV), only ~ 1 % of the GCXE flux

4.1.3 G0.570−0.018 and G0.570−0.001

Senda et al. (2002) found a faint X-ray emission in the hard X-ray band images of Chandra and ASCA. The Chandra position is $(l, b) = (0.^\circ570, 0.^\circ018)$, hence named G0.570−0.018 / CXO J174702.6−282733. They fit the Chandra spectrum with a phenomenological model of a thermal bremsstrahlung plus a Gaussian line at ∼6.5 keV (Fe-Kα line), and obtained the center energy and EW$_{\rm Fe-K}$ to be 6.5 ± 0.03 keV and $4.1^{+1.4}_{-1.0}$ keV, respectively. These are consistent with the ASCA results of $6.60^{+0.12}_{-0.09}$ keV and $3.7^{+3.0}_{-1.2}$ keV. Then, they fit the ASCA and Chandra spectra simultaneously with a physical model of IP (NEI) plasma. The best-fit temperature (kT), ionization parameter ($n_{\rm e}t$) and iron abundance are ∼6 keV, $\sim 2 \times 10^{10}$cm^{-3} s and ∼4.5 solar, respectively. The absorption is $\sim 1.4 \times 10^{23}$ cm^{-2}, and hence this source would be behind the Sgr B complex. Assuming the distance of 8 kpc, the X-ray luminosity (2 – 10 keV) is estimated to be $\sim 10^{34}$ erg s^{-1}, which is only ~ 1 % of the GCXE flux.

The Chandra morphology is a ring-like structure of $\sim 10''$ radius plus a tail of $\sim 20''$ long. From this small ring and high plasma temperature, Senda et al. (2002) proposed that G0.570−0.018 is a very young SNR of ∼100 years old. The tail would be outflow plasma from this young SNR. However the INTEGRA / IBIS γ-ray and VLA radio observations by Renaud et al. (2006) revealed neither the ^{44}Ti γ-ray line nor the radio continuum feature from this very young SNR candidate.

Inui et al. (2009) made the spectra of ASCA (observed in 1994), Chandra (2000), XMM-Newton (2001), XMM-Newton (2004) and Suzkau (2005) from the circle of the radius of $2'.5$ around G0.570−0.018. They fitted all the spectra with the same model of power-law plus 3 Gaussian lines for the Fe-Kα lines fixing at 6.40, 6.67 and 6.97 keV, respectively. The best-fit Fe I-Kα line flux (6.40 keV) increased from the ASCA(1994) to Chandra (2000) and XMM(2001) by ∼2 times, then turned to decrease to XMM-Newton (2004) and Suzaku epoch (2005) by factor of ∼0.7. The Fe XXV-Heα line flux (6.67 keV) was, on the other hand, almost constant with time.

With XMM-Newton, Ponti et al. (2015) found an SNR candidate G0.570−0.001 in the close vicinity of G0.570−0.018. Since the area of Inui et al. (2009) includes both G0.570−0.001 and G0.570−0.018, one possibility is that G0.570−0.018 is a time variable Fe I-Kα source (XRN, see table 7), and G0.570−0.001 is a Fe XXV-Heα line emitting SNR candidate. However, it is still a puzzle whether G0.570−0.001 is a Fe XXV-Heα line emitting hard X-ray source or soft source with no Fe XXV-Heα line, because Ponti et al. (2015) detected G0.570−0.001 in the soft X-ray band (2 – 4.5 keV) only.

4.1.4 G359.942−0.03 and J174400−2913

With the Chandra survey observations, many small diffuse spots of $\lesssim 10''$ size are found (e.g. Muno et al. 2008; Lu et al. 2008; Johnson et al. 2009, see section 6). Most of them are feature-less non-thermal emissions, but a few sources exhibit strong Fe-Kα lines. Johnson et al. (2009) found a Fe XXV-Heα line source, named G359.942−0.03. The spectrum is fitted with a thin thermal plasma model with ∼7 keV temperature and absorption of $\sim 2 \times 10^{23}$ cm^{-2}. The EW$_{6.7}$ is ∼0.8 keV. These are similar to the HTP. The detection of the Fe XXV-Heα line from G359.942−0.03 is, however, a bit confusing possibly due to the limited statistics, because Muno et al. (2008) reported no significant Fe-Kα line (EW$_{\rm Fe-K} \lesssim 180$ eV) from possibly the same source, named G359.941−0.029 (see table 12).

Yamauchi et al. (2014) found another Fe XXV-Heα line source, named Suzaku J174400−2913. The spectrum is fitted with a CIE plasma of ∼4 keV temperature and ∼0.6 solar abundance. The position coincides to a narrow X-ray filament (∼ $10''$) of G359.55+0.16 (Johnson et al. 2009). This source would be aligned with the radio non-thermal filament G359.54+0.18 (Yusef-Zadeh et al. 1997; Wang et al. 2002a; Lu et al. 2003). The strong Fe XXV-Heα line from G359.55+0.16 is a bit confusing, because no Fe XXV-Heα line has been reported (Wang et al. 2002a; Lu et al. 2003; Johnson et al. 2009). However the statistic of Yamauchi et al. (2014) is highest, high enough to conclude that the Fe XXV-Heα line from Suzaku J174400−2913 is a robust result.

The presences of strong Fe XXV-Heα lines of these sources are similar to young SNRs. However the filament-like morphologies with small sizes ($\lesssim 10''$) and the X-ray luminosity of $\sim 2 \times 10^{33}$ erg s^{-1} (2 – 10 keV) is one or two orders of magnitude smaller than the usual young SNRs. Therefore, these sources would be either small fragments of young SNR, or in other origins such as a filament produced by magnetic field reconnection and confined by the magnetic field, or a ram pressure confined stellar wind bubble generated by a massive star (Johnson et al. 2009). Since these X-ray filaments are very faint

($\sim 10^{33}$ erg s^{-1}), contributions to the HTP flux in the GCXE would be negligible.

4.1.5 Sgr B2 Star Cluster

Sagittarius B2 (Sgr B2) is a giant MC complex, located at the projected distance of $\sim$100 pc from the Galactic center Sgr A*, and is one of the richest star-forming regions (SFRs) in our Galaxy. It contains many compact H II regions (e.g. Benson & Johnston 1984). Thus, Sgr B2 harbors many clusters of very young high-mass stellar objects (YSOs).

With Chandra, Murakami et al. (2001b); Takagi et al. (2002) found about one and half dozens of compact sources in the Sgr B2 region of $\sim 3' \times 3.5'$ area. These sources are likely YSOs. The brightest 2 sources at the compact HII region, Sgr B2 Main, are slightly extended with sizes of $3''$ and $5''$ radii. The spectra are fitted with a CIE plasma of $\sim$1 solar abundance. The best-fit temperature and luminosity are in the range of $\sim$5 – 10 keV and $\sim 10^{33}$ erg s^{-1} (2 – 10 keV), respectively. Another bright source at the position of Sgr B2 North of $25'' \times 21''$ in size has the luminosity of $\sim 10^{33}$ erg s^{-1}. From the extended natures and large luminosity, these three sources are likely clusters of YSOs.

The combined spectrum of the other point sources is fitted with a CIE plasma model. The best-fit temperature is $\sim$10 keV. The individual luminosity is in the range of $\sim 2 \times 10^{31}$ – 10^{32} erg s^{-1}. The temperature is higher than, but the luminosity is typical to the YSOs. Since no IR nor radio counterpart is found, an alternative idea of these thermal X-ray emissions are isolated white dwarfs powered by the Bondi-Hoyle accretion from the dense cloud gas. In any origin, these are surely Fe XXV-Heα line emitters, which contribute to the HTP of the GCXE. The total luminosity is $\sim 5 \times 10^{33}$ erg s^{-1}(2 – 10 keV), which is $\sim$5 % of the total X-ray flux of the Sgr B complex. The major X-ray fraction of the Sgr B complex is a diffuse non-thermal emission with prominent Fe I-Kα lines (the XRN, section 5.1.1).

4.1.6 Arches Star Cluster

The Arches cluster is one of the most massive star clusters near the GC. It has a total mass of $\sim 10^4\, M_\odot$ within a compact size of $\sim$0.5 – 1 pc diameter. Yusef-Zadeh et al. (2002b); Law & Yusef-Zadeh (2004) detected 2 compact X-ray sources (A2, A1 N/S) in addition to the diffuse emission from the central region using Chandra.

Wang et al. (2006b) reported that the 2 sources are separated to 3 point sources (A1N, A1S and A2), which exhibited bright Fe XXV-Heα lines with temperatures of $\sim$1.8 keV, $\sim$2.2 keV and $\sim$2.5 keV, respectively. Diffuse thermal emission with a strong Fe XXV-Heα line is also found near the cluster center of $\leq 15''$ radius. The luminosity is $\sim 4 \times 10^{33}$ erg s^{-1} (2 – 8 keV), about 20 % of the sum of A1N, A1S and A2. The total luminosity of the thermal plasma of A1N, A1S, A2 and central diffuse source is $\sim 3 \times 10^{34}$ erg s^{-1} (0.3 – 8 keV), $\sim$2 % of the GCXE.

The Suzaku spectrum of the whole cluster region is fitted with a two-component model, a CIE plasma of $\sim$1 solar abundance, and a power-law component with a Fe I-Kα line (Tsujimoto et al. 2007). The best-fit temperature of the CIE plasma is $\sim$ 2 keV, and hence exhibits strong Fe XXV-Heα lines. The luminosity of the CIE plasma is $\sim 10^{34}$ erg s^{-1} (3 – 10 keV). About half of the X-rays are largely extended diffuse emission of power-law spectrum with strong Fe I-Kα lines (section 5.2.1).

Capelli et al. (2011a) examined long term X-ray emissions observed with XMM-Newton in 2002 – 2009. They found a clear flare with the flux increase of $\sim$70 % above the quiescent level. The spectrum in the quiescent state shows both the Fe XXV-Heα and Fe I-Kα lines, and hence the spectrum is a combination of thermal plasma (Fe XXV-Heα line) and non-thermal component (Fe I-Kα line). The best-fit temperature of the thermal plasma is $\sim$ 1.7 keV, in good agreement with those of Suzaku (Tsujimoto et al. 2007) and Chandra (Wang et al. 2006b). The total luminosity (2 – 10 keV) is $\sim 1.5 \times 10^{34}$ erg s^{-1}. The luminosity ratio between the thermal plasma and non-thermal component is 0.85 : 0.15, which seems inconsistent with Tsujimoto et al. (2007). However, taking account of the diffuse nature of the Fe I-Kα line and larger correction area of Tsujimoto et al. (2007), the flux ratios may be consistent with each other. The flare spectrum does not show significant emission of the Fe I-Kα line, in contrast to the quiescent spectrum. This also supports that the Fe I-Kα line is different origin from the higher ionization Fe XXV-Heα line. The flare spectrum is described well by a CIE plasma of $\sim$ 1.8 keV temperature. The total luminosity is $\sim 3 \times 10^{33}$ erg s^{-1}, one of the largest flares of YSOs.

4.1.7 Other Young Star Clusters

Baganoff et al. (2003) found central diffuse emission of a size of $10''$ radius in the immediate vicinity of Sgr A*, where Central Star Cluster (CSC) is included. The spectrum is fitted with a thermal plasma of $\sim$ 1.3 – 1.6 keV temperature. The luminosity is $\sim 2 \times 10^{34}$ erg s^{-1} (2 – 10 keV). The spectrum has a Fe-Kα line at $6.5^{+0.1}_{-0.2}$ keV, the energy between the Fe I-Kα and Fe XXV-Heα lines. They interpreted that the lower line energy than 6.7 keV is due to ionizing hot plasma (IP). More plausible idea is that the Fe-Kα line is a mixture of Fe I-Kα (CG) and Fe XXV-Heα (HTP). The luminosity of the hot plasma is significantly higher than that of single YSO, and hence likely origin is a cluster of YSO, including colliding winds of OBs and W-R stars.

The Sgr D complex is composed of Sgr D H II or G1.13−0.10, and an SNR, Sgr D SNR or G1.0−0.1 (Downes

et al. 1979; Downes & Maxwell 1966). Sawada et al. (2009) found a hard diffuse X-ray spot (Diffuse Source 2: DS2) in the radio shell of Sgr D H II. The spectrum of DS2 is a high temperature plasma of $\sim$4 keV, accompanied by a Fe XXV-Heα line, possibly, a cluster of YSO in the non-thermal radio shell.

Nobukawa et al. (2017a) found faint hard X-ray emissions from the Sgr D SNR region. Remarkable discovery is an extremely high Ni abundance of $\sim$30 solar from the northeast shell of the SNR. Such a large Ni abundance has not been predicted by any model of normal SNR. This anomalous structure would be due to some extreme circum stellar conditions in the GCXE region. One possible scenario is that Sgr D SNR is a CC-SN, and the SN explosion was highly asymmetric so that a part of the neutron-rich (Ni) inner core region was ejected perennially to the northeast shell of the SNR.

Sgr C is also a MC complex, and hence could be Fe XXV-Heα line sources like Sgr B, Arches and Sgr D. However, no hot plasma with a Fe XXV-Heα line is found, except lower temperature plasmas with a S XV-Heα line (section 4.2.7), and hence Sgr C would not contribute to the HTP in the GCXE.

Sgr A is another MC complex, which is associated with many XRNe (table 9). Although no compact point source with a Fe XXV-Heα line is found from the Sgr A complex due to the very crowded region, some fractions of HTP may come from this region, possible activities of YSOs.

Law & Yusef-Zadeh (2004) found 4 X-ray point sources and diffuse emission from the Quintuplet cluster with the luminosity of $\sim 10^{33}-10^{34}$ erg s^{-1}. Wang et al. (2006b) found 8 X-ray sources in the Quintuplet region. Since the X-ray properties are largely different, they combined 3 bright sources with similar properties (QX2, QX3 and QX4), and fit the spectrum with a CIE model. The best-fit kT and $N_{\rm H}$ are $\sim$8 keV and $\sim 6\times10^{22}$ cm^{-2}, respectively. The total luminosity is $\sim 8\times10^{32}$ erg s^{-1}. An extended emission also found with luminosity and temperature of $\sim 3\times10^{33}$ erg s^{-1} and $\sim$ 10 keV, respectively.

In summary, the total luminosity of the young star clusters with the Fe XXV-Heα lines is larger than that of the other diffuse hot plasma excluding Sgr A East. The sum of the luminosity of all the young clusters (both point sources and diffuse plasma) in the GC, would not exceed $\sim$5 % of the GCXE, even if contributions of undetected X-ray faint young star clusters are taken into account.

4.2 S XV-Heα Sources (LTP)

The soft X-ray plasmas with the size of $\lesssim 10'$ are given in this section. Most of them exhibit strong Si XIII-Heα and S XV-Heα lines with a moderate temperature of $\sim$1 keV, and hence these are likely intermediate-old SNRs. However, some of them show unusual structures as SNRs either in morphology or spectrum. This would be closely related to extreme ISM environment near at the GC. These soft X-ray plasmas may contribute significant fractions to the LTP flux, but the contribution to the HTP would be ignored.

4.2.1 G0.42−0.04 (G0.40−0.02), G1.2−0.0 and G0.13−0.12

In the soft X-ray band map of Suzaku, Nobukawa et al. (2008) found an excess spot with elliptical shape of $\sim 1'.8\times 2'.4$ at $(l,b)=(0^\circ.42, -0^\circ.04)$, hence named G0.42−0.04 (Suzaku J1746.4−2835.4). The source has a S XV-Heα line at $\sim$2.45 keV, a cut-off below $\sim$2 keV, and a steep slope above $\sim$4 keV. The spectrum is fitted with a CIE plasma model with the temperature and abundances of $\sim$0.7 keV, and $\sim$0.9 solar, respectively. The absorption column of $\sim 8\times10^{22}$ cm^{-2} is consistent with the Galactic center (GC) distance of 8 kpc. Then, the physical size of the ellipse is $\sim$5.6 pc$\times$4.2 pc. The X-ray luminosity is estimated to be $\sim 6\times10^{33}$ erg s^{-1} (2 – 10 keV). These values are consistent with an intermediate-old aged SNR.

Ponti et al. (2015) found a larger ellipse at $(l,b)=(0^\circ.40, -0^\circ.02)$, named G0.40−0.02, with the size of $\sim 4'.7\times7'.4$. The spectrum is fitted with a CIE plasma with the temperature and absorption column of $\sim$0.55 keV and $\sim 8\times10^{22}$ cm^{-2}, respectively, both are similar to those of G0.42−0.04. Therefore, G0.40−0.02 and G0.42−0.04 would be the same object with the distance of 8 kpc. Then, the physical size of G0.40−0.02 is $\sim$11 pc$\times$17 pc. They estimated that the dynamical age and thermal energy of G0.40−0.02 are $\sim$3700 years and $\sim 1.9\times10^{50}$ erg, respectively.

From the radio SNR candidate G1.0−0.1 in the Sgr D complex (Downes et al. 1979), Sidoli et al. (2001) found a faint diffuse soft X-ray with BeppoSAX, but Suzaku found no soft X-ray from G1.0−0.1(Sawada et al. 2009). Instead, Sawada et al. (2009) found an elliptical X-ray spot (Diffuse Source 1: DS1) with the size of $\sim 4'\times7'$ at the northeast of the radio shell Sgr D H II. From the position, the spot DS1 is named G1.2−0.0. The spectrum of G1.2−0.0 has Heα lines of S, Ar and Ca, and hence is fitted with a CIE plasma of $\sim$0.9 keV temperature. The abundances of S, Ar and Ca are $\sim$1.6, $\sim$1.8 and $\sim$1.8 solar, respectively. The X-ray absorption is $\sim 8.5\times10^{22}$ cm^{-2}, possibly in or behind the Sgr D MC complex. Assuming the distance to be 8 kpc, the size is estimated to be $\sim$ 8 pc$\times$16 pc. The plasma temperature, abundances and size suggest that G1.2−0.0 is an intermediate-old aged SNR. They reported that the unabsorbed luminosity in the 0.7 – 8 keV band is 1.4×10^{35} erg s^{-1}. However, this luminosity would be a subject of large ambiguity due to the large $N_{\rm H}$ for the soft spectrum.

In the XMM-Newton image, Heard & Warwick (2013b) discovered a diffuse soft X-ray spot of a circle of $1.5'$ radius near the X-ray filament G0.13−0.11 (section 6). From the position, this source is named G0.13−0.12. The X-ray spectrum is fitted with a CIE plasma of $\sim$1.1 keV temperature. The absorp-

tion is $\sim 5.6 \times 10^{22}$ cm^{-2}, consistent with being a GC source. Then, the X-ray luminosity is $\sim 2.2 \times 10^{34}$ erg s^{-1} (2 – 10 keV). The abundances of Si, S and Ar are ∼1.4, ∼2.0 and ∼3.4 solar, respectively. These values are consistent that G0.13−0.12 is an intermediate-aged SNR. Since massive MC, G0.13−0.13 is present in this region, alternative idea is a hot Inter Stellar Medium (ISM), or Circum Stellar Medium (CSM) plasmas heated by powerful stellar winds.

4.2.2 G359.79−0.26 and G359.77−0.09

Mori et al. (2008); Mori et al. (2009) found two bright diffuse spots, G359.79−0.26 and G359.77−0.09 in the Suzaku S XV-Heα line image near the GC. The sizes are $\sim 4.0' \times 2.6'$ and $\sim 4.9' \times 2.4'$, respectively. They reported that the X-ray spectra of G359.77−0.09 and G359.79−0.26 are fitted with a CIE plasma model, with the temperatures of ∼0.7 and ∼1.0 keV, respectively. The diffuse source G359.77−0.09 exhibits clear Heα lines of Si, S, and Ar with abundances of ∼0.9 solar, ∼0.7 solar and ∼0.9 solar, respectively. The other diffuse source G359.79−0.26 exhibits Heα lines of Mg, S, S, Ar and Ca with abundances of ∼1.3, ∼1.1, ∼1.4, ∼1.7 and ∼1.4 solar, respectively. The absorption column densities of G359.79−0.26 and G359.77−0.09 are $\sim 5 \times 10^{22}$ cm^{-2} and $\sim 7 \times 10^{22}$ cm^{-2}, consistent with GC sources at 8.0 kpc, and hence the sizes of G359.79−0.26 and G359.77−0.09 are ∼9.3 pc×6 pc and ∼11.4 pc×5.6 pc, respectively. The luminosity is in the range of $\sim 4 - 6 \times 10^{33}$ erg s^{-1}. In the XMM-Newton image, Heard & Warwick (2013b); Ponti et al. (2015) confirmed the soft X-ray sources , G359.79−0.26 and G359.77−0.09. The plasma temperatures, absorptions, abundances and luminosity are all consistent with Mori et al. (2008); Mori et al. (2009).

Although, the two SNR candidates, G359.79−0.26 and G359.77−0.09 are spatially separated by $\sim 0^\circ.2$, all the physical parameters are nearly the same. These sources make-up a single elliptical ring with the diameters and width of $\sim 20' \times 16'$ and $\sim 6' - 9'$, respectively. The X-ray spectrum from the ring is fitted with a CIE plasma model of ~ 0.9 keV temperature and the Si, S and Ar abundances of ∼1.0, ∼1.2 and ∼1.4 solar, respectively. The thermal energy of the ring is $\sim 10^{51}$ erg. Therefore, the ring and the two sources G359.79−0.26 and G359.77−0.09 would be comprised a single source, a super bubble (SB) with diameter and width of ∼40 – 50 pc and ∼15 – 20 pc, respectively. Since the shape of the ring is nearly symmetry with respect to the center point at $(l, b) = (359^\circ.83, -0^\circ.14)$, an alternative idea would be that the ring is a hyper nova remnant (Mori et al. 2009; Heard & Warwick 2013b).

4.2.3 Diffuse Soft Sources Near Sgr A* (NW, SE, E)

In the Chandra image near Sgr A*, Baganoff et al. (2003) found diffuse sources, named NW and SE. Since these are bright in the 1.5 – 6 keV band, but weak in the 6 – 7 keV band images, these are soft X-ray sources, unrelated to the Sgr A East SNR. Instead, they proposed these are bipolar-flows from Sgr A*, although no spectral information was available. In the XMM-Newton X-ray image near Sgr A*, Heard & Warwick (2013b) found three diffuse sources with the size of $\sim 1' \times 0'.7$, $\sim 1'.7 \times 1'$ and $\sim 1' \times 1'$, and named NW, SE and E. The sources, NW and SE are the same sources of Baganoff et al. (2003).

The spectra of NW, SE and E are fitted with a CIE plasma of ~ 0.9 keV, ~ 1.1 keV and ~ 1.0 keV temperatures. The Si, S and Ar abundances are in the range of ∼1.0 – 0.6, ∼0.6 – 0.9 and ∼0.7 – 1.5 solar, respectively. The absorptions of NW, SE and E are $\sim 8 \times 10^{22}$, $\sim 6 \times 10^{22}$ and $\sim 6 \times 10^{22}$ cm^{-2}, respectively, consistent with the GC distance of 8 kpc. Then, the sizes of NW, SE and E are estimate to be $\sim 2.3 \times 1.6$, $\sim 4.0 \times 2.3$ and $\sim 2.3 \times 2.3$ pc^2, respectively, while the luminosity (2 – 10 keV) is $\sim 1.5 - 2.7 \times 10^{34}$ erg s^{-1}. The temperatures, abundances and luminosity are similar to, but the sizes are significantly smaller than, those of the intermediate-aged SNRs. Heard & Warwick (2013b) estimated the electron densities of NW, SE and E to be ∼4.6 – 9.9 cm^{-3}, significantly higher than that of ISM or CSM. The small size of elongated shape pointing to Sgr A*, high density and closeness from Sgr A*, lead to an alternative scenario that NW, SE and E are outflows from Sgr A* (section 7.3).

4.2.4 G359.1−0.5: A Recombining Plasma

G359.1−0.5 is a shell-like radio SNR with the size of $\sim 10'$ in radius (Downes et al. 1979). Center-filled thermal X-rays are found with ASCA (Bamba et al. 2000), and hence G359.1−0.5 is a MM-SNR. The X-ray spectrum has prominent Si XVIII-Heα and S XVI-Lyα lines. This is very peculiar because S is more highly ionized (H-like) than the lighter element Si (He-like).

Ohnishi et al. (2011) observed G359.1−0.5 with Suzaku and made a high quality spectrum. The problem of the peculiar spectrum of ASCA is solved by adding radiative recombination continuum (RRC), a saw-teeth continuum shape made by a transition of free electrons to the K-shell of Si XIII and S XV. The strong RRC structures indicate that the plasma is in over-ionization (recombining plasma: RP). In fact, the observed spectrum is well-fitted by a RP model.

The best-fit $N_{\rm H}$ of $\sim 2 \times 10^{22}$ cm^{-2} seems smaller than that of the GCXE. However, taking account of the small e-folding latitude of $\sim 0^\circ.25$ of the GCXE (tables 3, 4), this value is consistent with that G359.1−0.5 is located near the boundary of the GCXE.

TeV gamma ray emission (HESS J1745−303) and a hint of the Fe I-Kα line are found near this SNR (Aharonian et al. 2008; Bamba et al. 2009). Since the Fe I-Kα line is hardly produced in this low-temperature SNR, this would be due to a bombardment of low energy cosmic rays (LECR) to a sur-

rounding cool MCs. These LECRs would preferentially ionize Si and S, and would make a RP. The other idea to make a RP is cooling of electrons by thermal conduction to adjacent MCs or adiabatic expansion when the shock breaks thorough a surrounding dense MC gas to a tenuous ISM. These MCs should be more numerous in the GC region compared to the other regions of the Galaxy. The ratio of the ionization temperature ($\sim$0.8 keV) to the electron temperature ($\sim$0.3 keV) of G359.1$-$0.5 is the largest among the known $\sim$ 10 RP-SNRs (e.g. Koyama 2014; Sato et al. 2014; Washino et al. 2016), suggesting some extreme MC, ISM or CSM conditions are presented in the GC, or near around G359.1$-$0.5.

4.2.5 G359.41$-$0.12 and Chimney

Tsuru et al. (2009) found an ellipse and a chimney-like structure in the S XV-Heα line image of Suzaku near the Sgr C complex region. These are named G359.41$-$0.12 and Chimney. The morphology of Chimney is similar to a PWN with NS moving to one direction. However no NS candidate, is found at the head region. Furthermore, the spectrum is fitted with a CIE plasma model with $\sim$1.2 keV temperature. The spectrum of G359.41$-$0.12 is also fitted with a CIE plasma model of $\sim$0.9 keV temperature. The absorption columns of G359.41$-$0.12 and Chimney are very large and are nearly the same of $\sim 1.2 \times 10^{23}$ and $\sim 1.0 \times 10^{23}$ cm^{-2}, respectively. The abundances of S and Ar are both $\sim$1.7 solar. These indicate that G359.41$-$0.12 and Chimney are in the same origin located at the same distance on the same line-of-sight, possibly just behind a dense MCs in the Sgr C complex at 8 kpc. The X-ray luminosity (1.5 – 8 keV) of G359.41$-$0.12 and Chimney are, then estimated to be $\sim 2-4 \times 10^{34}$ erg s^{-1}.

The sum of the thermal energies of G359.41$-$0.12 and Chimney is estimated to be $\sim 1.4 \times 10^{50}$ erg. The dynamical time scales of G359.41$-$0.12 and Chimney are $\sim 2.5 \times 10^4$ and $\sim 4 \times 10^4$ years, respectively. These values are typical to a single Galactic SNR. Tsuru et al. (2009) proposed that Chimney is an outflow plasma, extending about 30 pc from an SNR candidate G359.41$-$0.12. However the highly collimated outflow of $\sim$5 pc width and $\sim$30 pc length, emanating from G359.41$-$0.12 is very unusual as the result of a single SN. One possibility is that many MCs in the Sgr C complex deformed a spherical SN expansion to the outflow like expansion. Still to make a highly collimated uni-polar structure would be difficult. Some other extreme conditions of ISM in the GCXE or near at Sgr C complex would have a responsibility on the outflow like morphology of Chimney.

4.2.6 Diffuse Plasma Near 1E 1740.7$-$2942

1E 1740.7$-$2942 is the brightest XB near the GC region. Since the time variability and spectral behavior are similar to those of the low state of Cygnus X-1, the archetypal BH candidate, 1E 1740.7$-$2942 would be another BH candidate. It is named the Great Annihilator (GA), because a hint of electron-positron annihilation line at 511 keV was found (e.g. Sunyaev et al. 1991). Although, no further evidence for the annihilation line has been found so far by other instruments, this source has drawn great attentions, because non-thermal double jet-like structures were found in the radio band. Thus, the GA is referred as a micro quasar (Mirabel et al. 1992).

Two diffuse X-ray sources are found around the GA (Nakashima et al. 2010). One is M359.23$-$0.04, a bright Fe I-Kα spot (see section 5.3.2), and the other is a thermal plasma source G359.12$-$0.05, near the position of the radio SNR G359.07$-$0.02 (LaRosa et al. 2000). The spectrum of G359.12$-$0.05 is fitted with a CIE plasma model of $\sim$0.9 keV temperature and absorption column of $\sim 7 \times 10^{22}$ cm^{-2}. The abundances of Si, S and Ar are $\sim$1.2, $\sim$1.4 and $\sim$1.5 solar, respectively.

The $N_{\rm H}$ is typical column density of the GC region of $\sim 6 \times 10^{22}$ cm^{-2}, and hence G359.12$-$0.05 is a GC source at 8 kpc. From the $\sim$0.9 keV temperature, radius of $\sim 12'$ and flux of $\sim 6.3 \times 10^{-4}$ photons^{-1} cm^{-2}, the luminosity and dynamical age are estimated to be $\sim 5 \times 10^{33}$ erg s^{-1} (1 – 10 keV, absorbed flux) and $\sim 6 \times 10^4$ yr, respectively. These values are consistent with an intermediate-old aged SNR, and hence G359.12$-$0.05 comprises a unique system, an SNR associated with a black hole candidate, the GA or micro quasar.

4.2.7 Other SNR Candidates with Soft X-Rays

Ponti et al. (2015) found 3 diffuse soft X-ray sources, named G0.52$-$0.046, G0.570$-$0.001 and G0.224$-$0.032 with the deep survey of XMM Newton. The soft source G0.570$-$0.001 is located in the close vicinity of the hard X-ray source G0.570$-$0.018 (section 4.1.3), but these two are separate sources. The spectra of G0.52$-$0.046, G0.570$-$0.001 and G0.224$-$0.032 are fitted with thermal plasmas of temperatures of $\sim$0.8, 0.6 (fixed) and $\sim$0.5 keV, with absorption columns ($N_{\rm H}$) of $\sim 8 \times 10^{22}$, $\sim 1 \times 10^{23}$ and $\sim 7 \times 10^{22}$ cm^{-2}, respectively, and hence these are likely located near the GC. In the GC distance of 8 kpc, the plasma sizes are $\sim 6 \times 12$ pc^2, $\sim 4 \times 7$ pc^2 and $\sim 5 \times 11$ pc^2, respectively. The dynamical ages and the total thermal energies are $\sim$1700, $\sim$1600 and $\sim$1800 years, and $\sim 5 \times 10^{49}$, $\sim 3 \times 10^{49}$ and $\sim 3 \times 10^{50}$ erg, respectively. As is noted in section 4.1.3, a possibility that G0.570$-$0.001 is a Fe XXV-Heα line emitting hard X-ray source, is not fully excluded.

5 The Fe I-Kα Clumps

The Fe I-Kα line distribution in the GCXE is not uniform, but clumpy as is shown in figure 5. The Fe I-Kα flux from these clumps occupy nearly half of that in the GCXE. This section re-

views the local diffuse sources, which emit strong Fe I-Kα lines (Fe I-Kα clumps). The mechanisms of the Fe I-Kα emission and results of the EW$_{6.4}$ values are given in section 5.1. The Fe I-Kα clumps with origins of past big flares of Sgr A* are given in section 5.2, while the Fe I-Kα clumps with the other origins than the Sgr A* flare are in section 5.3.

5.1 Mechanisms of the Fe I-Kα Emission and EW$_{6.4}$

When an X-ray or a low-energy cosmic ray (LECR) hits a neutral Fe atom in a cold cloud, an electron hole is made in the K-shell of the neutral Fe (K-shell ionization). Then another electron in the L-shell falls to the hole, and re-emit a characteristic X-ray at 6.4 keV. This process produces an Fe I-Kα line. If the K-shell ionization source is an X-ray of a power-law spectrum with the photon index Γ, $I(E) \propto E^{-\Gamma}$, the EW$_{6.4}$ is given by;

$$EW_{6.4} = 4 \left(\frac{1}{\Gamma+2}\right) \left(\frac{6.4}{7.1}\right)^{\Gamma} \left(\frac{1}{1+\cos^2\theta}\right) \mathrm{keV} \quad (4)$$

, where the fluorescent yield ($Y_{\mathrm{K}\alpha}$) , the density ratio of iron to electron ($n_{\mathrm{Fe}}/n_{\mathrm{e}}$) , the differential Thomson scattering cross section ($d\sigma_{\mathrm{T}}/d\Omega$) , and the photo-absorption cross section by Fe atoms (σ_{Fe}) are ~ 0.34, $\sim 4\times10^{-5}$, $\sim 4.0\times10^{-26}(1+\cos^2\theta)\,\mathrm{cm}^2$, and $2\times10^{-20}(E/7.1\mathrm{keV})^{-3}\,\mathrm{cm}^2$, respectively. In a typical value of $\Gamma = 1.5$ and scattering angle of $\theta = 90^\circ$, the EW$_{6.4}$ is $\sim$1 keV. The Fe I-Kα line flux is proportional to N_{H}, when the target cold gas is optically thin, or N_{H} is $\lesssim 10^{24}\,\mathrm{cm}^{-2}$. Therefore, in order to produce detectable Fe I-Kα line flux as is shown in figure 5, the absorption K-edge of the neutral Fe at 7.1 keV should be large enough of $N_{\mathrm{H}} \gtrsim 10^{23}\,\mathrm{cm}^{-2}$.

If the K-shell ionization source is a charged particle with the number distribution of power-law function of $N(E) \propto E^{-\Gamma}$, the EW$_{6.4}$ is given as a function of the spectral index (Γ) (Dogiel et al. 2011). In the case of an electron, the EW$_{6.4}$ is $\sim$250 – 400 eV, almost independent of Γ. In the case of protons, the EW$_{6.4}$ depends largely on Γ. In the normal case that Γ is $\gtrsim$1, the EW$_{6.4}$ is $\gtrsim$1 keV.

The largest cross sections of the K-shell ionization of protons and electrons are around the energy of a few $\sim$10 MeV, and a few $\sim$ 10 keV, respectively (Tatischeff et al. 2012). The particle of these energy is called the Low Energy Cosmic Ray proton (LECRp) or the Low Energy Cosmic Ray electron (LECRe). Both the LECRp and LECRe can penetrate only $N_{\mathrm{H}} \lesssim 10^{22}\,\mathrm{cm}^{-2}$. Therefore, if the absorption depth of the iron K-edge at 7.1 keV is shallow of $N_{\mathrm{H}} \lesssim 10^{22}\,\mathrm{cm}^{-2}$, the ionization source is likely an electron or proton.

5.2 X-ray Reflection Nebula (XRN)

In figure 5, bright Fe I-Kα clumps are found in the MC complexes of Sgr A, B, C, D and E in the Central Molecular Zone (CMZ). The spectra have a mean EW$_{6.4}$ of $\sim$1 keV and a pronounced edge structure at 7.1 keV of $N_{\mathrm{H}} \sim 10^{23} - 10^{24}\,\mathrm{cm}^{-2}$. Thus the origin of the bright Fe I-Kα clumps would be an X-ray irradiation. The flux and morphology are often variable in the time scale of a few – 10 years. This section overviews the bright Fe I-Kα line clumps, named the X Ray Reflection Nebulae (XRNs), and discuss the nature, structure and origin of the XRNe.

5.2.1 Sgr B: A Prototype of the X-ray Reflection Nebula (XRN)

As is noted in section 2.2, the XRN scenario of the Fe I-Kα line from the Sgr B2 clouds is proposed by Koyama et al. (1996); Murakami et al. (2000) with the ASCA observation. BeppoSAX found hard X-ray emission from the Sgr B2 cloud (Sidoli et al. 2001), but the line center energy of 6.5 ± 0.07 keV is higher than those from Koyama et al. (1996); Murakami et al. (2000), and any other later observations with better energy resolution instruments (see table 7).

With Chandra, Murakami et al. (2001b) found a diffuse emission of nearly one order of magnitude brighter than those of the X-ray emitting young stars in the Sgr B regions (section 4.1.5). The morphology is a convex shape of $\sim 2' \times 4'$ size facing to Sgr A*. The X-ray peak is shifted from the core of the MC toward Sgr A* by $\sim 1'$. The X-ray spectrum exhibits pronounced Fe I-Kα, Fe I-Kβ lines, deep Fe I K-edge at 7.1 keV and large photoelectric absorption at low energy. The absorption-corrected X-ray luminosity is $\sim 10^{35}\,\mathrm{erg\,s}^{-1}$. These are nearly the same as the ASCA results. Using the best-fit spectral parameters and the geometry of the MC, Murakami et al. (2001b) simulated the X-ray properties with the XRN scenario in the case that N_{H} is larger than $10^{24}\,\mathrm{cm}^{-2}$. Their simulation successfully reproduced the convex morphology and the peak shift of $\sim 1'$ toward the GC or Sgr A*. Thus, the X-ray morphology and spectrum are all well explained by the XRN scenario, where the irradiation source is located toward the GC, or Sgr A* itself.

The Suzaku observations by Koyama et al. (2007a) provided separate maps of the Fe I-Kα and Fe XXV-Heα lines. Although the Fe XXV-Heα line is smoothly distributed over the Sgr B region except a faint clump of the SNR candidate G0.61−0.01 (section 4.1.2), the Fe I-Kα line image is more clumpy with local excesses at the positions of the Sgr B2 cloud and at $(l, b) = (0.^\circ74, -0.^\circ09)$. The latter clump is called M0.74−0.09 (see figure 5).

The Fe XXV-Heα line flux is constant with time in all the regions including near the Sgr B complex. By contrast, a time variability of the Fe I-Kα line in the Sgr B complex regions is discovered for the first time by Koyama et al. (2008) between the Chandra and Suzaku observations separated by 5 years. The time variability is confirmed by the more extended data set from ASCA, Chandra, XMM-Newton and Suzaku in the time span of more than 10 years (Inui et al. 2009). The long term time

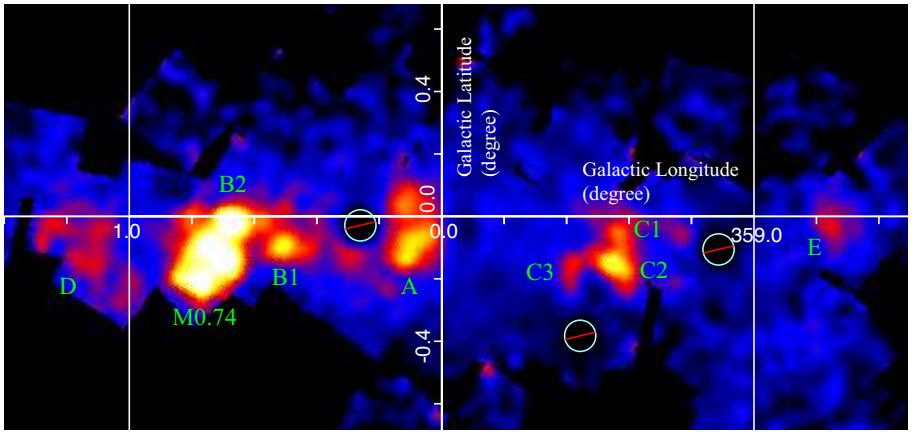

Fig. 5. The XRN complexes near the Galactic center: Sgr D, B (M0.74, B2, B1), A, C (C3, C2, C1), and E (from the left to the right). The white circles are positions of bright X-ray binaries and are excluded from this map (From unpublished Suzaku results).

Table 7. 6.4 keV clumps near the Sgr B complex

Name (l, b)∗	$N_{\rm H}$ (10^{22}cm^{-2})	$EW_{6.4}$ (keV)	$F_{\rm x}$ (4–10 keV)⋆ (10^{-12} erg s^{-1} cm^{-2})	Area (arcmin^2)	Vari#	Instrument† Reference‡
Sgr B2 $(0.66, -0.05)$	83^{+25}_{-20}	$2.9^{+0.3}_{-0.9}$	13	28	-	A, a
Sgr B2 $(0.66, -0.04)$	88^{+20}_{-15}	2.1 ± 0.2	12	11	-	C, b
Sgr B2 $(0.7, -0.04)$	40 ± 15	2.2 ± 0.1	4.5	13	-	B, c
Sgr B2 $(0.66, -0.03)$	50 ± 13	$1.2^{+0.7}_{-0.3}$	1.9 ± 0.2 (10 –40 keV)	7	Y	N+X, j
Sgr B2 (0.66−0.03)	96^{+25}_{-8}	$1.13^{+0.05}_{-0.02}$	11	9	-	S, f
M0.74−0.09	40^{+14}_{-11}	$1.55^{+0.37}_{-0.26}$	3.0	9		
Sgr B2 $(0.67, -0.02)$	84^{+38}_{-12}	-	4.3 (5–10 keV)‖	9	Y	S, i
Sgr B2 $(0.67, -0.02)$	88^{+38}_{-12}	-	2.1 (5–10 keV) ∗∗	9	Y	
M0.74−0.09	57±6	-	1.7 (5–10 keV) ‖	7	Y	
M0.74−0.09	65±18	-	0.9 (5–10 keV) ∗∗	7	Y	
G0.66−0.13	30^{+38}_{-9}	-	0.9 ± 0.1 (10–40 keV)	9	Y	N+X, j
G0.570−0.018	$13.9^{+3.3}_{-3.2}$	-	1.2–1.5 (2–10 keV)	20	Y	C, d, h
Sgr B1 (0.51, −0.10)	15^{+2}_{-1}	1.4±0.3	2.2 (2–10 keV)	22	-	S, g
Sgr B1+G0.570	-	0.57±0.07	9.7 (2–8 keV)	77	-	C, e
Sgr B2+ M0.74+ G0.66	-	1.15±0.15	11 (2–8 keV)	96		

∗ Some numerical values in the columns, Name (l, b) and Area may have errors of $\lesssim 0^\circ.01$ and $\lesssim 10\,\%$, respectively, because these are read from the original figures in the References.

With multiple observations, flux variability is found (Y) or not(N).

† Instrument, A: ASCA, C: Chandra, B: BeppoSAX, S: Suzaku, N: NuSTAR, X: XMM-Newton.

‡ Reference, a: Murakami et al. (2000), b: Murakami et al. (2001b), c: Sidoli et al. (2001), d: Senda et al. (2002), e: Yusef-Zadeh et al. (2007), f: Koyama et al. (2007a), g: Nobukawa et al. (2008), h:Inui et al. (2009), i: Nobukawa et al. (2011), j: Zhang et al. (2015)

⋆ Unabsorbed flux, but reference (f) is absorbed flux.

|| 2005 observation.

∗∗ 2009 observation.

variability of the Fe I-Kα line in the giant MC Sgr B2 is shown in figures 6. The Fe I-Kα line flux of ASCA and Chandra in the observations of 1994 and 2000 was 1.4 times stronger than those of XMM-Newton and Suzaku observations of 2004 – 2005.

The fluorescent Fe I-Kα lines should be accompanied by the Compton scattered hard X-rays from the cloud. Indeed, the INTEGRAL satellite found a diffuse hard X-ray source, named IGR J17475−2822 at the position of the Sgr B2 cloud (Revnivtsev et al. 2004). With INTEGRAL of more than 40 Msec observations from 2003 to 2009, Terrier et al. (2010)

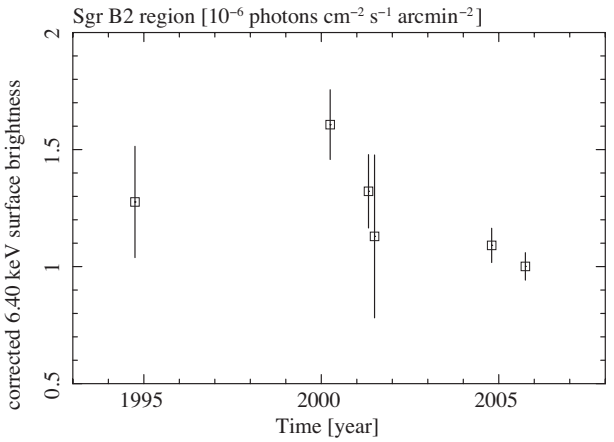

Fig. 6. The light curve of the Fe I-Kα line in the Sgr B2 cloud. The data points are ASCA observation in 1994, the Chandra and XMM observations in 2000 and 2001, the XMM observation in 2004 and the Suzaku observation in 2005 (From Inui et al. 2009).

found that the flux of IGR J17475−2822 decreased with the time scale of 8.2±1.7 years.

Nobukawa et al. (2011) made an additional Suzkau observation in 2009. They compared the two Sgr B2 spectra observed in 2005 and 2009. These spectra include all the essences of the XRN scenario: the rapid and correlated time variability of the Fe I-Kα line and the continuum fluxes, the large EW$_{6.4}$, and the deep K edge absorption. The X-ray flux of the Fe I-Kα line decreased in correlation with the hard-continuum flux by a factor of 0.4 – 0.5 in four years, which is almost equal to the light traveling time across the Sgr B2 cloud. The same flux decrease in 2005 – 2009 is also found from the other Fe I-Kα line clump in the Sgr B complex, M0.74−0.009.

Zhang et al. (2015) detected hard X-rays up to 20 keV with NuSTAR from the Sgr B region. The photon index is determined to be $\Gamma \sim 2$, similar to typical AGNs. They also reported the time variability of the Sgr B2 cloud using XMM-Newton; the Fe I-Kα flux showed continuous decease from 2001 to 2012 – 2013. This is a smooth extension of the decreasing trend in 2000 – 2009. NuSTAR shows a hint that the flux became constant after 2013 to 2014 at a level of 20 % of that in 2001.

Zhang et al. (2015) discovered a new Fe I-Kα cloud in the Sgr B complex, named G0.66−0.13. This source is time variable of increasing Fe I-Kα flux during 2001 – 2013. In 2013, the flux was brighter than the Sgr B2 cloud, but in 2014, it became below the detection limit. The 8 – 12 keV band flux of NuSATR in the non-thermal continuum emission dropped by 50 % in 2013 from that measured with XMM-Newton in 2012. Due to the faintness, however, no detailed spectral information is available for G0.66−0.13.

Another Fe I-Kα clump, named M0.51−0.10 is found at the position of the Sgr B1 cloud (Yusef-Zadeh et al. 2007 and figure 5). With Suzaku, Nobukawa et al. (2008) studied in detail, and found that EW$_{6.4}$ and $N_{\rm H}$ are $\sim$1.4 keV and $\sim 1.5 \times 10^{23}$ cm^{-2}, respectively. Therefore, M0.51−0.10 (Sgr B1) is likely another XRN in the Sgr B complex.

As is noted in section 4.1.3, the young SNR candidate G0.570−0.018 is discovered with Chandra, then confirmed with ASCA (Senda et al. 2002). Inui et al. (2009), however found a time variability of Fe I-Kα line from this source in the ASCA, Chandra, XMM-Newton and Suzaku observations. The Fe I-Kα line flux changed by factor of $\sim$0.5, but Fe XXV-Heα line was constant with time. Thus, G0.570−0.018 is an XRN, but the X-ray would be contaminated by the nearby SNR G0.570−0.001, which may emit Fe XXV-Heα and Fe XXVI-Lyα lines (section 4.1.3).

All the Fe I-Kα clumps (candidates of XRNe) near the Sgr B complex are listed in table 7. In this table, the EW$_{6.4}$ in Sgr B1+G0.57−0.018 (Yusef-Zadeh et al. 2007) is exceptionally small compared to those of other regions and authors. Since Yusef-Zadeh et al. (2007) used larger photon collecting areas than those of the other authors, the value of EW$_{6.4}$ would be affected by the local background of the GCXE with small EW$_{6.4}$, and hence gives the smaller EW$_{6.4}$ than the other authors of the smaller photon collecting areas. On the other hand, the Sgr B2+M0.7−0.09+G0.66−0.13 clouds (Yusef-Zadeh et al. 2007) have a large XRNe area, and hence observed EW$_{6.4}$ wolud be normal. From the Sgr B2 cloud, unusually large EW$_{6.4}$ of $\sim$2 – 3 keV are reported by Murakami et al. (2000); Murakami et al. (2001b); Sidoli et al. (2001). These would be due to the limited spectral resolution and statistics of ASCA and BeppoSAX compared to the other later observations with Suzaku, Chandra and XMM-Newton.

The X-ray spectra and time variability in the flux and morphology of the Fe I-Kα clumps in the Sgr B complex strongly support the XRN scenario. The Fe I-Kα line and associated power-law continuum are due to "an X-ray echo" , or X-ray fluorescence (Fe I-Kα) and Thomson scattering (power-law) of an external X-ray source. The required flux of the external X-ray source depends on the distance to the Fe I-Kα clump. Even in the minimum case that the external X-ray source is inside the Fe I-Kα clump of $\sim$1 pc size, the flux should be larger than 10^{37} erg s^{-1}. Furthermore, this high flux should be an averaged value in more than $\sim$1 year. Since no such Galactic X-ray source is found near the Sgr B complex, a unique candidate for the irradiating X-ray source is the SMBH, Sgr A*. One plausible scenario is that Sgr A* exhibited large flares with the luminosity of more than $\sim 10^{39}$ erg s^{-1}(averaged in $\gtrsim$1 year). The fluorescent / Thomson scattered X-rays by the Sgr B clouds have now arrived at the Earth, after traveling extra time between the direct pass from Sgr A* and the pass via the Sgr B clouds, which is a few hundred light-years. From all the observational results, the Sgr B Fe I-Kα clumps are regarded as the most se-

cure example of the XRN, hence may be called a prototype of the XRN.

Sunyaev et al. (1998); Odaka et al. (2011) proposed that the morphologies, spectra and the time variations of scattered and fluorescent X-rays are the useful diagnostics for the study of the XRN scenario. The detailed simulation is made by Odaka et al. (2011). In order to compare the observations to this simulation, very fine and complicated observational results are required, which is a subject of future study.

5.2.2 The Northeast Region from Sgr A*: Sgr A XRN Complex

The Fe I-Kα line clumps in the Sgr A complex located at the northeast of Sgr A* are firstly found with ASCA (Koyama et al. 1996). However, unlike the Sgr B complex, no detailed study was made due to its highly complex structure. With Chandra, Koyama et al. (2004) found Fe I-Kα complex in the MC at $(l,b) \sim (0.12, -0.12)$ (Tsuboi et al. 1997; Oka et al. 2001), and proposed these are XRNe candidates. Park et al. (2004) found at least three Fe I-Kα clumps (No1, 2 and 3 in table 9) with large EW$_{6.4}$ of ~ 1 keV from this region. Muno et al. (2007) listed up 2 Fe I-Kα sources named Feature 1 and Feature 2, the same sources as No1 and No2, respectively. They found that Feature 2 showed flux (4 – 10 keV) decline by 26 ± 7 % from the 2002 to 2004 – 2005 observations. Although, Feature 1 showed no flux change, this source showed a hint of a morphology change during this period similar to Feature 2

Lu et al. (2008) found two Fe I-Kα sources near the radio and X-ray filament F10 (table 12). These sources are named East and West, the same sources as No 1 and No 2, respectively. Although they suggested electron origin, the discovery of time variability by Muno et al. (2007) strongly supports an X-ray irradiation scenario.

Muno et al. (2008) listed small size ($\lesssim 0'.1$) filament-like sources near the GC (section 6.1). Some of them exhibited large EW$_{6.4}$. Therefore these would be bright fragments of normal XRNe in the XRN complex region. This unusual morphology, on the other hand, leads to suspect different origins than XRN. One plausible idea is that the filament-like Fe I-Kα line source is due to the bombardment of LECRp on low-temperature gas confined by strong magnetic fields.

Ponti et al. (2010) made the Fe I-Kα line image using $\sim$1.2 Msec data of XMM-Newton in the time span of $\sim$8 years. They divide the image into 4 regions, Bridge, G0.11$-$0.11, MC1 and MC2. The region of Bridge is further divided into 7 sub-regions (Bridge 1 – 7). The fluxes of the Fe I-Kα line from these regions show different time variation with each other. The Fe I-Kα line flux in MC1, MC2, Bridge 5 – 7 are constant with time, those in Bridge 1 – 4 increase with time, and the other Fe I-Kα clump G0.11$-$0.11 shows decrease with time. An apparent superluminal motion of a light front is found in Bridge 1.

Capelli et al. (2012), on the other hand, divided the XMM-Newton image of the Fe I-Kα line complex into 9 regions, and found flux increasing clumps, B2, C and D, and decreasing clumps, B1 and F. The fluxes in the clumps A, E, DS1 and DS2 are constant in time.

Using the Chandra data, Clavel et al. (2013) examined the details of the time variability and spatial structure of the Fe I-Kα clumps in the regions of Ponti et al. (2010). They divided Bridge 1 into Br1a – Br1e with each size of $26'' \times 61''$, and selected the same small bright spot Br2f from Bridge 2. They found short flares of the Fe I-Kα line in the 10 years light curves from Br1a – Br2f. The peak position moved in the order of the look-back time in the light-curve of Br1a – Br2f, during 2005 – 2012. This confirmed the superluminal motion suggested by Ponti et al. (2010). Since the flare peak is $\sim$10 time brighter than that in quiescent, they proposed that the past flare of Sgr A* is not single but composed of multiple flares with the peak luminosity of $\sim 10^{39}$ erg s^{-1}. They also divided the clump MC1 into MC1a – f with each size of $26'' \times 61''$, and found increases of the Fe I-Kα flux in MC1c – MC1f, and decreases in MC1a and MC1b. They further selected 13 small bright spots in the 4 – 8 keV band from Bridges 1 and 2, G0.11-0.11, MC1 and MC2, with a $15''$ square, and found time variability in the light curves of the 4 – 8 keV band. The fluxes of the spots, Br1p, Br1m, Br2o, G011s and MC1j, are increasing. From the former 3 spots, short flares of time scale of a few years were observed. The fluxes of the spots, G0.11u, G0.11r, MC1k and MC2n, are decreasing during the time span of 10 years. The fluxes of the other four spots were constant with time.

Nobukawa et al. (2010) made a high quality spectrum with Suzaku from the brightest Kα region at the northeast of Sgr A*. They fitted the spectrum with a combined model, two CIE plasmas and a power-law continuum with many Gaussian lines. The CIE plasmas represented the background spectrum (GCXE) in these clumps. They discovered Kα lines from neutral Ar, Ca, chrome (Cr) and manganese (Mn), in addition to the already known K-shell lines from the neutral Fe and Ni. The best-fit parameters of the Gaussian lines are given in table 8. They determined the Fe abundance in the GCXE around these XRNe to be $\sim$1.1 – 1.2 solar. Assuming the scattering angle of $\theta = 90°$, the EW$_{6.4}$ of 1150 ± 90 eV in these XRNe is converted to the Fe abundance of 1.2 ± 0.1 solar[3]. Thus, the Fe abundance in the GC region estimated with Fe I-Kα line in the XRNe and Fe XXV-Heα line in the GCXE, are almost the same of $\sim$1.1 – 1.2 solar, consistent with those of Koyama et al. (2007c); Uchiyama et al. (2013); Muno et al. (2004a)[4]. The EW of the Kα lines of Ar I, Ca I, Cr I and Ni I are roughly consistent with the solar abundances (table 8).

[3] The Fe abundance in the original paper by Nobukawa et al. 2010 is 1.6 solar, but they used different abundance table.

[4] This Fe abundance is corrected to that in the same model as the other authors, which includes a power-law component.

Table 8. K-shell lines from heavy elements from the Radio arc region (after Nobukawa et al. 2010).

Line	Energy (keV)	Intensity (†)	EW (eV)
Ar I-Kα	2.94±0.02	170^{+60}_{-40}	140±40
Ca I- Kα	3.69±0.02	54^{+14}_{-9}	83±13
Cr I- Kα	5.41±0.04	9.5±2.5	24±7
Mn I- Kα	5.94±0.03	7.4±2.2	22±7
Fe I-Kα	6.404±0.002	340±10	1150±90
Fe I-Kβ	7.06(fixed)	40±3	160±20
Ni I-Kα	7.48±0.02	18±3	83±13

† In unit of 10^{-6} photons s^{-1} cm^{-2}.

NuSTAR detected non-thermal continuum X-rays (Mori et al. 2015) spatially correlated with the Fe I-Kα fluorescence line from the two Fe I-Kα clumps, MC1 and Bridge. They made a Monte-Carlo simulation with the XRN model for the broad-band X-ray spectrum. Then, they determined that the intrinsic column density is $\sim 10^{23}$ cm^{-2}, the primary X-ray spectrum of a power-law has photon index (Γ) of ~ 2, and the flare luminosity of Sgr A* is $\gtrsim 10^{38}$ erg s^{-1}.

Lu et al. (2008) found a faint source at the east of the southernmost extension of the Radio Arc (Johnson et al. 2009), and named G0.017−0.044. Since G0.017−0.044 has a reasonably large EW$_{6.4}$ of ∼0.62 keV, this may be an XRN, one of the nearest (in projection) XRN from Sgr A*. However, no detailed spectral information to judge the reliable origin is available.

G0.174−0.233 is discovered with Suzaku near the Radio Arc (Fukuoka et al. 2009). The spectrum exhibits bright Fe I-Kα, Ca I-Kα and a hint of Ar I-Kα lines. The EW$_{6.4}$ is ∼0.95 keV, typical to XRN. The detection of the Ca I-Kα and Ar I-Kα lines from G0.174−0.233 (Fukuoka et al. 2009) is the second case after the Sgr A XRN (Nobukawa et al. 2010).

The physical parameters of the XRNe in the Sgr A complex are summarized in table 9. Since the Sgr A region is very crowded with many XRNe, some XNRe overlap with those reported by other authors. The most important parameter, EW$_{6.4}$ should be time constant, regardless the time variable flare fluxes of Sgr A*, and free from the observed ambiguity of the $N_{\rm H}$ values. If the iron abundances and scattering angle θ are the same among the XRNe, the EW$_{6.4}$ should be the same in all the XRNe (equation 4). Nevertheless, the reported EW$_{6.4}$ shows apparent and systematic variations among the authors and instruments, and in each XRNe. For example, No3 (Park et al. 2004), G0.11−0.11 (Ponti et al. 2010) and F (Capelli et al. 2012) are the same XRN in position with a similar collecting area. However, the observed EW$_{6.4}$ are largely different of ∼1.3, ∼1.0 and ∼1.7 keV, respectively.

The value of the EW$_{6.4}$ depend on the the continuum flux of the XRNe, which is sensitive to the subtraction of local GCXE. The flux of local GCXE is position dependent, because the SH is very small of $\sim 0^\circ.25$. Since the Sgr A complex is crowded with many XRNe, the background (GCXE) position is very limited. This situation causes the non-negligible EW$_{6.4}$ difference among the authors and XRNe, which may be called the systematic errors. An example of this systematic error is found in the EW$_{6.4}$ and $N_{\rm H}$ differences between Capelli et al. (2012) and Ponti et al. (2010). The total areas of the total XRNe by Ponti et al. (2010) and Capelli et al. (2012) are almost the same. However, the mean EW$_{6.4}$ and $N_{\rm H}$ are, respectively ∼0.78 keV and $\sim 6.5 \times 10^{22}$ in Ponti et al. (2010), and ∼1.2 keV and $\sim 12 \times 10^{22}$ in Capelli et al. (2012). The background of Ponti et al. (2010) is taken from the source free regions in the GC-west, where the GCXE is systematically lower than the GC-east, near the Sgr A XRNe complex (see section 9.3). Therefore the continuum emission of the XRNe is under-subtraction, giving systematically smaller EW$_{6.4}$ and $N_{\rm H}$ than those of Capelli et al. 2012 and any other authors.

Accordingly, the values of the physical parameters in table 9 should be carefully treated. Taking account of the possible errors of the EW$_{6.4}$ in table 9, it is still worth to note that the EW$_{6.4}$ in all the XRNe are roughly consistent with ∼1 keV.

5.2.3 Sgr C, D, and E

The Sgr C complex is a unique star-forming region in the west of the CMZ, which is located at the mirror point of the Sgr B complex with respect to Sgr A*. This complex is composed of high-mass YSOs, H II regions and radio non-thermal filaments (NTF) (Kendrew et al. 2013 and references therein). ASCA found a diffuse hard X-ray emission from the Sgr C complex (Murakami et al. 2001a). The X-ray spectrum is characterized by a large EW$_{6.4}$ of ~ 1 keV and a large absorption column of $\sim 10^{23}$ cm^{-2}, suggesting that the X-rays are due to fluorescence and scattering of external X-rays. No adequately bright source in the immediate vicinity of the Sgr C complex to account for the fluorescence flux is found. Thus, with the same reason of the Sgr B complex, the irradiating X-ray source would be a past bright flare of Sgr A*; the Sgr C complex is the second XRN complex discovered after the Sgr B complex.

With Chandra, Yusef-Zadeh et al. (2007) found 5 X-ray spots from the Sgr C complex in the 2 – 6 keV band image. Two of them, G359.45−0.07 and G359.42−0.12, are diffuse sources with the size of $\lesssim 4'$. They made an X-ray spectrum from the region including these two diffuse sources. The mean EW$_{6.4}$ is ∼470 eV.

Suzaku found four diffuse clumps near the Sgr C region (Nakajima et al. 2009), named M359.47−0.15, M359.43−0.07, M359.43−0.12 and M359.38−0.00. Two of them, M359.47−0.15 and M359.43−0.07 are prominent in the Fe I-Kα line image. The EW$_{6.4}$ values are very large of ∼2.0 – 2.2 keV, nearly 2 times larger than those of the normal XRNe in

Table 9. The 6.4 keV clumps near the Radio arc region.

Name $(l,\ b)^*$	$N_{\rm H}$	$EW_{6.4}$	$F_{\rm x}$ (2–10 keV)	Var#	Area	Instrument†
	(10^{22}cm^{-2})	(keV)	(10^{-12}erg s^{-1}cm^{-2})	-	(Arcmin^2)	Reference‡
No1 (0.023, −0.053)	$32.9^{+4.0}_{-4.2}$	1.19 ± 0.10	1.7	-	0.5	C, a
No2 (0.045, −0.081)	$36.8^{+9.6}_{-13.8}$	$1.03^{+0.37}_{-0.23}$	3.1	-	1.5	
No3 (0.121, −0.137)	$15.8^{+4.1}_{-2.6}$	1.29 ± 0.10	2.0	-	1.3	
All (0.08, −0.08)	-	0.67 ± 0.05	56	-	123	C, b
All (0.08, −0.08)	12.0±1.1	1.15±0.09	-	-	45	S, h
Feature 1 (0.023, −0.053)	36^{+5}_{-3}	$1.00^{+0.24}_{-0.09}$	$0.52^{+0.02}_{-0.03}$ (4–8 keV)$^{\|\|}$	N	0.9	C, c
Feature 1 (0.023, −0.053)	34^{+5}_{-3}	$1.01^{+0.19}_{-0.09}$	$0.48^{+0.02}_{-0.03}$ (4–8 keV)§	N	0.9	
Feature 2 (0.045, −0.081)	40^{+20}_{-6}	$0.93^{+0.16}_{-0.16}$	$0.77^{\pm}0.03$ (4–8 keV)$^{\|\|}$	Y	2	
Feature 2 (0.045, −0.081)	75^{+26}_{-18}	$0.69^{+0.22}_{-0.22}$	$0.55^{\pm}0.03$ (4–8 keV)§	Y	2	
East clump (0.023, −0.053)	14 ± 0.2	$0.75^{+0.08}_{-0.07}$	1.1	-	0.9	C, d
West clump(0.045, −0.081)	$23^{+0.6}_{-0.7}$	$1.07^{+0.16}_{-0.13}$	1.1	-	2	
G0.014−0.054	-	$0.87^{+0.45}_{-0.38}$	0.08 (2–8 keV)	-	0.072	C, e
G0.021−0.051	-	$1.0^{+0.57}_{-0.47}$	0.07 (2–8 keV)	-	0.052	
G0.039−0.077	-	$0.66^{+0.35}_{-0.27}$	0.11 (2–8 keV)	-	0.093	
G0.062+0.010	-	$1.58^{+1.38}_{-1.35}$	0.06 (2–8keV)	-	0.33	
G0.097−0.131	-	$1.19^{+0.42}_{-0.35}$	0.48 (2–8 keV)	-	1.2	
G0.017−0.044	-	$0.62^{+0.58}_{-0.34}$	0.04	-	0.01	C, f
G0.174−0.233	$7.5^{+2.0}_{-1.7}$	$0.95^{+0.18}_{-0.19}$	0.48	-	3	S, g
Bridge** (0.09,−0.08)	4 ± 3	$0.75^{+0.05}_{-0.03}\star$	-	Y/N	7.4	X, i; C, k
G0.11−0.11	7 ± 4	$0.96 \pm 0.06^*$	-	Y	14	
MC1 (0.020, −0.052)	10^{+1}_{-2}	$0.68^{+0.07}_{-0.02}\star$	-	N	2.1	
MC2 (0.035, −0.096)	5^{+5}_{-4}	$0.72^{+0.12}_{-0.07}\star$	-	N	1.8	
A (0.022, −0.052)	$18.4^{+1.5}_{-2.7}$	0.9±0.1	-	N	2.2	X, j
B1 (0.028, −0.077)	$10.2^{+2.3}_{-2.0}$	0.9±0.1	-	Y	2.6	
B2 (0.055, −0.083)	$12.3^{+3.0}_{-2.7}$	$1.5^{+0.3}_{-0.2}$	-	Y	1.9	
C (0.048, −0.053)	$5.8^{+2.3}_{-1.9}$	$1.0^{+0.2}_{-0.1}$	-	Y	2.0	
D (0.072, −0.072)	$13.2^{+5.0}_{-4.7}$-	$1.3^{+0.4}_{-0.3}$	-	Y	1.8	
E (0.090, −0.087)	$9.6^{+1.7}_{-1.4}$	1.4±0.2	-	N	2.9	
F (0.125, −0.115)	$9.2^{+2.7}_{-2.3}$	1.7±0.2	-	Y	15	
DS1 (0.065, −0.020)	$15.5^{+3.9}_{-3.3}$	0.9±0.2	-	N	3.7	
DS2 (0.025, −0.012)	14.5±2.3	0.9±0.1	-	N	6.5	

∗ Same as table 7, but for the XRNe in the Sgr A complex.

With multiple observations, flux variability is found (Y) or not(N).

† Instrument, C: Chandra, S: Suzaku, X: XMM-Newton.

‡ Reference, a: Park et al. (2004), b: Yusef-Zadeh et al. (2007), c: Muno et al. (2007), d:Lu et al. (2008), e: Muno et al. (2008), f:Johnson et al. (2009), g: Fukuoka et al. (2009), h: Nobukawa et al. (2010), i: Ponti et al. (2010), j: Capelli et al. (2012), k: Clavel et al. (2013).

|| Observed in 2002.

§ Observed in 2004 – 2005.

∗∗ This region is separated to subgroups, Bridge 1 – 7.

⋆ Errors are estimated from the flux errors of the Fe I-Kα line.

the Sgr B and Sgr A complexes. This is puzzling, but possibly some systematic errors are involved. The absorptions ($N_{\rm H}$) are $\sim 10^{23}$ cm^{-2}, consistent with that the sources are in the MCs of the Sgr C complex.

Ryu et al. (2013) re-analyzed the same region, and found 3 Fe I-Kα diffuse sources, named C1, C2 and C3, where the positions of C1 and C2 coincide to those of M359.47−0.15 and M359.43−0.07, respectively. These sources have reasonable EW$_{6.4}$ of $\sim$1.1 – 1.6 keV. The Fe I-Kα line of C1 increased by 8 % (2.9σ confidence) from the 2006 to the 2010 observations.

Table 10. The 6.4 keV clumps near the Sgr C complex.

Name$(l, b)^*$	$N_{\rm H}$ (10^{22}cm^{-2})	$EW_{6.4}$ (keV)	$F_{\rm x}$ (3–10 keV)* (10^{-12} erg s^{-1}cm^{-2})	Area (arcmin^2)	Instrument† Reference‡
Sgr C (359.42, −0.04)	$12.6^{+3.5}_{-3.3}$	$0.8^{+0.4}_{-0.5}$	6 (4–10 keV)	23	A, a
G359.45+G359.42	-	0.47±0.10	12 (2–8 keV)	77	C, b
M359.43−0.076	$9.2^{+4.9}_{-4.4}$	$2.2^{+0.3}_{-0.4}$	0.27	7.1	S, c
M359.47−0.15	$8.2^{+3.6}_{-1.7}$	$2.0^{+0.2}_{-0.2}$	0.41	6.9	
C1 (359.43, −0.076)	$11.6^{+0.6}_{-0.8}$	1.1–1.5	-	13	S, d
C2 (359.47, −0.15)	$17.9^{+1.9}_{-1.6}$	1.1–1.6	-	13	
C3 (359.58, −0.13)	$13.7^{+0.7}_{-0.8}$	0.7–1.3	-	31	

$*$ Same as table 7, but for the XRNe in the Sgr C complex.

$\star$ Unabsorbed flux, but reference (c) is absorbed flux. Two separate observations of C1 made in 2006 and 2010 show a time variability.

† Instruments. A:ASCA, C:Chandra, S: Suzaku

‡ Reference, a: Murakami et al. (2001a), b: Yusef-Zadeh et al. (2007), c: Nakajima et al. (2009), d: Ryu et al. (2013).

The time variability of C1, and the large EW$_{6.4}$ of 1 – 1.6 keV of C1, C2 and C3 favors the X-ray irradiation scenario (XRNe).

The summary of the Fe I-Kα sources in the Sgr C complex is given in table 10. The small EW$_{6.4}$ value of $\sim$ 470 eV by Yusef-Zadeh et al. (2007) is marginal whether the origin is LECR electron or X-ray irradiation (XRN). However, the small EW$_{6.4}$ value would be due to the larger correcting area of 77 arcmin^2 than Nakajima et al. (2009) and Ryu et al. (2013), and hence the spectrum would be contaminated by the nearby GCXE (see section 5.2.2). In fact, Nakajima et al. (2009) observed the EW$_{6.4}$ value from nearly the same area of Yusef-Zadeh et al. (2007) with Suzaku and found that the EW$_{6.4}$ is 460 eV.

The Suzaku extensive observations near the edge of the GCXE revealed strong Fe I-Kα lines from the Sgr D and E complexes (see figure 5). Although no detailed follow-up analysis of these complexes have been made, the similarity in spectra and morphologies to those of the Sgr B, A and C complexes suggests that the Sgr D and E complexes also contain XRNe.

5.3 Fe I-Kα Clumps Other than XRNe

This section reviews the other Fe I-Kα clumps than those in section 5.2. The origins may not be an X-ray irradiation from Sgr A*, but the irradiation sources would be either local nearby bright X-ray stars, LECRe or LECRp.

5.3.1 Arches Cluster

In addition to the thermal hot plasma (section 4.1.6) in the central region, Yusef-Zadeh et al. (2002b); Law & Yusef-Zadeh (2004) found extended emission, named A3 at the southeast from the core of the Arches cluster with Chanda. The source A3 has a power-law spectrum with possibly Fe I-Kα lines. However no detail of the spectrum was reported. Then after, Yusef-Zadeh et al. (2007) reported the Fe I-Kα line emission with EW$_{6.4}$ of $\sim$0.8 keV. A long exposure Chandra observation by Wang et al. (2006b) found that the thermal plasma mainly comes from the center region of the cluster, but a strong Fe I-Kα line with power-law continuum emission is coming from the southeast region of the star cluster, named SE extension. Since the EW$_{6.4}$ is $\sim$1.4 keV, most likely origin is bombardment of molecular gas by X-ray photons or low energy protons.

Tsujimoto et al. (2007) made the Suzaku spectrum from the whole region of the Arches cluster, because Suzaku had no good spatial resolution. The spectrum is fitted with a model of a CIE plasma plus power-law continuum with two Gaussian lines at 6.4 keV (Fe I-Kα) and 7.05 keV (Fe I-Kβ). Then, the power-law spectrum has a photon index of $\sim$0.7, but no pronounced iron K-edge feature at 7.1 keV is found. Since the narrow band image of 7.5 – 10.0 keV shows a similar distribution to that of the Fe I-Kα line flux, the Fe I-Kα and Fe I-Kβ lines are associated to the power-law component with the EW$_{6.4}$ of $\sim$1.42 keV. They also examined the Chandra spectra, and found that the power-law index and EW$_{6.4}$ to be $\sim$1.2 and $\sim$1.25 keV, respectively.

XMM-Newton found a big loop-like annular structure in the Fe I-Kα band of $\sim 3'$ diameter and $\sim 1'$ width around the star cluster, named Loop (Sakano et al. 2006). They made an X-ray spectrum from the brightest part of Loop at the southeast of the cluster center, and fitted with a model of a power-law plus a Gaussian line. The best-fit absorption column and photon index are $(7.2 \pm 1.4) \times 10^{22}$ cm^{-2} and 1.4 ± 0.6, respectively. The EW$_{6.4}$ is 1.0 ± 0.25 keV. Capelli et al. (2011b) found three Fe I-Kα clumps, N, S and SN. These comprise a part of the loop-like structure of Sakano et al. (2006). The EW$_{6.4}$ are all within the range of 0.9 – 1.1 keV. They interpreted that N, S and SN are explained by the MC bombardment of LECRs from the Arches cluster stars. Tatischeff et al. (2012) found a strong Fe I-Kα line from nearly the same regions of N and S,

Table 11. The 6.4 keV clumps near Arches Star clusters.

Name $(l, b)^*$	$N_{\rm H}$	$EW_{6.4}$	$F_{\rm x}$ (2–8 keV)	Area	Instrument†
	(10^{22}cm^{-2})	(keV)	(10^{-12}erg s^{-1}cm^{-2})	(Arcmin^2)	Reference‡
SE extension (0.1, 0.02)	$6.2^{+2.7}_{-5.6}$	$1.4^{+0.9}_{-0.5}$	0.54	0.5	C, a
Loop (0.1, 0.05)	7.2 ± 1.4	1.00 ± 0.25	-	3.1	X, b
Arches (0.1, 0.03)	-	0.81±0.2	1.2	1.6	C, c
Arches (0.1, 0.03)	14±5	∼1.25–1.42	1.1 (3–10 keV)	6.2	C, S, d
N (0.13, 0.02)	9.5±1.5	1.0±0.4	-	0.5	X, e
S (0.12, 0.01)	10.1±0.7	0.9±0.2	-	0.5	
SN (0.10, 0.01)	$8.5^{+4.0}_{-3.4}$	1.1±0.4	-	0.9	
DX (0.10, 0.05)	6(fixed)	$2.6^{+2.1}_{-1.1}$	-	0.8	
Cloud region (0.12, 0.02)	$11.3^{+1.9}_{-1.3}$	1.2±0.2	-	1.1	X, f
Cloud region (0.12, 0.02)	9.5(fixed)	$1.1^{+0.7}_{-0.5}$	1.5 (3–20 keV)	1.1	N, g
Cloud region (0.12, 0.02)	6.0±0.3	0.9±0.1	-	1.1	X, h

∗ Same as table 7, but for the Fe I-Kα clumps in the Arches cluster.

† Instruments. C:Chandra, N: NuSATR, X: XMM-Newton

‡ Reference, a: Wang et al. (2006b), b: Sakano et al. (2006), c: Yusef-Zadeh et al. (2007), d: Tsujimoto et al. (2007), e: Capelli et al. (2011b), f: Tatischeff et al. (2012), g: Krivonos (2014), h:Clavel et al. (2014).

with the $EW_{6.4}$ of ∼1.2 keV. Since no time variability of the Fe I-Kα line during 2000-2010 is found, they claimed that the origin would be LECRp. Possible supersonic collision between the stellar wind from star clusters and MCs would make strong shock and hence would become efficient particle acceleration, which makes enough LECR to produce the Fe I-Kα line and power-law flux. Although it is not clear whether the origin is X-rays or protons, the candidate source would be related to high-mass stars in the Arches cluster.

Krivonos (2014) detected diffuse X-rays up to ∼30 keV with NuSTAR. The emitting region is an ellipse of northwest-southeast major axis, nearly the same regions of N and S of Capelli et al. (2011b). They determined the $EW_{6.4}$ to be ∼1.1 keV. The wide band X-ray spectrum is in broad agreement with the LECRp origin. Using the XMM-Newton data from 2000 to 2013, Clavel et al. (2014) examined a long-term time variability of the power-law emission in the same eclipse of Krivonos (2014). The $EW_{6.4}$ is ∼0.9 keV. They found a flux drop by 30 % in 2012, and hence constant flux hypothesis is rejected with more than 4 σ confidence. From this time variability, they interpreted that the power-law emission is due to the reflection of an X-ray transient source in the Arches cluster.

Most of the authors suggested that the irradiation source for the Fe I-Kα emission is active stars in the core of the Arches cluster, because of extreme activity of the embedded stars than the other star clusters. If the irradiation sources are the cluster stars in the core, with the mean distance of ∼1 pc from the Fe I-Kα diffuse sources, the X-ray luminosity should be >100 times brighter than any of the observed results of $\sim 4 \times 10^{33}$ erg s^{-1} (Capelli et al. 2011a). Therefore, with the same reason as the other XRN candidates (section 5.1), it is also possible that the Fe I-Kα emission from the Arches cluster is due to the past flare of Sgr A*. The luminosity and epoch of the flare are not largely different from those estimated from the XRNe in the Sgr A complex, because their positions, Fe I-Kα fluxes and luminosity are not largely different from those of the Sgr A XRNe (table 9). Thus, the true origin of Fe I-Kα line in this star cluster is a puzzle, whether the irradiation source is cluster stars or Sgr A*, whether it is X-ray or LECRp.

In the XMM-Newton image, Capelli et al. (2011b) found the other Fe I-Kα clump, DX at about 16 pc west of the cluster center. The $EW_{6.4}$ of DX is very large of ∼2.6 keV. A short timescale variability is found from DX. These are unusual compared to the other Fe I-Kα clumps in the Arches cluster. Together with the large distance from the cluster, DX would be unrelated object to the Arches cluster.

The summary of the Fe I-Kα line emission from the Arches cluster are listed in table 11. All the $EW_{6.4}$ are around ∼1 keV. The clump DX has an exceptionally large $EW_{6.4}$ of ∼2.6 keV, although the error is large. As is noted, DX would be unrelated object to the Arches cluster.

5.3.2 Fe I-Kα Clump Near the Great Annihilator

Suzaku found two diffuse X-ray sources with strong K-shell lines near 1E 1740.7−2942, the Great Annihilator by Nakashima et al. (2010). One is an SNR candidate G359.12−0.05 with a strong S XV-Heα line (section 4.2.6). The other source, M359.23−0.04 has a prominent Fe I-Kα line and locates at the northeast of 1E 1740.7−2942. The $EW_{6.4}$ is as large as ∼ 1.2 keV, and is associated with a MC in the radio CS

(J=1−0) map (Tsuboi et al. 1999). The $N_{\rm H}$ is $\sim 3\times10^{23}$ cm^{-2}. Thus, the Fe I-Kα line from M359.23−0.04 is likely due to X-ray fluorescence irradiated by an external X-ray source. One possible candidate of the external source is 1E 1740.7−2942 itself. Assuming the photon index of 1.4, Nakashima et al. (2010) estimated that the required luminosity of 1E 1740.7−294 is $\sim 4-5\times10^{36}$ erg s^{-1}. This is consistent with the observed 1E 1740.7−2942 luminosity of 2.6×10^{36} erg s^{-1}, if possible systematic errors and time variability are taken into account. The combination of M359.23−0.04 and 1E 1740.7−2942 is a rare case of the association of diffuse Fe I-Kα line and bright binary X-ray source.

5.3.3 G0.162−0.217

From the Radio Arc region, a small spot of the Fe I-Kα line is found at $(l, b) = (0.^\circ162,\ -0.^\circ217)$ with Suzaku, named G0.162−0.217 (Fukuoka et al. 2009). This source is located adjacent to the south end of the Radio Arc (LaRosa et al. 2000; Yusef-Zadeh et al. 2004). The Radio Arc is a site of relativistic electrons, which may include LECRe along the magnetic field line of the Radio Arc. Thus, G0.162−0.217 would be made by the LECRe. The observed EW$_{6.4}$ is ~ 0.2 keV, consistent with the LECRe bombarding scenario. This type of the faint Fe I-Kα line emitter would be more numerous in the GCXE (section 6), and may contribute significant fraction of Fe I-Kα flux in the GCXE (section 9.3). However limited statistics of the current instruments does not allow further search of these potential LECRe sources of the Fe I-Kα lines.

6 Small Size X-ray Sources or Non-Thermal X-Ray Filaments

This section reviews small scale diffuse plasmas discovered mainly with Chandra in the central region (section 6.1) and the outer region (section 6.2) of the GCXE. The shapes of the diffuse plasmas are mostly either filamentary or cometary with non-thermal X-ray spectra. In this section, these sources are called the X-ray filament. The summed luminosity (2 – 10 keV) of the X-ray filaments is $\sim 5\times10^{34}$ erg s^{-1}, only $\sim$4 % of the 2 – 10 keV band luminosity of the GCXE ($\sim 1.2\times10^{36}$ erg s^{-1}).

6.1 The Central Region of the GCXE

Muno et al. (2008); Lu et al. (2008) made the Chandra map in the close vicinity of Sgr A*, the $\sim 10' \times 10'$ region (within $\sim$20 pc from Sgr A*). They found many small scale diffuse sources, most of them have a filamentary or cometary shape (see figure 7). Table 12 is the summary of the X-ray filaments within $\sim$20 pc from Sgr A*, where strong Fe-Kα line filaments in Sgr A East and near the Sgr A complex and the Arches cluster, are excluded, because these are separately discussed in sections 4 and 5. All the diffuse sources listed in upper rows of table 12, the positions (source name), sizes and luminosity are taken from Muno et al. (2008), while those in lower rows are from Lu et al. (2008).

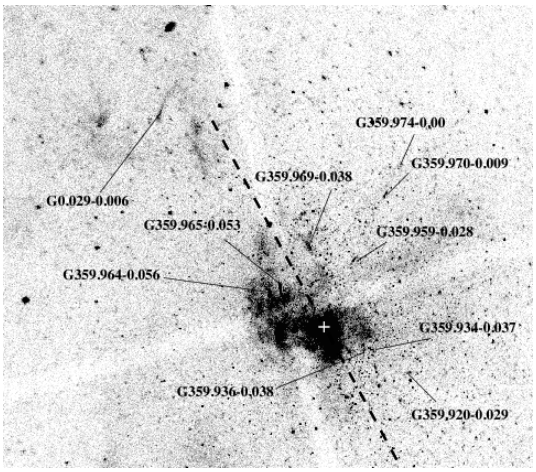

Fig. 7. X-ray filaments near Sgr A* in the central region of $6'.5 \times 6'.5$. The dashed line indicates the Galactic plane, and the plus sign denotes the position of Sgr A*. The brightest diffuse emission around Sgr A* is central star cluster, and the extended emission at the northeast of Sgr A*is the Sgr A East SNR (From Lu et al. 2008).

Diffuse sources have been also found or studied by many other authors. Since the typical morphology is filamentary or cometary with the length and width of $\sim 20''$ and $\sim 4''$ (the mean values of Muno et al. 2008; Lu et al. 2008), the cited positions may have typical uncertainly of a few $10''$. Therefore, if the source positions are within $\lesssim 20''$ from Muno et al. (2008) or Lu et al. (2008), these sources are regarded as the same objects of Muno et al. (2008) or Lu et al. (2008), and the authors names are listed in the column of Reference.

Most of the sources have power-law (non-thermal) spectra with the photon index of $\Gamma \sim 1-2$. However, only small fractions of the X-ray filaments are associated to the radio NTF. Four X-ray filaments, 359.945−0.044, G359.942-0.045, G359.944−0.052 and G359.950−0.043, are located very close to Sgr A* in the Sgr A West Cavity or on the Mini Spiral, and hence possibly associated to the Central Star Cluster (CSC), or related to the Sgr A* activity. Other four X-ray filaments, G359.956−0.052, G359.962−0.062, G359.964−0.053 and G359.965−0.056 are in the Sgr A East SNR. Since the EW$_{\rm Fe-K}$ of these X-ray filaments are less than $\sim$70 eV (Muno et al. 2008), these are not parts of the hot plasma of Sgr A East, but are more likely non-thermal filaments due to accelerated particles in the SNR Sgr A East.

The X-ray filament G359.945−0.044 (or G359.95−0.04 in Wang et al. 2006a, Lu et al. 2008 and Johnson et al. 2009) is one of the brightest filament separated only $0'.1$ from Sgr A*. It has a bright head and faint tail structure. The spectrum shows softening from the head to tail of photon index Γ from $\sim$1.3

Table 12. Non-thermal X-ray filament within the 17 arcmin Region.*

Name (l, b)	Size (arcsec^2)	EW_{Fe} (eV)	L_X (2−8 keV) (10^{32} erg s^{-1})	Comment	Reference‡
G359.945−0.044	22	≤60	66	in the Cavity, PWN ?	a, b, c, d, n
G359.942−0.045	28	≤220	16	in the Cavity	a, c
G359.944−0.052	20	≤470	2	Jet, in the Spiral	a, c, j
G359.950−0.043	55	≤140	4	in the Spiral	a
G359.933−0.039	15	-	-	F1	a, b, c
G359.956−0.052	10	-	1	in Sgr A East	a
G359.933−0.037	13	≤170	3		a, b
G359.941−0.029	17	≤180	2	F2 Stellar Wind ?	a, c
G359.925−0.051	19	≤2060	3		a
G359.964−0.053	76	≤70	17	in Sgr A East, PWN ?, F3	a, b, c, e
G359.965−0.056	29	-	3	in Sgr A East, F4	a, b
G359.921−0.052	12	-	-		a
G359.962−0.062	26	-	2	in Sgr A East	a
G359.959−0.027	34	≤75	6	knot-1, F5	a, b, c, f
G359.971−0.038	148	≤130	10	PWN ?, F6	a, b, c
G359.969−0.033	17	-	-	PWN ?	a
G359.921−0.030	30	≤1300	3	F7	a, b
G359.915−0.061	22	-	-		a
G359.983−0.040	-	-	-		a
G359.904−0.047	32	-	1		a
G359.977−0.076	26	-	-		a
G359.970−0.008	30	≤110	6	knot-2 PWN ?, F8	a, b, c, f, m
G359.899−0.065	30	-	3		a
G359.897−0.023	42	-	2		a
G359.889−0.081	432	≤30	70	Radio, Sgr A-E, PWN ?	a, b, c, g, h, l, n, o
G0.008−0.015	51	-	-		a, c
G0.032−0.056	429	≤110	10		a, b, c
G0.029−0.080	838	-	-		a
G0.116−0.111	2257	-	-		a
G0.029−0.06	6×47	-	11	Radio, PWN?, F10	b
G359.974−0.00	4×7	-	4	knot-3, F9	b, f
G359.983−0.046	-	-	31	Canonball, PWN ?	b f
G359.90−0.06	3×6	-	108	Radio, Sgr A-F	b, o
Total luminosity (2–10 keV)			3.8×10^{34} erg s^{-1}		

* Sources and parameters in upper rows are taken from Muno et al. (2008) in the order of angular distance from Sgr A*, while those of rower rows are from Lu et al. (2008). The overlapping sources from both Muno et al. (2008) and Lu et al. (2008) are combined in the upper rows. The sources observed by other authors with the separation angle of $\lesssim 0.3'$ are treated as the same objects.

‡ Reference, a: Muno et al. (2008), b: Lu et al. (2008), c: Johnson et al. (2009), d: Wang et al. (2006a), e: Baganoff et al. (2003), f: Koyama et al. (2004), g: Sakano et al. (2003), h: Lu et al. (2003), i: Park et al. (2005), j: Li et al. (2013), k: Nynka et al. (2013), l: Nynka et al. (2014), m: Nynka et al. (2015), n: Mori et al. (2015), o: Yusef-Zadeh et al. (2005).

to ∼3.1 (Wang et al. 2006a). The total X-ray luminosity is $\sim 10^{34}$ erg s^{-1}, with an averaged photon index of ∼1.7 – 1.9 (Muno et al. 2008; Lu et al. 2008; Johnson et al. 2009). These values are consistent with a PWN. However, no X-ray pulsar is found from the head. Thus, an alternative scenario is a ram pressured magnetic tube, which traps TeV electrons accelerated by Sgr A* (e.g. Wang et al. 2006a). Hard X-rays above 10 keV are detected with NuSTAR from this source (Mori et al. 2015). The 20 – 40 keV luminosity is $\sim 7 \times 10^{33}$ erg s^{-1}.

Hard X-rays above 10 keV are also detected with NuSTAR

Table 13. Non-thermal X-ray filament in the $0.^\circ5 \times 1^\circ$ region, excluding the inner $17'$ region.*

Source name	Size (arcsec^2)	L_X (2−10 keV) (10^{32} erg s^{-1})	Comment	Reference‡
G0.223−0.012	6×80	15		a
G0.13−0.11	7×33	40	Radio, PWN?	a, b, c, e
G359.55+0.16	4×21	20	Radio, X-ray thread	a, b, f, g, h
G359.43−0.14	4×21	5		a
G359.40−0.08	5×27	24		a
G0.17−0.42	180×18	-	near the Radio Arc	d
Total luminosity (2–10 keV)		1.0×10^{34} erg s^{-1}		

∗ Same as table 12, but listed sources are in the large area of $0.^\circ5 \times 1^\circ$ region around Sgr A*, excluding those of the central region in table 12.

‡ Reference, a: Johnson et al. (2009), b: Wang et al. (2002b), c: Yusef-Zadeh et al. (2002a); Yusef-Zadeh et al. (2002b), d: Ponti et al. (2015), e: Mori et al. (2015) f: Wang et al. (2002a), g: Lu et al. (2003), h: Yamauchi et al. (2014).

from the other bright X-ray filaments, G359.983−0.046 (J174545.5−285829: the Cannonball), G359.89-0.08 (Sgr A-E) and G359.97-0.038, (Nynka et al. 2013; Nynka et al. 2015; Zhang et al. 2014; Mori et al. 2015). With the wide band spectra, X-ray luminosity and photon indexes are determined to be $\sim 10^{33} - 10^{34}$ erg s^{-1}, and $\sim$1.3 – 2.6, respectively.

From the star formation rate at the Galactic center, Muno et al. (2008) estimated that $\sim$20 PWNe are expected in the Galactic center. However, only small fractions of the X-ray filaments are suspected to be PWNe (Muno et al. 2008). Therefore, most of the PWNe would have the X-ray luminosity of $\lesssim 10^{31}$ erg s^{-1}, bellow the detection limit of the sources in table 12.

The X-ray filaments, G359.959−0.027, G359.970−0.008 and G359.974−0.00 have narrow features associated to the radio filaments, and are roughly aligned on a slightly curved line crossing over Sgr A*. These are named knot-1, 2 and 3 by Koyama et al. (2004). The other narrow filament, G359.944−0.052, named Jet by Li et al. (2013), has well collimated structure pointing to Sgr A*located the other side of the Galactic plane. The detailed discussion on these filaments related to the past high activity of the SMBH, Sgr A* are given in section 7.3.

In table 12, the X-ray luminosity is available for 2 thirds of the X-ray filaments, with the luminosity of $\sim 10^{32} - 10^{34}$ erg s^{-1} (2 – 8 keV). The summed luminosity (2 – 10 keV) is $\sim 3.8 \times 10^{34}$ erg s^{-1}. The luminosity of the remaining 1 third is unavailable due to the faintness. Assuming the luminosity of the remaining sources is near the lower limit of the observable luminosity of $\sim 10^{32}$ erg s^{-1}, the summed luminosity of all the X-ray filaments is estimated to be $\sim 4 \times 10^{34}$ erg s^{-1}, only 3 % of the GCXE.

6.2 The Outer Region of the GCXE

The high spatial resolution survey of the whole GCXE of $\sim 2^\circ \times 0.^\circ8$ around Sgr A* is first made by Wang et al. (2002a) with Chandra. Although 8 bright radio non-thermal-filaments are included in this region, only one source, G359.54+0.18 (Yusef-Zadeh et al. 1997) is found as an X-ray filament, named the X-ray thread. With the deeper Chandra survey of $1.^\circ1 \times 0.^\circ57$ around Sgr A*, Johnson et al. (2009) found 17 X-ray filaments, a dozen of them are located in the inner GCXE region of $\sim 10' \times 10'$ and are listed in table 12. The source list in the whole GCXE of $1.^\circ1 \times 0.^\circ57$, excluding the inner region are given in table 13.

Ponti et al. (2015) surveyed nearly the same region with XMM-Newton. Since most of them except G0.17−0.42, are overlapped with Johnson et al. (2009), the sources listed in tables 13 are mainly due to Chandra observations. The References in table 13 indicate the other authors who observed the relevant sources.

The X-ray filament G0.13−0.11 is the brightest, and is the most studied X-ray filament in this region. This name and its features are confusing, because other nearby objects with similar names but different natures are presented. The radio MC, G0.13−0.13 is found to be a Fe I-Kα line source (Yusef-Zadeh et al. 2002a; Yusef-Zadeh et al. 2002b), and is claimed that the Fe I-Kα line is due to LECRe. However the selected area is rather large ($4' \times 3'$), and hence is contaminated by a nearby XRN, G0.11−0.11 (table 9). The diffuse soft X-ray source, a candidate of an intermediate-aged SNR, G0.13−0.12 is near at the filament G0.13−0.11 (section 4.2.1).

Wang et al. (2002b) found that the X-ray spectrum of G0.13−0.11 is a simple power-law with the luminosity of $\sim 3 \times 10^{33}$ erg s^{-1}. From the head of G0.13−0.11, a point source CXOGCS J174621.5−285256 is found with a power-law photon index and the 2 – 10 keV band luminosity of $0.9^{+0.9}_{-0.7}$, and $\sim 8 \times 10^{32}$ erg s^{-1}, respectively. This luminosity is $\sim$30 % of

the whole G0.13−0.11. The morphology, spectrum and luminosity indicate that G0.13−0.11 is the leading edge of a PWN, produced by a pulsar CXOGCS J174621.5−285256 moving in a strong magnetic field environment. The main body of this PWN is likely traced by a bow-shaped radio feature, which is apparently bordered by G0.13−0.11, and is possibly associated with the prominent non-thermal radio filaments. The origins may be due to synchrotron radiation, or inverse Compton scattering of far-infrared photons from dust by the relativistic electrons responsible to the radio synchrotron emission. The magnetic field strength is estimated to be 0.08 mG within the radio NTF (Yusef-Zadeh et al. 2005).

The source density in the outer region (table 13) is far smaller than that of the inner region (table 12). This is, at least partly, due to the higher detection threshold luminosity in the larger area of the outer region than that of the inner region. In fact, most of the X-ray luminosity (2 – 10 keV) of the table 12 sources is $\lesssim 10^{33}$ erg s^{-1}, while those in table 13 are $\gtrsim 10^{33}$ erg s^{-1}. The source sizes of the inner region are also smaller than those of the outer region, except some distance X-ray filaments from Sgr A*.

The summed luminosity (2 – 10 keV) of all the resolved X-ray filaments is $\sim 1.0 \times 10^{34}$ erg s^{-1}. Assuming that G0.17−0.42 has the luminosity of $\sim 5 \times 10^{32}$ erg s^{-1}, the lower limit of the detection threshold, the total luminosity is estimated to be $\sim 1.1 \times 10^{34}$ erg s^{-1}, ∼1 % of the GCXE and one quarter of all the point sources in the inner GCXE region (section 6.1).

7 Past X-Ray Flares of Sgr A*

Sgr A* is the brightest radio point source located at the dynamical center of Our Galaxy. The observations of accurate motions of the IR stars in the close vicinity of Sgr A* revealed that the mass of Sgr A* is $\sim 4 \times 10^6\ M_\odot$ (e.g. Genzel et al. 2010), and hence established that Sgr A* is a SMBH. The fine X-ray image with Chandra resolved Sgr A* from nearby X-ray sources for the first time (Baganoff et al. 2003). The resultant X-ray flux is very low of $\sim 10^{33}$ erg s^{-1}. This quiescent flux of the SMBH would be due to a small mass flow rate within the Bondi radius. The accretion flow structure of ~ 0.6 pc size would be marginally resolved (Baganoff et al. 2003).

Many X-ray outbursts, possibly due to fluctuations of mass accretion rate of a time scale ∼ minutes – hours, have been observed with the rate of ∼1 flare / day. The photon index in the flare spectrum is $\Gamma \sim 2$, similar to AGNs. The maximum peak luminosity is $10^{35} - 4 \times 10^{35}$ erg s^{-1}, ∼ a few 100 times of quiescent flux of $\sim 10^{33}$ erg s^{-1} (Porquet et al. 2003; Porquet et al. 2008). Still, this maximum flux is extremely lower than any of the AGNs. Has Sgr A* always been quiet in the past ? This section reviews possible relics of big flares or high activities of Sgr A* in the past: the X-ray echo from Sgr A* (XRNe) (section 7.1), recombining plasma near at Sgr A* (section 7.2), and jets and outflow structures from Sgr A* (section 7.3).

7.1 X-ray Echo as a Relic of the Past Activities of Sgr A*

The XRNe are dense MCs of large $N_{\rm H}$ (see section 5). Thus, the observed GCXE spectrum behind the XRN (here, GCXE1) is largely absorbed by the MC, while that in front of the XRN (here, GCXE2) is not absorbed by the MC. The observed spectrum at the XRN position is the sum of the GCXE1, GCXE2 and XRN spectra.

Ryu et al. (2009) fitted the Suzaku X-ray spectra from Sgr B2 XRNe by the combined models of GCXE1 plus XRN, and GCXE2, where the former component has a large absorptions of $N_{\rm H}(Abs1)$ due to the absorption of the MC, while the later has a small $N_{\rm H}(Abs2)$. The parameters of $Abs1$ and $Abs2$ are absorptions by the MC+ISM, and by the ISM only, respectively. The schematic view is given in figure 8 (left). The best-fit $N_{\rm H}(Abs1)$ is $> 10^{23}$ cm^{-2}, consistent with the absorption of the dense MC+ISM (table 7), while the best-fit $N_{\rm H}(Abs2)$ is $\sim 6 \times 10^{22}$ cm^{-2}, consistent with that of the ISM. Assuming that the GCXE is spherically extended around Sgr A* with a uniform flux density, the line-of-sight position of the XRN is approximately estimated by the best-fit flux ratio of the GCXE1 and GCXE2 spectra. The projected position (2-diemnssional) and the line-of-sight position provides the 3-dimensional position of the XRN. The positions in the face-on-view of Sgr B XRNe are given in figure 8 (center). Here and after, this method of 3-dimensional position determination is called, the X-ray tomography technique.

The Sgr C complex is composed of three XRNe (C1, C2 and C3: table 10). These are located nearby in projection with each other. Ryu et al. (2013) applied the X-ray tomography method to the XRNe, C1, C2 and C3, and found that these XRNe are largely separated in the line-of-sight positions; C1 and C3 are near side of the Galactic plane, while C2 is far side. These are separately associated to the MCs in different velocity ranges of the radio observations. The face-on-view of the positions of C1, C2 and C3 are shown in figure 8 (center).

Using the 3-dimensional positions, the distances of the XRNe from Sgr A* are determined. Then, using the best-fit fluxes and MC absorptions ($N_{\rm H}$) of $N_{\rm H}(Abs1) - N_{\rm H}(Abs2)$, the past luminosity of Sgr A* is estimated. The age of the past is light-traveling time difference between the direct pass to the Earth from Sgr A*, and the pass from Sgr A* via the XRNe and to the Earth. Thus, the X-ray tomography analyses of many XRNe make the X-ray activity history of Sgr A* as is shown in figure 8 (right).

The X-ray luminosity of Sgr A* has been continuously high level of $L_{\rm X} \sim (1-3) \times 10^{39}$ erg s^{-1} in the past of ∼70 – 500

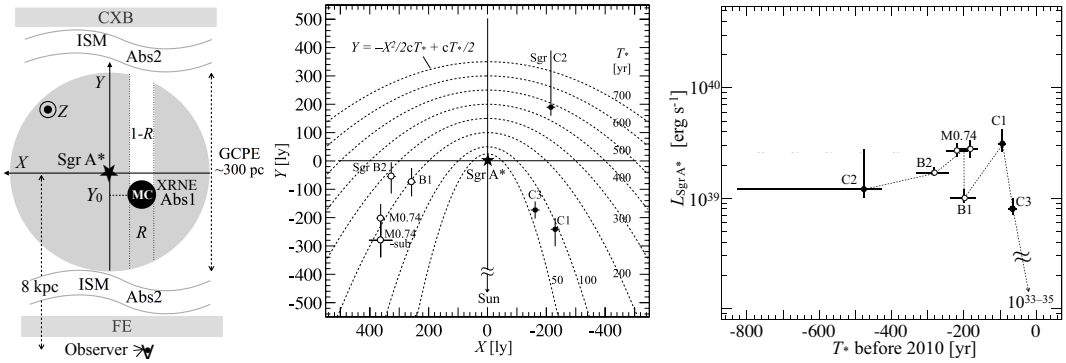

Fig. 8. Left: Schematic view of the X-ray tomography to get the line of sight position of the XRNe. The notations of FE and Z are foreground emission and Z-axis of the coordinate (X-Y-Z), respectively. Center: Face-on view of the positions of XRNe in the Sgr C complex (filled circles) and those in the Sgr B complex(open circles).The parabolas (dashed lines) represent the equal-time delay (T_*) contours for the X-ray echoes from Sgr A*. Right: X-ray light curve of Sgr A* in the past $\sim$500 years. Data points of Sgr C and Sgr B are shown by filled and open circles, respectively (From Ryu et al. 2009 and Ryu et al. 2013). The present luminosity of Sgr A* is quoted from Baganoff et al. (2003); Porquet et al. (2003).

years ago. Then, about 70 years ago, the luminosity dropped down to the current low level. The averaged past luminosity is $\sim$4 – 6 orders of magnitude higher than the present luminosity. In addition, at least two short-term flares with the timescale of a few years are found. Thus, the high luminosity level of the $\sim$70 – 500 years ago is not due to a single flare of long duration, but would be due to multiple, overlapping short flares.

To fill the blank ages of < 70 years ago in the past Sgr A* activity history, similar tomography method should be applied to the Sgr A XRNe complex, because these XRNe are the nearest sample ($\sim$ 30 – 80 light-years in projection) to Sgr A*. However, the tomography method requires very accurate spectra with Suzaku. Unfortunately, the XRNe density in the Sgr A MC complex is too high (see table 9) to be separately observed with the limited spatial resolution of Suzaku.

Using XMM-Newton, Ponti et al. (2010) determined the line-of-sight positions of XRNe in the Sgr A MC complex. They assumed a long flare ($\sim$ 100 year) of constant flux of $\sim 10^{39}$ erg s^{-1}, and that all the XRNe in the Sgr A complex are behind the projected Galactic plane. From the observed fluxes and $N_{\rm H}$ of the XRNe, they determined the distance from Sgr A*, and hence predicted the 3-dimensional positions of the XRNe, Bridge, M1, M2 and G0.11-0.11. This method of Ponti et al. (2010), however gives no information on the light curve of Sgr A*, because the flux is a priori assumed to be constant.

Capelli et al. (2012) also determined the line-of-sight positions of XRNe in the Sgr A MC complex using equation (4); the XRNe of the minimum EW$_{6.4}$ have the scattering angle of $\theta = 90^\circ$, on the line of the projected Galactic plane. The other XRNe with larger EW$_{6.4}$ would be located either in front or behind the line of $\theta = 90^\circ$ (equation 4). To resolve this degeneracy of in front or behind, they grouped the 9 XRNe in table 9 into 3 groups, according to their time variability profiles. Group 1 is decreasing flux (B1 and F), Group 2 is increasing flux (B2, C and D), and Group 3 is constant flux (A, E, DS1 and DS2) (see section 5.2.2). They assumed that the XRNe in the same group were irradiated by the same flare of a few ten years duration (observed time scale of the variability). Then, using the observed EW$_{6.4}$, they determined the 3-dimensional positions of the XRNe. From the observed fluxes and the column density $N_{\rm H}$ of the XRNe, they made the X-ray light curve of Sgr A* in the past of $\sim$70 – 130 years ago, with the average luminosity of $\sim 10^{37} - 10^{38}$ erg s^{-1}.

As is noted in section 5.2.2, Clavel et al. (2013) found many bright Fe I-Kα flares from small spots of $26'' \times 61''$ ($\sim$1 pc$\times$2.4 pc) or $15''$ ($\sim$0.6 pc) square. Since the flare peaks are $\sim$10 time brighter than those in the quiescent level, they proposed that the past flare of Sgr A* are composed of multiple short flares of $\sim$a few years duration with the peak luminosity of $\sim 10^{39}$ erg s^{-1}, overlaid on the lower level and longer duration ($\sim$10 year) flares.

The key factor to determine the 3-dimensional positions of the XRNe by Capelli et al. (2012) is reliability of the absolute EW$_{6.4}$. However the observed EW$_{6.4}$ has large systematic errors as is noted in sections 5.2.2. The EW$_{6.4}$ of the XRNe depends on the subtraction of a local GCXE background. Since Capelli et al. (2012) used a common GCXE background at $b = -0^\circ.12$ for all the XRNe, but each XRN is located at different position of b, the EW$_{6.4}$ should be $b - 0^\circ.12$-dependent. In fact, $b - 0^\circ.12$ and EW$_{6.4}$ are not randomly distributed, but show a clear anti-correlation as expected from the local GCXE subtraction effect. Accordingly, the line-of-sight positions, hence the predicted light curve has significant systematic errors. The results of Ponti et al. (2010) of the 3-dimensinal positions are inconsistent with those of Capelli et al. (2012), not only due to the different assumption of a single constant flux flare (Ponti et al. 2010) of $\sim 10^{39}$ erg s^{-1}, or multiple short flares of various luminosity of Sgr A*(Capelli et al. 2012), but also due to the

systematic errors of local GCXE subtraction.

Ignoring these uncertainty, the predicted X-ray light curve of Sgr A* by Capelli et al. (2012) in the recent past of $\sim$70 – 130 years ago comes to the decaying phase in the past $\sim$70 – 500 years light curve in figure 8 (right). However the flux is $\sim$10 – 100 times lower than those of C1 and C3 in the same epoch. If all the XRNe are located in front the line of $\theta = 90^\circ$, in contrast to the assumption of Capelli et al. (2012), the light curve would be systematically sifted toward recent ages, at least, less than $\sim$30 – 80 years. In the close vicinity of Sgr A*, there exist two giant MCs, the 50 km s^{-1} and 20 km s^{-1} clouds. However, no Fe I-Kα line is found from these clouds (Park et al. 2005; Ponti et al. 2010). This would be due to the largely declined flare flux of Sgr A* in the recent decades.

7.2 Recombining Plasma: Another Relic of Sgr A* Activity

Sgr A* is located in the Sgr A East SNR. If Sgr A* had been very bright of $\sim 10^{39-40}$ erg s^{-1} during $\sim$70 – 500 years ago (see section 7.1), He-like iron in the hot plasma would be partially photo-ionized to H-like iron, then the plasma would emit the radiative recombination continuum (RRC) at $\sim$8.7 keV (Ozawa et al. 2009). The RRC structure is recently found in the Suzaku spectrum of Sgr A East (Uchiyama et al. 2017). Therefore, the RRC in the Sgr A East spectrum can be regarded as another relic of the past flares of Sgr A*in $\sim$70 – 500 years ago.

Nakashima et al. (2013) found a possible relic of more energetic flares in the far past. They found a peculiar X-ray plasma named GC-South at (l, b)= (0°, $-1.^\circ5$). The emission region is an ellipse with $\sim 21' \times 8'$ in the major and minor radius. The jet-like structure is elongated toward Sgr A*.

The X-ray spectrum of the GC-South plasma exhibits emission lines from highly ionized Si and S. Although the X-ray spectrum of the GBXE around GC-South is well fitted with a CIE plasma (section 3.2), that of GC-South cannot be fitted with a CIE plasma, leaving saw-teeth shape residuals at $\sim$2.5 keV and $\sim$3.5 keV, which are attributable to the RRCs of He-like Si and S, respectively (Yamaguchi et al. 2009). In fact, the GC-South spectrum is well fitted with a RP model. The electron temperature is $\sim$0.46 keV, while the ionization temperature was $\sim$1.6 keV in the initial epoch, and the plasma is now in a recombining phase after the relaxation time scale $n_{\rm e}t$ (electron density $\times$ elapsed time) of $\sim 5.3 \times 10^{11}$ cm^{-3} s.

The absorption column density of the GC-South plasma is consistent with that of the Galactic Bulge (GB). Thus, the GC-South plasma is likely located in the GB region (at 8 kpc distance). Then, the full size of the plasma, the mean electron density ($n_{\rm e}$), and the thermal energy are estimated to be $\sim 97 \times 37$ pc^2, ~ 0.16 cm^{-3} and $\sim 1.6 \times 10^{51}$ erg, respectively (Nakashima et al. 2013). Then, the RP plasma age t ($= n_{\rm e}t/n_{\rm e}$), is $\sim 10^5$ years.

Possible scenario is that the almost fully ionized (at least, for Si and S) plasma is made by a bright flare X-rays of Sgr A* of $\sim 10^5$ years ago, and the plasma is now in recombining phase (RP). Using this scenario, Nakashima et al. (2013) argued that the past flare luminosity of $\sim 10^5$ years ago is near the Eddington limit of $\sim 10^{44}$ erg s^{-1}, more energetic than those of recent flares of $\sim$70 – 500 years ago.

7.3 The Other Possible Relic of Sgr A* Activity

As is noted in section 6.1, Chandra found 3 filaments (knot-1, knot-2 and knot-3) near Sgr A*. These are aligned on almost a straight line, but is slightly curved pointing to Sgr A*. With a power-law model fit, the $N_{\rm H}$ are found to be $\sim (10-16) \times 10^{22}$ cm^{-2}, consistent with the GC distance. Then, the size and luminosity of knot-1, knot-2 and knot-3 are nearly the same of $10'' \times 4''$, and $\sim (2-6) \times 10^{32}$ erg s^{-1}, respectively (Koyama et al. 2004; Muno et al. 2008). The power-law photon indexes are flat of $\lesssim$1.3. From these facts, Koyama et al. (2004) suggested that the three filaments have the same origin; knot-1, knot-2 and knot-3 would be due to sequential plasma ejections from a single source, Sgr A*.

The other jet-like structure G359.944−0.052 (Jet, table 12) has the size of $\sim 2'' \times 19''$, located at the close vicinity in the southeast from Sgr A*with the major axis pointing to Sgr A*. Li et al. (2013) found that the spectrum of Jet is a power-law with the photon index, absorption column and luminosity (2 – 10 keV) of $\sim$1.8, $\sim 12 \times 10^{22}$ cm^{-2} and $\sim 2.4 \times 10^{32}$ erg s^{-1}, respectively. The large absorption column suggests that Jet is located at the GC distance. The photon index and luminosity are typical to a jet of synchrotron emission. The position and major axis of Jet aligns with the curved line connecting Sgr A*, knot-1, knot-2 and knot-3. Thus, it may be conceivable that Jet is a counter jet of knot-1, knot-2 and knot-3, or these are highly collimated magnetized outflows of relativistic particles emanating from Sgr A*(Li et al. 2013).

The ejected epochs of these jets (outflows) can be determined from the 3-dimensional ejection angle and the velocity of the jets, which are all unknown. However the projected distances of the jets are small ($\sim$0.7 – 8 pc), and hence the jet ejections would be recent events. If the past flares of Sgr A*triggered the jet ejections, the flare energies would be significantly large in order to produce such prominent jets.

As noted in section 4.2.3, Heard & Warwick (2013b) found the diffuse thermal sources NW, SE and E in the GC region from the XMM-Newton image. They suggested these 3 sources are young-intermediated aged SNRs. However, some aspects are unusual; the sizes are smaller than typical SNRs of $\sim$1 keV temperatures, the plasma density is very high of $\sim$4.6 – 9.9 cm^{-3},

and the morphology shows bipolar-flow structures emanated from Sgr A* or Sgr A East SNR with angles nearly perpendicular to the Galactic plane. The locations are only $\sim$5 – 10 pc away from Sgr A*. Therefore, they proposed an alternative scenario that these thermal plasmas are outflows driven by intermittent outbursts of Sgr A*. Assuming the velocity is 1000 km s^{-1}, high speed stellar wind of massive star, the timescale for the plasma to reach the $6'$ (14 pc) distance, the most remote position of these plasmas is $\sim 10^4 - 10^5$ years. This is the same age of GC-South (section 7.2).

The Fermi Bubbles are largely extended GeV gamma ray sources of $\sim 50^\circ$ above and below the GC (Dobler et al. 2010; Su et al. 2010). These would be due to starbursts or a nuclear outburst which happened near the Galactic center in $\sim$10 Myr ago. The same idea is firstly proposed by Sofue (2000) to account the North Polar Spur (NPS). The morphology is spatially correlated with the WMAP haze, and the edges of the bubbles also line-up with NPS in the ROSAT X-ray maps. Suzaku revealed a large amount of neutral matter absorbing the X-ray emission towards the bubble direction as well as the existence of the ~ 0.3 keV temperature plasma. These are naturally interpreted as shock-heated Galactic halo during the bubble expansion (Kataoka et al. 2013). The 511 keV line emission by INTEGRAL (Jean et al. 2006; Weidenspointer et al. 2008) would be another hint of the past activity near the GC, or Sgr A*.

8 Methodology to the Origin of the GDXE

The long standing questions regarding the origin of the GDXE are; how much fractions of the GDXE are resolved into point sources, and what are the populations of the point sources. The candidate point sources should have similar spectra (plasma temperatures of $>$ a few keV) to the GDXE and reasonably bright in the 2 – 10 keV band to explain the GDXE flux. These Galactic point sources are, hear and after, defined as the X-ray Active Stars (XAS). The majority of the XASs are the mCVs, non-mCVs and ABs.

In the previous sections, many arguments for the origin of the GDXE are given along these questions. However the predictions are often quantitatively inconsistent from author to author or instrument to instrument. The reasons of these inconsistency are mainly due to large errors of the observed physical parameters (both statistical and systematical), and partly due to confusing definition of XASs (mCVs, non-mCVs and ABs), differences in the energy band of XLF and that of the analysis method of EW_{Fe-K} and so on.

Thus this section discuss in detail on these issues, adopting two methodology to the GDXE origin. One is direct resolution of the GDXE into the XASs. In this section, this approach is referred to as the Flux Integration Method (FIM) of the XASs (section 8.1). The other is a quantitative estimation whether or not, and how much the GDXE spectrum is reproduced by the spectra of the XASs, which is referred as the Spectrum Accumulation Method (SAM) of the XASs (section 8.2).

Non-negligible systematic errors for the origin of the GDEX, regardless in the FIM or SAM approaches, are found in the spectra (e.g. EW_{Fe-K}) and fluxes of the GDXE and the XASs. The next subsections give interpretations and discussions with critical comments on these systematic errors.

8.1 Flux Integration Method (FIM)

The FIM approach is the development of the previous study given in section 2.1.1. If the instrument has enough power to resolve the XASs down to the luminosity limit of $\gtrsim 10^{27}$ erg s^{-1} (2 – 10 keV), the lowest luminosity of the XASs with the plasma temperature of $\sim$ a few keV, the FIM is very simple and straightforward approach. However, even with the highest spatial resolution and deepest exposure observations of Chandra, the resolved XASs are limited in the high luminosity range of $\gtrsim 4 \times 10^{29}$ erg s^{-1}, which is achieved only for the GBXE (Revnivtsev et al. 2009; Hong 2012). Therefore, the XAS fraction must be estimated by the extrapolation of the observed fraction from the high luminosity band to the lowest luminosity limit of $\sim 10^{27} - 10^{28}$ erg s^{-1}, using the empirically made XLF, the cumulative X-ray luminosity as a function of the luminosity of the resolved XASs.

A problem of the FIM is that actually resolved XAS fraction and its XLF have significant uncertainties, variations from author to author, namely the systematic errors. The systematic errors would come mostly from the Non X-ray Background (NXB) [5] subtraction, which is serious in the low luminosity band of $\lesssim 10^{31}$ erg s^{-1}. These systematic errors are separately discussed in the next sections 9.1, 9.2 and 9.3 in detail in the cases of the GBXE, GRXE and GBXE, respectively.

As for the XLF, Sazonov et al. (2006) constructed an XLF (2 – 10 keV) in the luminosity band of $10^{30} - 10^{34}$ erg s^{-1} using the XASs in the solar neighborhood observed with the RXTE and ROSAT. They claimed that the XLF is mainly composed of CVs and ABs with the flux per $M_\odot$ of $\sim 1.1 \times 10^{27}$ erg s$^{-1} M_\odot^{-1}$, and $\sim 2.0 \times 10^{27}$ erg s$^{-1} M_\odot^{-1}$, respectively. The composition ratio of the CV $vs.$ ABs is 1:2. However, a large error exists in the conversion process of the ROSAT luminosity band of 0.1 – 2.4 keV to the RXE luminosity band of 2 – 10 keV. In fact, they estimated that the systematic error in the conversion process is ≥ 50 %. Possibly, the XLF in the lowest luminosity range of $\sim 5 \times 10^{27} - 10^{30}$ erg s^{-1} has even larger systematic error.

Warwick (2014b) constructed another XLF (2 – 10 keV) in

[5] Non X-ray Background (NXB) is cosmic ray induced background and exhibits some K_α lines of various elements.

the luminosity band of $10^{28}-10^{34}$ erg s^{-1}, using the Galactic ridge survey data of XMM-Newton. They claimed that the XLF is composed of CVs and ABs with the fluxes per $M_\odot$ of $\sim 2.5\times 10^{27}$ erg s$^{-1}M_\odot^{-1}$ and $\sim 1.1\times 10^{28}$ erg s$^{-1}M_\odot^{-1}$, respectively. The composition ratio of the CVs $vs.$ ABs is 1:4. These are largely different from that of Sazonov et al. (2006).

Revnivtsev et al. (2009); Hong (2012) made the other XLF (6.5 – 7.1 keV) in the luminosity band of $4\times10^{29}-10^{33}$ erg s^{-1}, using the Chandra data in the GBXE field. The shape of these XLFs are quite different. From the shape of their XLF, Revnivtsev et al. (2009) claimed that the main component are mCVs (high luminosity band) and ABs (low luminosity band). On the other hand, Hong (2012) claimed that the composition is mainly mCVs, quite different from Revnivtsev et al. (2009); Sazonov et al. (2006); Warwick (2014b) of the ABs dominant compositions. These apparent inconsistency in the XLF composition among the authors would come partly from the energy band difference. The ABs spectra become much softer toward the lower luminosity limit, and hence the contribution in the high energy band (e.g. 6.5 – 7.1 keV) become smaller than those of canonical energy band of 2 – 10 keV. The other possibility would be confusion in the definition of the CV and AB; whether the non-mCV (dwarf nova) is included to the CV, included to the AB, or independently treated.

Accordingly, the FIM should be applied separately for the mCVs, non-mCVs and ABs with unified energy band. The sum of these separate FIM estimations is the final solution of the XAS fraction in the GDXE.

8.2 Spectrum Accumulation Method (SAM)

The SAM approach is the development of the early studies given in section 2.1.2. Using Suzaku, Yuasa et al. (2012) predicted that most of the flux of the GDXE are due to the mCVs. Hong (2012); Heard & Warwick (2013a) predicted the same conclusion using Chandra and XMM-Newton spectra, respectively. These scenarios of the mCV dominant origins, however, have a serious problem that the EW_{Fe-K} of the mCVs are far smaller than those of the GDXE. On the other hand, Xu et al. (2016) found that the integrated spectra of the non-mCVs (DNe) in the Suzaku archive, has comparable EW_{Fe-K} to that of the GDXE, and argued that the GRXE is mainly composed of the non-mCVs, as was previously proposed by Mukai, & Shiokawa (1993).

The SAM approaches of Xu et al. (2016); Heard & Warwick (2013a); Yuasa et al. (2012); Hong (2012) to predict the XAS origin for the GDXE have all common problems. They applied selected candidates of XASs, only the mCVs and ABs (except non-mCVs dominant scenario by Xu et al. 2016; Mukai, & Shiokawa 1993 of non-mCVs-dominant scenario). They used the limited information of the EW_{Fe-K} for all the relevant objects, and did not separately examine the origin of the GCXE, GBXE and GRXE involving all the possible candidate XASs. One important note, related to the EW_{Fe-K} is, that the Fe abundances in the observed thermal plasmas of the mCVs, non-mCVs and ABs are different to be $\sim$0.3, $\sim$0.6, and $\sim$0.2 solar, respectively (Nobukawa et al. 2016). In particular, the observed Fe abundances in the mCV plasma of far less than 1-solar are often ignored in most of the mCV dominant scenario. The reasons of the low Fe abundance and the difference among the XASs would be due to the different production and emission mechanisms of the plasmas among the XASs. The real physical process is unsolved problem, but out of the scope of the review.

As for the EW_{Fe-K}, one technical note is that the default choice of the XSPEC package, $eqwith$ uses the continuum flux in the energy range of ±0.3 keV of the center energy of the relevant iron K-shell line. Thus, depending on the data analysis process, the value of $EW_{6.7}$, for example, would be underestimated by the extra flux of the adjacent Fe I-Kα and Fe XXVI-Lyα lines. In the case of two-component spectra of the GDXE , a thermal plasma plus a power-law emission, the $EW_{6.4}$ may be confused, whether it is estimated under the continuum shape of the thermal plasma ($EW_{6.7}$ and $EW_{6.97}$), the power-law continuum ($EW_{6.4}$), or the sum of the both components.

To avoid the source-to-source and author-to-author mismatches in the estimation of EW_{Fe-K}, and utilize the proper comparison between those of the GDXE and XASs, unified data process and analysis for all the GDXE and XASs by the same author are preferred. Nobukawa et al. (2016) determined the EW_{Fe-K} of the GDXE and XASs, using all the Suzaku archive in unified analysis. The results of the GDXE are given in table 5.

The EW_{Fe-K} of the XASs have been measured by many authors, but the qualities and samples were limited (e.g. Yamauchi et al. 2016; Nobukawa et al. 2016 and references therein). Nobukawa et al. (2016) found in the best quality Suzaku spectra that the $EW_{6.7}$ and $EW_{6.97}$ in the XAS spectra are well explained by a CIE plasma with the free parameters of temperature and Fe abundance. The Fe I-Kα line flux would be due to the surrounding cloud, and hence $EW_{6.4}$ is estimated by the parameters of the covering solid angle (Ω), the absorption column ($N_{\rm H}$), and the flux above 7.1 keV. They found a good correlation between $EW_{6.4}$ and the temperature of the mCVs, non-mCVs and ABs with each different free parameters of $\Omega\times N_{\rm H}$. Thus the $EW_{6.4}$ are quantitatively included with the parameter $\Omega\times N_{\rm H}$ for each mCVs, non-mCVs and ABs into the CIE model. Then, all the observed EW_{Fe-K} are well explained by the CIE model, here and after, the 1-T model.

Nobukawa et al. (2016) found that the X-ray luminosity of XASs are well correlated to the temperature of the 1-T model. In the XLF, the relevant luminosity ranges are $\sim 10^{31}-10^{34}$ erg s^{-1}, $\sim 10^{29}-10^{32}$ erg s^{-1} and $\sim 10^{27}-10^{30.5}$ erg s^{-1}, corresponding to the temperature ranges of $\sim$10 – 20 keV, $\sim$3 –

10 keV and $\sim$1 – 3 keV, for the mCVs, non-mCVs and ABs, respectively (table 14). Then, they constructed a two-temperature CIE model (2-T model), as good approximated spectra in the relevant luminosity bands of the XASs [6].

In principle, a multi-T model would be more appropriate than the 2-T model to incorporate the temperature dependent XLF. However, in reality, the 2-T and multi-T models show no large difference beyond the observed statistical errors in the XAS spectra. Accordingly, the GCXE, GBXE and GRXE spectra should be compared with a combination of the 2-T models of the XASs (Nobukawa et al. 2016). The best-fit results are given in table 15. Since the EW_{Fe-K} of the GDXE are more similar to the non-mCVs than any other XASs, it would be reasonable that the non-mCVs occupies the largest fraction in the best-fit results (table 15).

The best-fit χ^2 / d.o.f for the GCXE, GBXE and GRXE spectra are 2637 / 276, 148 / 95 and 282 / 91, respectively. Thus the SAM predicts that a combination of the XASs can explain the spectra of the GBXE, but not for the GRXE and GCXE spectra. Detailed discussions are separately given in sections 9.1, 9.2 and 9.3 for the GBXE, GRXE and GCXE, respectively.

The SAM approach using the 2-T model is less sensitive to the assumed XLF than the FIM. This is a large advantage of the SAM over the FIM. Possible systematic errors due to NXB subtraction would be also less sensitive than the FIM. In fact, the EW_{Fe-K} in the Suzaku GCXE spectra were almost the same among the authors (see section 3.3), although the data reductions and analysis methods were independent. The 2-T model of Nobukawa et al. (2016) smeared-out position-to-position variations in the GDXE, because they used the larger area for the GDXE spectra than any of the other authors or instruments.

The realistic error of the most important parameter, the mean EW_{Fe-K} of non-mCV, is statistically estimated using the standard deviation of the 13 non-mCVs sample (Nobukawa et al. 2016), and resultant 1-σ error is $\sim 10\,\%$. As the results, the best-fit composition ratios of the mCVs, non-mCVs and ABs (table 15) would have a systematic error of $\sim \pm 0.1$. This, however, has no serious impact on the discussion for the origin of the GDXE given in section 9.

8.3 Combined Approach of the FIM and SAM

In the FIM approach, the essential points are to obtain a reliable fraction of the resolved XASs, and a reliable XLF down to the limiting luminosity of $\sim 10^{27}$ erg s^{-1}. The best instrument for the FIM is Chandra, because of the best spatial resolution of $\sim 1''$, two orders of magnitude better than Suzaku. The weakest point is its large NXB, about 10 times larger than Suzaku. Therefore, possible flux errors due to the NXB subtraction are not negligible for the low surface brightness sources, the GBXE and GRXE, and faint XASs.

[6] It is better to refer the original paper of Nobukawa et al. (2016), because the process to construct the 2-T models is very complicated.

Table 14. Physical Parameters of the mCV, non-mCV and AB.*

	mCV	non-mCV	AB
kT_e (keV)	$23.3^{+5.1}_{-3.7}$	10.7 ± 1.7	4.25 ± 0.18
Lx (erg s^{-1})	10^{31}–10^{34}	10^{29}–10^{32}	10^{27}–$10^{30.5}$
SH (pc)†	130–160	130–160	150–300
$EW_{6.4}$(eV)	169±5	82±7	28±5
$EW_{6.7}$(eV)	118±7	451±10	327±8
$EW_{6.97}$(eV)	60±7	167±9	45±6

∗ Errors are 1 σ confidence level.

† Ak et al. (2008), Patterson (1984) and Strassmeier et al. (1993).

Table 15. The best-fit fraction of the mCV, non-mCV and AB spectra (after Nobukawa et al. 2016).

	GCXE	GBXE	GRXE
Source		Fraction†	
mCV	0.04($<$ 0.01)	0.03($<$ 0.09)	0.10±0.05
non-mCV	0.96±0.01	0.67±0.06	0.51±0.06
AB	0.00 ($<$ 0.01)	0.30±0.03	0.39±0.02
χ^2/d.o.f.	2637/276(9.55)	148/95(1.56)	282/91(3.10)

†Fraction of the surface brightness of mCV, non-mCVs and ABs. After Nobukawa et al. (2016).

In the SAM approach, the essential points are to obtain reliable spectra of the GDXE (GBXE, GRXE and GCXE), and the XASs (mCVs, non-mCVs and ABs). The key parameters are the values of EW_{Fe-K}, which are sensitive to the continuum levels, or the NXB subtractions. Suzaku is the best instrument for the SAM approach, because of the reasonably large effective area and good spectral resolution. The NXB is about 10 times lower than Chandra, and the stability and reproducibility of the NXB are fur better than Chandra and XMM-Newton.

Whichever the FIM and SAM, to minimize possible systematic errors are to utilize the best instruments for FIM and SAM, and carry out unified analysis for the GDXE and XASs. In order to minimize the author-to-author systematic errors, simultaneous and unified study with Chandra (FIM) and Suzaku (SAM) by the same researchers is important. Currently, no such unified work has been available. Therefore, independent approaches by the FIM and SAM should be complementally applied to the origins of the GDXE. If the fluxes are not explained by the FIM, and / or if the spectra are not well explained by the SAM, new sources other than the known XASs must be involved, regardless point-like or diffuse.

So far, the point source origin of the GDXE led by the FIM, is more widely accepted, because the FIM is a simple approach, and has no risk to involve any new Galactic sources, or new physical processes other than the emissions of the known XASs. On the other hand, although the SAM did not exclude the contri-

bution of the known XASs in some fractions, the SAM did not elude a risk to involve new objects or new concepts of uncommon physical processes. Due to this risk, the SAM approach has been less accepted. In the next section, the origin and structure of the GBXE (section 9.1), GRXE(section 9.2) and GCXE (section 9.3) are discussed separately, applying equally both the FIM and SAM.

9 Origins of the GCXE, GBXE and GRXE

The true origins of the GDXE are not conclusive, due to non-negligible errors of the observed results. The important fact is that the EW_{Fe-K} and SH_{Fe-K} are all different among the GCXE, GBXE and GRXE. Therefore, the origin of the GBXE, GRXE and GCXE should be separately discussed, which are given in subsectios 9.1, 9.2 and 9.3, respectively.

9.1 Galactic Bulge X-Ray Emission (GBXE)

Revnivtsev et al. (2009) conducted deep observations ($\sim$1 Msec) in the region of $(l, b) = (0.^\circ1, -1.^\circ4)$, named the Chandra Bulge Field (CBF). Although the CBF is near the GC, Yamauchi et al. (2016) found that the flux ratio of the GBXE component to that of the GCXE at $(l, b) = (0.^\circ1, -1.^\circ4)$ is more than $\sim$10 (see figure 3). Thus, the CBF is not in the GCXE region but is almost in the pure GBXE region.

In the central region of the CBF, Revnivtsev et al. (2009) applied the FIM. The XLF in the 6.0 – 7.1 keV band shows a slow increase in the luminosity range of $\sim 10^{30} - 10^{32}$ erg s^{-1} (2 – 10 keV). The resolved XAS fraction at 10^{30} erg s^{-1} (2 – 10 keV) is ~ 50 %, then turns to a rapid increase in the luminosity range of $\sim 4 \times 10^{29} - 10^{30}$ erg s^{-1}, and finally the resolved XAS fraction becomes ~ 80 % of the GBXE at the lowest luminosity limit of $\sim 4 \times 10^{29}$ erg s^{-1} (2 – 10 keV). They predicted that the rapid increase of the XLF in the low luminosity band is due to the increasing contribution of ABs, and hence contribution of ABs to the GBXE is very large at the low luminosity band.

In the same central region of the CBF, Hong (2012) made another XLF using the same data set and energy band of Revnivtsev et al. (2009). His XLF shows a monotonous increase toward the low luminosity. The resolved XAS fraction at 10^{30} erg s^{-1} is already $\sim$60 – 70 %, then becomes slow increase to $\sim$70 % at $\sim 4 \times 10^{29}$ erg s^{-1} (2 – 10 keV). He predicted that the smooth XLF is due to a single class of the XASs, namely mCVs, and suspected that more than $\sim$70 % of the GBXE is resolved into mCVs, in contrast to the prediction of Revnivtsev et al. (2009).

Morihana et al. (2013) reported that the EW_{Fe-K} of the resolved point sources in the CBF is $\sim$100 eV in the luminosity range of $\gtrsim 10^{32}$ erg s^{-1} (2 – 8 keV), where they regarded the candidate point sources are the mCVs and AGNs (see also Hong 2009). The EW_{Fe-K} increases by a constant rate in the range of $7 \times 10^{30} - 7 \times 10^{31}$ erg s^{-1} (2 – 8 keV) (see figure 13 of Morihana et al. 2013), possibly due to an increasing contribution of the non-mCVs and / or ABs. In the range of $\lesssim 7 \times 10^{30}$ erg s^{-1} (2 – 8 keV), the EW_{Fe-K} become nearly equal to $\sim$300 eV, where main contributors would be non-mCVs and / or ABs. This trend, at least semi-quantitatively, is consistent with Revnivtsev et al. (2009), but is against the mCV dominant scenario of Hong (2012).

The causes of the significant difference of the XLF profiles between Revnivtsev et al. (2009) and Hong (2012) would be found in the difference of the resolved XASs in the low luminosity band of $\lesssim 10^{30}$ erg s^{-1} (2 – 10 keV). Most of the resolved XASs in this faintest luminosity range are uncommon between Revnivtsev et al. (2009) and Hong (2012). These inconsistency may come from the difference of the NXB estimation and related analysis, because the surface brightness of the NXB at $\sim$6 – 7 keV is $\sim$10 times larger than the X-ray flux in the CBF (Hong 2012). In fact, Hong (2012) re-analyzed the same data of Revnivtsev et al. (2009), and found that the XLF inconsistency is disappeared.

Another problems in these authors is their flat spectra of the CBF X-rays and those of the resolved XASs. These are found in figure 3 of Revnivtsev et al. (2009) and figure 6b of Hong (2012). Comparing with the GBXE spectrum of Nobukawa et al. (2016), the flat spectra of Revnivtsev et al. (2009) and Hong (2012) would be due to under-subtraction of the NXB [7].

Morihana et al. (2013) reported that the EW_{Fe-K} in the CBF X-rays may be $\sim$580 eV [8], which are significantly smaller than that of the whole GBXE by Nobukawa et al. (2016) of $\sim$720 eV (table 5). This discrepancy would be either the difference of the selected regions, or more likely due to incomplete NXB subtraction of Chandra.

Yuasa et al. (2012) observed the GBXE and GRXE regions with Suzaku. The spectra are fitted with a model spectrum of the mCVs. The essence of this fit is to reproduce the $EW_{6.7}$ and $EW_{6.97}$ values, by the two free parameters of the mCV mass (white dwarf mass) and Fe abundances; the free parameter of mCV mass tunes the ratio of $EW_{6.7}$ / $EW_{6.97}$ (plasma temperature), while the Fe abundance tunes the absolute $EW_{6.7}$ (and $EW_{6.97}$) value. The other important value of the $EW_{6.4}$, is independent free parameter. Therefore, their mCV-dominant model should obviously gives a nice fit to the spectra of the GBXE

[7] The spectral comparison between Revnivtsev et al. (2009), Hong (2012), and Nobukawa et al. (2016) is not straightforward, due to different unit of the vertical axis (intensity) of keV s^{-1} keV^{-1}, keV^2 s^{-1} keV^{-1}, and photons s^{-1} keV^{-1}, respectively

[8] This result is confusing because Morihana et al. (2013) stated this value in the text, however $\sim$300 eV of the resolved XASs at the luminosity of $\lesssim 10^{30}$ erg s^{-1} is found in their figure 13, and they argued most of the CBF flux is resolved to XASs.

and GRXE, in particular in the most important energy band of around Fe-Kα lines. The best-fit mCV mass and Fe abundance for the GBXE are $\sim 0.7 M_{\odot}$ and $\sim$0.8 solar, while those for the GRXE are $\sim 0.7 M_{\odot}$ and $\sim$0.9 solar, respectively. The 10 % smaller abundance of the GBXE than the GRXE is consistent with that the $EW_{6.7}$ and $EW_{6.97}$ of the GBXE are about 10 % smaller than those of the GRXE (table 5).

Since the Fe abundance in the hot plasma of the mCVs in the solar neighborhood is $\sim$ 0.3 solar (e.g. Yamauchi et al. 2016, Nobukawa et al. 2016, and references), the hot plasma in the mCV-dominant model by Yuasa et al. (2012) should have $\sim$3 times larger Fe abundance than those of the solar neighborhood. However, the flux profiles along the large range of $|l|$= 1° – 100° in the continuum and in the Fe-Kα line bands are globally very similar with each other (Revnivtsev et al. 2006a; Revnivtsev et al. 2006b) (see sections 2.1 and 2.3). Therefore, the Fe abundance should be nearly constant in the wide range of the GRXE and GBXE regions. As is noted in section 5.2.2, the Fe abundance over the whole GCXE is nearly the same of $\sim$1.1 – 1.2 solar. The infrared star observations also show a global uniformity of Fe abundances in the wide range from the Galactic ridge to the Galactic center (e.g. Cunha et al. 2007, and references therein). Thus the Fe abundance is almost the same in the whole GRXE, GBXE and GCXE regions, in conflict to the mCV dominant scenario for the GBXE spectrum by Yuasa et al. (2012); Hong (2012).

The $SH_{6.7}$ and $SH_{6.97}$ of $\sim$310 pc (2°.2) and the $SH_{6.4}$ of $\sim$160 pc (1°.1) in the GBXE (Yamauchi et al. 2016, and see table 4) are globally consistent with those of the XASs of $\sim$130 – 300 pc (see table 14). Therefore, Nobukawa et al. (2016) tried the SAM approach with the 2-T models of the XASs spectra (see 8.2). Unlike Yuasa et al. (2012), the 2-T models of Nobukawa et al. (2016) are based on the real observed values of the temperatures and Fe abundances to predict all the EW_{Fe-K} for all the XASs.

Nobukawa et al. (2016) obtained a reasonable fit with χ^2/d.o.f=148 / 95 by the combined 2-T models (table 15). Then, they concluded that the major fraction of the GBXE is due to the non-mCVs and ABs. The predicted ABs ratio of 30 % is far smaller than the AB-dominant scenario by Revnivtsev et al. (2009) and far larger than the mCV-dominant scenarios by Yuasa et al. (2012); Hong (2012). Although the flux of the non-mCVs is about 10 times lower, the space density is 10 times larger than those of the mCVs (Patterson 1984). Therefore, it may not be surprising that the non-mCVs is the main contributor to the GBXE, in contrast to the many previous predictions .

In summary, ignoring possible systematic errors in the FIMs, a common consensus is that $\sim$70 – 80 % of the GBXE flux is explained by either the mCVs, non-mCVs, ABs, or some mixture of these sources (Revnivtsev et al. 2009; Hong 2012). This prediction is consistent with the SAM prediction (Nobukawa et al. 2016). However, the composition ratios are different between the FIM and SAM and even among the FIMs. Furthermore, this prediction comes from the works of limited area of the GBXE, the CBF of $|l| = 0.^{\circ}0$, $|b| = -1.^{\circ}4$, in the FIM, and the off-plane field of $|l| < 0.^{\circ}6$, $1.^{\circ}0 < |b| < 3.^{\circ}0$ in the SAM. Therefore, unsolved questions are still remained; which is the major contributor, the mCVs, non-mCVs or ABs ? How much is the mixing ratio of these sources in all the GBXE region ?

9.2 Galactic Ridge X-Ray Emission (GRXE)

The deepest point source survey in the GRXE was made with Chandra by Ebisawa et al. (2001); Ebisawa et al. (2005) near at $(l, b) = (28.^{\circ}5, -0.^{\circ}2)$, named the Galactic Ridge Field (GRF). Ebisawa et al. (2005) resolved $\lesssim$10 % of the GRF flux into XASs at the detection threshold luminosity of $\sim 2 \times 10^{31}$ erg s^{-1} (2 – 10 keV). In the same region (GRF), Revnivtsev et al. (2007a) reported that the resolved XAS fraction is $\sim$19 % in the luminosity range of $\sim 10^{30} - 10^{32}$ erg s^{-1} (1 – 7 keV). This ratio is converted to $\sim$10 % at the detection threshold luminosity of $\sim 2 \times 10^{31}$ erg s^{-1}, using the the mean XLF (Sazonov et al. 2006; Hong 2012; Warwick 2014b).

Warwick (2014b) applied the FIM to the origin of the GRXE. They assumed that the resolved XAS fraction is the same as Ebisawa et al. (2005); Revnivtsev et al. (2007a). Then, they extrapolate this fraction to the low luminosity limit of $\sim 10^{28}$ erg s^{-1} along to their XLF, which is made by the XMM-Newton archives. They argued that more than 90 % of the GRXE flux in the GRF is resolved into the XASs (2 – 10 keV) with the composition ratio of the CVs:ABs of about 1:4 (section 8.1). This FIM results however, may have a large uncertainty due to the ambiguity of the XLF profiles sensitive to the ABs temperature near at the low luminosity limits of less reliable data. Furthermore, the observed surface brightness of the GRXE obtained with Chandra (Ebisawa et al. 2001; Ebisawa et al. 2005; Revnivtsev et al. 2007a) and XMM-Newton (Hangs 2004) are about 1.3 times larger than those of Suzaku (Ebisawa et al. 2008; Nobukawa et al. 2016). These differences may be also due to some systematic errors of the NXB subtraction in the Chandra and XMM-Newton data.

For the SAM approach, Warwick et al. (2014a) analyzed the XMM-Newton slew survey on the Galactic plane data, and reported that the spectrum of the resolved XASs in the luminosity band of $\gtrsim 8 \times 10^{32}$ erg s^{-1} (2 – 10 keV) has the $EW_{6.4}$, $EW_{6.7}$, and $EW_{6.97}$ of $\sim$90, $\sim$170, and $\sim$80 eV, respectively, and hence they claimed that the origin of the GRXE is mCVs in the luminosity band of $\gtrsim 8 \times 10^{32}$ erg s^{-1} (2 – 10 keV) . This conclusion may be correct, because the EW_{Fe-K} values in this high luminosity band are very close to those of the mCVs (Nobukawa et al. 2016).

Xu et al. (2016) found that Suzaku spectrum of the non-mCV is similar to the GRXE. Since the observed luminosity of the non-mCV did not cover the low luminosity band of the XLF, they made a model spectrum of the non-mCVs to include full luminosity range of the XLF. The model spectrum of the non-mCVs is also very similar to the GRXE. Therefore, they predicted that the majority of the GRXE is due to unresolved non-mCVs. However their model of non-mCVs is taken into account of only the $EW_{6.7}$ values.

The spectra of the GRXE have been observed with Suzaku, in the regions of sub-degree to a few degree size at $|l| \sim 8^\circ$, 15° and 28° on the Galactic plane by Ebisawa et al. (2008); Yamauchi et al. (2009). Due to the low surface brightness and limited exposure time of $\sim 50-100$ ksec, all the EW_{Fe-K} are not determined except the $EW_{6.7}$. The $EW_{6.7}$ are variable from position to position in the range of $\sim 350-640$ eV, larger than the statistical errors of typically ~ 100 eV. These large position-to-position variations suggest that the origin of the GRXE is not fully due to the assembly of numerous XBSs.

The large statistical errors and large position-to-position variations of the EW_{Fe-K} do not allow any quantitative study of the SAM. To increase statistics and to smear-out the position-to-position variations, Nobukawa et al. (2016) made the GRXE spectrum using all the Suzaku archives. The total exposure time is 3 Msec, two orders of magnitude larger than those of the individual positions, and hence the statistical error of the $EW_{6.7}$ is reduced to be ~ 10 eV (table 5). They fitted the GRXE spectrum with a combination of the 2-T models of the XASs (section 8.2). The fit is rejected with χ^2 / d.o.f=282 / 91 (table 15).

Although statistically rejected, the best-fit composition ratio of the mCV, non-mCV and ABs is 1: 5: 4, similar to the GBXE of 0.3: 6.7: 3 (table 15). Therefore, the shapes of the XLF of the GBXE and GRXE would be similar with each other. The XAS fraction of the GBXE at the luminosity limit of $\sim 2\times10^{31}$ erg s^{-1}(Revnivtsev et al. 2009; Hong 2012) is $\sim$3 times larger than the GRXE. If the same XLF of the GBXE is applied to the GRXE, the resolved XAS fraction of the GRXE (Ebisawa et al. 2005; Revnivtsev et al. 2007a) is estimated to be $\lesssim$30 % of the GRXE at the same luminosity limit of $\sim 2\times10^{31}$ erg s^{-1}. Thus, observational facts of both the FIM and SAM suggest that the GRXE is composed of not only the XASs, but has an additional component, either new class of point or diffuse sources.

Excluding the poor statistic band of $\gtrsim 7.5$ keV, the largest residual from the combined 2-T model is the excess flux of Fe I-Kα line. Yamauchi et al. (2016) found that the $SH_{6.4}$ is $\sim$70 pc, smaller than any of the XASs (table 14), but is rather similar to that of the MCs. Nobukawa et al. (2015) found the $EW_{6.4}$ excess, at the east of the Galactic plane of $l_* = 2^\circ - 4^\circ$, b_*=0° compared to the west of the same, but negative longitude. In the X-ray spectra from both the east and west regions, the Fe XXV-Heα and Fe XXVI-Lyα fluxes are almost the same between the east and west, while the Fe I-Kα flux shows nearly 2 times larger excess in the east compared to the west.

Then, they subtracted the west spectrum from that of the east, and made the X-ray spectrum of the east excess. They fitted the spectrum with a model of a power-law continuum and a Gaussian line for the Fe I-Kα line at 6.4 keV. The best-fit photon index and $EW_{6.4}$ are 3 ± 1 and 1.3 ± 0.4 keV, respectively. These values are well explained by a scenario of LECRp bombardment. Thus, a significant contribution of the Fe I-Kα line in the GRXE would come from a bombardment to the MCs by LECRp (Nobukawa et al. 2015; Yamauchi et al. 2016; Nobukawa et al. 2016), although possibility of X-ray irradiation by bright XBs (Sunyaev et al. 1993) or LECRe bombardment (Valinia et al. 2000) would be partly possible.

Sato et al. (2014); Sato et al. (2016); Nobukawa et al. (2017b) found the excess of Fe I-Kα line from regions of seven intermediate-old aged SNRs in the region of $6^\circ \lesssim l \lesssim 35^\circ$ and $|b| \lesssim 0^\circ.5$. Since the diffuse hard X-ray flux (e.g. 5 – 10 keV band) is negligibly small, these SNRs are not identified as point sources, then the excess of the Fe I-Kα flux is regarded to be position-to-position fluctuations in the GRXE. Even X-ray undetected intermediate-old aged SNRs would make LECRp, and produce the Fe I-Kα line by the bombardment on the MCs.

In summary, the FIM did not explain the full flux of the GRXE by XASs. The SAM predicts the regions of the excess of $EW_{6.4}$ over the assembly of the mean spectra of the XASs. Thus, an additional component is required, which is spatially clumpy and emits strong Fe I-Kα lines, possibly MCs by the bombardment of LECRp.

9.3 Galactic Center X-Ray Emission (GCXE)

In the deep observation with Chandra of $\sim$600 ksec exposure of $17' \times 17'$ (40 pc$\times$40 pc) field around Sgr A*, Muno et al. (2003); Muno et al. (2004a) resolved $\sim$10 % and $\lesssim$20 % (2 – 8 keV) into XASs, respectively. With the $\sim$800 ksec observation in the fan-shaped region in the GC west of $2' - 4'$ from Sgr A*, Revnivtsev et al. (2007b) resolved $\sim$40 % (4 – 8 keV band) into XASs at the same threshold luminosity of $\sim 10^{31}$ erg s^{-1}. Thus, even if taking account of the energy band difference, there is an extremely large difference by $\sim$2 – 4 between these two authors with the mean (averaged) XAS fraction of $\sim$25%. This mean value is about 2 times smaller than that of the GBXE by Hong (2012). Therefore, the XAS fraction of the GCXE would be about half of the GBXE or $\sim$40% of the GCXE.

With Suzaku, Uchiyama et al. (2011) made spatial profiles of the Fe-Kα lines in the GDXE with the resolution of $0^\circ.1$. Then, they compared the flux distribution of the Fe XXV-Heα line, the brightest iron K-shell line, with the SMD model, where the SMD flux is normalized to the X-ray flux in the GRXE. The results are shown in figure 9. The Fe XXV-Heα flux in the GCXE

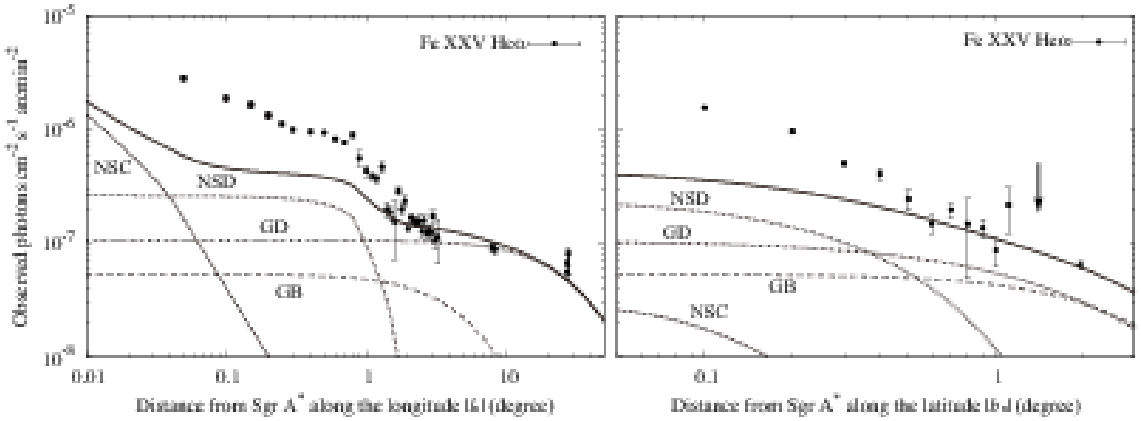

Fig. 9. Left: Flux distribution of the Fe XXV-Heα along the Galactic plane in comparison with the SMD. The thick dotted lines are the nuclear stellar cluster (NSC), the thin dotted lines are the central nuclear stellar cluster (NSD). The dot-dashed lines represent the Galactic dick (GD), while the long-dashed line is the Galactic bulge. The sum of these components is presented by the solid lines. The GCXE, GBXE and GRXE in X-rays correspond to NSD, GB and GD in infrared (SMD), respectively. Right: same as the left but perpendicular to the Galactic plane. The arrow shows the position of the CBF (section 9.1) (From Uchiyama et al. 2011).

region of $|l_*| = 0^\circ.1 - 0^\circ.6$ is $\sim$2 – 4 times larger than the prediction of the SMD model (the solid lines in figure 9). The same result, the excess of Fe XXV-Heα line above the infrared flux in the GCXE region is found in the assembly of the infrared stars obtained by the SIRIUS observations of Yasui et al. (2015).

Heard & Warwick (2013a) made the Fe-Kα line and the 7.2 – 10 keV band profile along the $b_* = 0^\circ$ and $l_* = 0^\circ$ lines in the central GCXE region ($4' - 13'$ from Sgr A*). The flux of the central GCXE region is enhanced with a sharp peak near at Sgr A*. They predicted that the 2 – 10 keV fluxes per $1 M_\odot$ at $20'$ from Sgr A* is $\sim 5 \times 10^{27}$ erg s$^{-1} M_\odot^{-1}$, while at $2'$, it is $\sim 1 \times 10^{28}$ erg s$^{-1} M_\odot^{-1}$. Taking into account of the energy band differences, these are $\sim$1.5 and $\sim$3 times larger than those of the GRXE of $(3.5 \pm 0.5) \times 10^{27}$ erg s$^{-1} M_\odot^{-1}$ (3 – 20 keV) (Revnivtsev et al. 2006a) and the solar neighborhood of $(3.1 \pm 1.1) \times 10^{27}$ erg s$^{-1} M_\odot^{-1}$ (2 – 10 keV) (Sazonov et al. 2006), respectively.

The systematic enhancement of the fluxes per $1 M_\odot$ toward Sgr A* makes the FIM approaches for the origin of the whole GCXE to be complicated. On the other hand, $\mathrm{EW_{Fe-K}}$ are almost constant in all the GCXE region, except $\mathrm{EW_{6.4}}$ in the XRNe (section 3.3), and hence the SAM approaches would be more straightforward for the origin of the whole GCXE.

Since the surface brightness of the GCXE in the iron K-shell band (6.3 – 7.1 keV) is $\sim$10 times larger than those of the GBXE and GRXE, reliable fluxes and spectra for the GCXE may be possible with XMM-Newton and even with Chandra. Therefore the SAM is reliably applied to the GCXE for the XMM-Newton and Chandra dada in addition to the Suzaku data. Heard & Warwick (2013a) fitted the XMM-Newton spectra of the central GCXE region with mCV spectra of unrealistic Fe abundance (Yuasa et al. 2012, see section 9.1). Within $9'$ from Sgr A*, Muno et al. (2004b) made the Chandra spectrum of the resolved point sources in the luminosity range of $\sim 10^{31} - 10^{33}$ erg s^{-1}. They proposed that the major component in this luminosity band is mCV. However their estimated $\mathrm{EW_{6.4}}$, $\mathrm{EW_{6.7}}$ and $\mathrm{EW_{6.97}}$ of $\sim$140 eV$\sim$400 eV, and $\sim$230 eV, respectively, are largely different from the mCV , but is rather similar to the non-mCV (table 14).

In order to examine the differences between the global GCXE spectrum and those of the XASs, Nobukawa et al. (2016) fitted the Suzaku GCXE spectrum with the combination of their 2-T models, which are made from the real observed values of the temperature, $\mathrm{EW_{Fe-K}}$ for each mCVs, non-mCVs and ABs (section 8.2). The combined 2-T model fit is completely rejected with χ^2 / d.o.f = 2637 / 276 (table 15), simply because the $\mathrm{EW_{Fe-K}}$ of the GCXE (table 5) are far larger than any of the XASs (table 14).

Large excesses in the GCXE spectrum from the combined 2-T models are found in the Fe I-Kα and Fe XXVI-Lyα lines. This indicates that the $\mathrm{EW_{6.4}}$ and $\mathrm{EW_{6.97}}$ excess over the 2-T model in the GCXE is larger than those in the GRXE (section 9.2). An important note is that the excesses of $\mathrm{EW_{6.4}}$ and $\mathrm{EW_{6.97}}$ in the GCXE are not due to the 1.5 – 3 times enhancement of the X-ray luminosity per $M_\odot$ in the GCXE relative to the GBXE and GRXE, but needs new components which exhibit larger $\mathrm{EW_{6.4}}$ and $\mathrm{EW_{6.97}}$ than any of the XASs.

The SAM results which reject the combined 2-T model fit are consistent with that the GCXE has smaller $\mathrm{SH_{Fe-K}}$ $\sim$(31 – 36) pc (calculated from the e-folding b in table 4) than those of the mCVs, non-mCVs $\sim$(130 – 160) pc and ABs $\sim$(150 – 300) pc, respectively (table 14). The $\mathrm{SH_{Fe-K}}$ of the GCXE are similar to the SH of CMZ (Tsuboi et al. 1999; Weinen et al. 2014), and hence the new components of the GCXE may be closely related to the CMZ, regardless diffuse or point sources.

The excess of the $\mathrm{EW_{6.4}}$ should be associated with the ad-

ditional non-thermal X-ray continuum. As is noted in section 3.3, Yuasa et al. (2008) found a power-law emission from the GCXE, most are due to the XRNe. Still some fractions are remained in the non-XRN regions of the GC west (e.g. Koyama et al. 2009; Uchiyama et al. 2013), which would be due to the LECR. If significant fraction of the LECR is LECRp, excess of the $EW_{6.4}$ would be obtained. Thus the $EW_{6.4}$ excess in the GCXE is an enhanced version of the the GRXE (section 8.3).

The excess of the Fe XXVI-Lyα lines requires another component, which emit stronger Fe XXVI-Lyα lines than any of the XASs. In the CMZ region of $|l| \lesssim 0.^{\circ}3$, the longitude profiles of the Fe XXV-Heα line in the east (positive l^*) shows a significant excess over the west, even excluding the bright SNR Sgr A East (Koyama et al. 2007b; Heard & Warwick 2013a). This excess would be due to larger populations of high-mass stars in the east than the west (Park et al. 2004; Muno et al. 2004a; Koyama et al. 2007b).

In the close vicinity of Sgr A*, the Fe XXV-Heα and Fe XXVI-Lyα fluxes relative to the SMD, seems to be larger than $\sim$3 times of the GRXE (Heard & Warwick 2013a). This region corresponds the Nuclear Star Cluster in the CMZ, which is a site of large population of high-mass stars. The high-mass stars may contribute to the GCXE by the putative star-burst activity and / or frequent SN explosion in the GMZ. The reconnection of strong magnetic fields, or big outbursts of Sgr A* (Inui et al. 2009; Terrier et al. 2010; Ponti et al. 2010; Capelli et al. 2012; Ryu et al. 2009; Ryu et al. 2013) (section 7) may also produce hot plasmas, responsible to the strong Fe XXVI-Lyα line. The CMZ and the close vicinity of Sgr A* are unique regions with the most extreme physical conditions than any other regions of the Galaxy. Therefore, other physical processes, beyond our current views of the quiet Galactic regions, may be concealable.

In summary, the FIMs did not explain the full flux of the GCXE by XASs. The SAM result leave significant excess of $EW_{6.4}$ and $EW_{6.97}$ over any combination of the XAS spectra. Thus, either diffuse or new type point source are required in the GCXE. These should have larger $EW_{6.4}$ and $EW_{6.97}$ and smaller SH_{Fe-K} than any of the XASs.

Acknowledgments

The author expresses his sincere thanks to all the members of $KyotoSchool$ for their efficient works, valuable comments and many helps on the study of the Galactic diffuse X-rays. Particular thanks are due to M. Nobukawa and S. Yamauchi for their great efforts for preparing this draft. This work is supported by JSPS and MEXT KAKENHI Grant Number 24540229.

References

Aharonian, F., et al. 2008, A&A, 483, 509

Ak, T., Bilir, S., Ak, S., & Eker, Z. 2008, New Astronomy, 13, 133

Anders, E., & Grevesse, N. 1989, Geochimica et Cosmochimica Acta, 53, 197

Baganoff, F. K., et al. 2003, ApJ, 591, 891

Bamba, A., Yokogawa, J., Sakano, M., & Koyama, K. 2000, PASJ, 52, 259

Bamba, A., Yamazaki, R., Kohri, K., Matsumoto, H., Wagner, S., Puhlhofer, G., & Kosack, K. 2009 ApJ, 691, 1854

Beiersdorfer, P., Phillips, T. W., Wong, K. L., Marrs, R. E., & Vogel, D. A. 1992, Phys. Rev. A, 46, 3812

Beiersdorfer, P., Phillips, T., Jacobs, V. L., Hill, K. W., Bitter, M., von Goeler, S., & Kahn, S. M. 1993, ApJ, 409, 846

Benson, J. M.,& Johnston, K. J. 1984, ApJ, 277, 181

Capelli, R., Warwick, R. S., Cappelluti, N., Gillessen, S., Predehl, P., Porquet, D.,& Czesla, S. 2011a, A&A, 525, 2

Capelli, R., Warwick, R. S., Porquet, D., Gillessen, S., & Predehl, P. 2011b, A&A, 530, 38

Capelli, R., Warwick, R. S., Porquet, D., Gillessen, S., & Predehl, P. 2012, A&A, 545, 35

Clavel, M., Terrier, R., Goldwurm, A., Morris, M. R.; Ponti, G., Soldi, S., & Trap, G. 2013, A&A, 558A, 32

Clavel, M., Soldi, S., Terrier, R., Tatischeff, V., Maurin, G., Ponti, G., Goldwurm, A.,& Decourchelle, A. 2014, MNRAS, 443, 129

Cooke, B. A., Griffiths, R. E., & Pounds, K. A. 1969, Nature, 224, 134

Cunha, K., Sellgren, K., Smith, V. V., et al. 2007, ApJ, 669, 1011

Dobler, G., Finkbeiner, D. P., Cholis, I., Slatyer, T., & Weiner, N. 2010, ApJ,717, 825

Dogiel, V., Chernyshov, D., Koyama, K., Nobukawa, M., Cheng, K. -S. 2011, PASJ, 63, 535

Downes, D., Goss, W. M., Schwarz, U. J., & Wouterloot, J. G. A. 1979, A&AS, 35, 1

Downes, D., & Maxwell, A. 1966, ApJ, 146, 653

Ebisawa, K., Maeda, Y., Kaneda, H., & Yamauchi, S. 2001, Science, 293, 1633

Ebisawa, K., et al. 2005, ApJ, 635, 214

Ebisawa, K., et al. 2008, PASJ, 60, 223

Ekers, R. D., van Gorkom, J. H., Schwarz, U. J., & Goss, W. M. 1983, A&A 122, 143

Forman, W., Jones, C., Cominsky, L., Julien, P., Murray, S., Peters, G., Tananbaum, H., & Giacconi, R. 1978, ApJS, 38, 357

Fukuoka, R., Koyama, K., Ryu, S. G., & Tsuru, T. G. 2009, PASJ, 61, 593

Genzel, R. Eisenhauer, F., & Gillessen, S. 2010, Rev. Mod. Phys, 82, 3121

Giacconi, R., Gursky, H., Paolini, F. R., & Rossi, B. B. 1962, PhRvL, 9, 439

Hangs, A. D. P., Warwick, R., Watson, M. G., & Helfand, D. J. 2013a, MNRAS, 351, 31

Heard, V., & Warwick, R. S. 2013a, MNRAS, 428, 3462

Heard, V., & Warwick, R. S. 2013b, MNRAS, 434, 1339

Hertz, P., & Grindlay, J. E. 1984, ApJ, 278, 137

Hirano, T., Hayakawa, S., Nagase, F., Masai, K., & Mitsuda, K. 1987, PASJ, 39, 619

Hong, J. S., van den Berg, M., Grindlay, J. E., & Laycock, S. 2009, ApJ, 706, 223

Hong, J. S. 2012, MNRAS, 427, 1633

Inui, T., Koyama, K., Matsumoto, H., & Tsuru, T. G. 2009, PASJ, 61, 241

Iwan, D., Shafer, R. A., Marshall, F. E., Boldt, E. A., Mushotzky, R. F., & Stottlemyer, A. 1982, ApJ, 260, 111

Jean, P., Knödlseder, J., Gillard, W., Guessoum, N., Ferrière, K.,

Marcowith, A., Lonjou, V., & Roques, J. P. 2006, A&A, 445, 579
Johnson, S. P., Dong, H. & Wang, Q. D. 2009, MNRAS, 399, 1429
Kaneda, H., Makishima, K., Yamauchi, S., Koyama, K., Matsuzaki, K., & Yamasaki, N. Y. 1997, ApJ, 491, 638
Kataoka, J., et al. 2013, ApJ, 779, 57
Kawai, N., Fenimore, E. E., Middleditch, J., Cruddace, R. G., Fritz, G. G., Snyder, W. A.,& Ulmer, M. P. 1988, ApJ, 330, 130
Kendrew, S., Ginsburg, A., Johnston, K., Beuther, H., Bally, J., Cyganowski, C. J., & Battersby, C.2013, ApJ, 775, 50.
Kellogg, E., Gursky, H., Murray, S., Tananbaum, H., & Giacconi. R. 1971, ApJL, 169, 99
Koyama, K., Makishima,K., Tanaka,Y., & Tsunemi, H. 1986a, PASJ, 38, 121
Koyama, K., Ikeuchi, S., & Tomisaka, K. 1986b, PASJ, 38, 503
Koyama, K. 1989, PASJ, 41, 665
Koyama, K., Awaki, H., Kunieda, H., Takano, S., Tawara, Y., Yamauchi, S. Hatsukade, I.,& Nagase, F. 1989, Nature, 339, 603
Koyama, K., Maeda, Y., Sonobe, T., Takeshima, T., Tanaka, Y., & Yamauchi, S.1996, PASJ, 48, 249
Koyama, K., Senda, A., & Murakami, H. 2004, Progress of Theoretical Physics Supplement, 155, 152
Koyama, K., et al. 2007a, PASJ, 59, 221
Koyama, K., Uchiyama, H., Hyodo, Y., Matsumoto, H., Tsuru, T. G., Ozaki, M., Maeda, Y., & Murakami, H. 2007b, PASJ, 59, 237
Koyama, K., et al. 2007c, PASJ, 59, 245
Koyama, K., Inui, T., Matsumoto, H., & Tsuru, T. G. 2008, PASJ, 60, 201
Koyama, K., Takikawa, Y., Hyodo, Y., Inui, T., Nobukawa, M., Matsumoto, H., & Tsuru, T. G. 2009, PASJ, 61, 255
Koyama, K. 2014 , efxu.conf, 2
Krivonos, R. A., et al. 2014, ApJ, 781, 107
LaRosa, T. N., Kassim, N. E., Lazio, T. J. W., & Hyman, S. D. 2000, AJ, 119, 207
Law, C., & Yusef-Zadeh, F. 2004, ApJ, 611, 585
Li, Z., Morris, M. R., & Baganoff, F. K., 2013, ApJ, 779, 154
Lu, F. J., Wang, Q. D., & Lang, C. C. 2003, AJ, 126, 319
Lu, F. J., Yuan, T. T., & Lou,Y. -Q. 2008, AJ, 673, 915
Maeda, Y., et al. 2002, ApJ, 570, 671
Mirabel, I. F., Rodriguez, L. F., Cordier, B., Paul, J., & Lebrun, F. 1992, Nature, 358, 215
Mori, H., Tsuru, T. G., Hyodo, Y., Koyama, K., & Senda, A., 2008, PASJ, 60, 183
Mori, H., Hyodo, Y., Tsuru, T. G., Nobukawa, M., & Koyama, K. 2009, PASJ, 61, 687
Mori, K., et al. 2015, ApJ, 814, 94
Morihana, K., Tsujimoto, M., Yoshida, T., & Ebisawa, K. 2013, ApJ, 766, 14
Morris, M. R., Meyer, L., & Ghez, A. M. 2012, Research in Astronomy and Astrophysics, 12, 995
Mukai, K., & Shiokawa, K. 1993, ApJ, 418, 863
Muno, M. P., et al. 2003, ApJ, 589, 225
Muno, M. P., Baganoff, F. K., Bautz, M. W., Feigelson, E. D., Garmire, G. P., Morris, M. R., Park, S., Ricker, G. R., & Townsley, L. K. 2004a, ApJ, 613, 326M
Muno, M. P., et al. 2004b, ApJ, 613, 1179
Muno, M. P., Baganoff, F. K., Brandt, W. N., Park, S., & Morris, M. R. 2007, ApJ 656, 69
Muno, M. P., Baganoff, F. K., Brandt, W. N., Morris, M. R., & Starck, J-.L. 2008, ApJ, 673, 251
Murakami, H., Koyama, K., Sakano, M., Tsujimoto, M., & Maeda, Y. 2000, ApJ, 534, 283
Murakami, H., Koyama, K., Tsujimoto, M., Maeda, Y., & Sakano, M. 2001a, ApJ, 550, 297
Murakami, H., Koyama, K., &, Maeda, Y. 2001b, ApJ, 558, 687
Nakajima, H., Tsuru, T. G., Nobukawa, M., et al. 2009, PASJ, 61, 233
Nakashima, S., Nobukawa, M., Tsuru, T., Koyama, K., & Uchiyama, H. 2010, PASJ, 62, 971
Nakashima, S., Nobukawa, M., Uchida, H., et al. 2013, ApJ, 773, 20
Nobukawa, M., et al. 2008, PASJ, 60, S191
Nobukawa, M., Koyama, K., Tsuru, T. G., Ryu, S. G., & Tatischeff, V. 2010, PASJ, 62, 423
Nobukawa, M., Ryu, S. G., Tsuru, T. G., & Koyama, K. 2011, ApJL, 739, L52
Nobukawa, K. K., Nobukawa, M., Uchiyama, H., Tsuru, T. G., Torii, K., Tanaka, T., Chernyshov, D. O., Fukui, Y., Dogiel, V. A., & Koyama, K. 2015. ApJ, 807L, 10
Nobukawa, M., Nobukawa, K. K., Uchiyama, H.,Yamauchi, S., & Koyama, K. 2016, ApJ, 833, 268
Nobukawa, M., 2017, in preparation
Nobukawa, K. K., 2017, in preparation
Nynka, M., et al. 2013, ApJ 778, 31
Nynka, M., et al. 2014, ApJ 784, 6
Nynka, M., et al. 2015, ApJ 800, 119
Odaka, H., Aharonian, F., Watanabe, S., Tanaka, Y., Khangulyan, D., & Takahashi, T. 2011, ApJ, 740, 103
Ohnishi, T., Koyama, K., Tsuru, T., Masai, K., Yamaguchi, H., & Ozawa, M. 2011, PASJ, 63, 527
Oka, T., Hasegawa, T., Sato, F., Tsuboi, M., & Miyazaki, A. 2001, PASJ, 53, 779
Ozawa, M., Koyama, K., Yamaguchi, H., Masai, K., & Tamagawa, T. 2009, ApJL, 706, L71
Park, S., Muno, M. P., Baganoff, F. K., Maeda, Y., Morris, M., Howard, C., Bautz, Mark. W., & Garmire, G. P. 2004, ApJ, 603,548
Park, S., et al. 2005, ApJ, 631, 964
Patterson, J. 1984, ApJS, 54, 443
Perez, K. et al. 2015, Nature, 520, 646
Ponti, G., Terrier, R., Goldwurm, A., Belanger, G., & Trap, G. 2010, ApJ, 714, 732
Ponti, G., et al. 2015, MNRAS, 453, 172
Porquet, D., Predehl, P., Aschenbach, B., Grosso, N., Goldwurm, A., Goldoni, P., Warwick, R. S., & Decourchelle, A. 2003, A&A, 407L, 17 5
Porquet, D., et al. 2008, A&A, 488, 549
Predehl, P., & Truemper, J. 1994, A & A, 290, 29
Proctor, R. J., Skinner, G. K., & Willmore, A. P. 1978, MNRAS, 185, 745
Protheroe, R. J., Wolfendale, A. W., & Wdowczyk, J. 1980, MNRAS, 192, 445
Renaud, M., Paron, S., Terrier, R., Lebrun, F., Dubner, G., Giacani, E., & Bykov, A. M. 2006, ApJ, 638, 220
Revnivtsev, M. 2003, A&A, 410, 865
Revnivtsev, M. G., et al. 2004, A&A, 425, L49
Revnivtsev, M. G. , Sazonov, S., Gilfanov, M., Churazov, E., & Sunyaev, R. 2006a, A&A, 452, 169
Revnivtsev, M. G., Molkov, S., & Sazonov, S. 2006b, MNRAS, 373, L11
Revnivtsev, M. G., & Sazonov, S. 2007a, A&A, 471, 159
Revnivtsev, M. G,, Vikhlinin, A., & Sazonov, S. 2007b, A&A, 473, 857
Revnivtsev, M. G., Sazonov, S., Churazov, E., Forman, W., Vikhlinin, A.,

& Sunyaev, R. 2009, Nature, 458, 1142
Revnivtsev, M. G., & Molkov, S. V. 2012, MNRAS, 424, 2330
Rho, J., & Petre, R.1998, ApJL, 503, 167
Roberts, M. S. E., Romani, R. W., & Kawai, N. 2001, ApJS, 133, 451
Ryu, S. G., Koyama, K., Nobukawa, M., Fukuoka, R., & Tsuru, T. G. 2009, PASJ, 61, 751
Ryu, S. G., Nobukawa, M., Nakashima, S., et al. 2013, PASJ, 65, 33
Sakano, M., Koyama, K., Murakami, H., Maeda, Y., & Yamauchi, S. 2002, ApJS, 138, 19
Sakano, M., Warwick, R. S., Decourchelle, A., & Predehl, P. 2003, MNRAS, 340, 747
Sakano, M., Warwick, R. S., Decourchelle, A., & Predehl, P. 2004, MNRAS, 350, 129
Sakano, M., Warwick, R. S., & Decourchelle, A. 2006, JPhCS, 54, 133
Sato, T., Koyama, K., Takahashi, T., Odaka, H., & Nakashima, S. 2014, PASJ, 66, 124
Sato, T., Koyama, K., Lee, S-H., & Takahashi, T. 2016, PASJ, 68, 8
Sawada, M., Tsujimoto, M., Koyama, K., Law, C. J., Tsuru, T. G., & Hyodo, Y. 2009, PASJ, 61, 209
Sazonov, S., Revnivtsev, M., Gilfanov, M., Churazov, E., & Sunyaev, R. 2006, A&A, 450, 117
Senda, A., Murakami, H., & Koyama, K. 2002, ApJ, 565, 1017
Sidoli, L., Mereghetti, S. A. Treves, A., Parmar, A. N., Turolla, R., & Favata,F. 2001, A&A 372, 651
Skinner, G. K., Willmore, A. P., Eyles, C. J., Bertram, D., & Church, M. J. 1987, Nature, 330, 544
Sofue, Y. 2000, ApJ, 540, 224
Strassmeier, K. G., Hall, D. S., Fekel, F. C., & Scheck, M. 1993, A&AS, 100, 173
Su, M., Slatyer, T. R., & Finkbeiner, D. P. 2010, ApJ, 724, 1044
Sunyaev, R., et al. 1991, ApJ, 383, L49
Sunyaev, R. A., Markevitch, M., & Pavlinsky, M. 1993, ApJ, 407, 606
Sunyaev, R., & Churazov, E. 1998, MNRAS, 297, 1279
Takagi, S., Murakami, H., & Koyama, K. 2002, ApJ, 573, 275
Tanaka, Y., Koyama, K., Maeda, Y., & Sonobe, T. 2000, PASJ, 52, 25
Tanaka, Y. 2002, A&A, 382, 1052
Tatischeff, V., Decourchelle, A., & Maurin, G. 2012, A&A, 546A, 88
Terrier, R., Ponti, G., Bélanger, G., et al. 2010, ApJ, 719, 143
Totani, T. 2006, PASJ, 58, 965
Tsuboi, M., Ukita, N., & Handa, T. 1997, ApJ, 481, 263
Tsuboi, M. Handa, T., & Ukita, N. 1999, ApJS, 120, 1
Tsujimoto, M., Hyodo, Y., & Koyama, K. 2007, PASJ, 59, 229
Tsuru, T. G., Nobukawa, M., Nakajima, H., Matsumoto, H., Koyama, K., & Yamauchi, S. 2009, PASJ, 61, S219
Uchiyama, H., Nobukawa, M., Tsuru, T., Koyama, K., & Matsumoto, H. 2011, PASJ, 63, 903
Uchiyama, H., Nobukawa, M., Tsuru, T. G., & Koyama, K. 2013, PASJ, 65, 19
Uchiyama, H., et al. 2017, private communication
Valinia, A., & Marshall, F. E. 1998, ApJ, 505, 134
Valinia, A., Tatischeff, V., Arnaud, K., Ebisawa, K., & Ramaty, R. 2000, ApJ, 543, 733
Wang, Q., Gotthelf, E. V., & Lang, C. C. 2002a, Nature, 415, 148
Wang, Q. D., Lu, F., & Lang, C. C. 2002b, ApJ, 581, 1148
Wang, Q. D., Lu, F. J., & Gotthelf, E. V. 2006a, MNRAS, 367, 937
Wang, Q. D., Dong, H., & Lang, C. 2006b, MNRAS, 371, 38
Wargelin, B. J., Beiersdorfer, P., Neill, P. A., Olson, R. E., & Scofield, J. H. 2005, ApJ, 634, 687
Warwick, R. S., Pye, J. P., & Fabian, A. C. 1980, MNRAS, 190, 243
Warwick, R. S., Turner, M. J. L., Watson, M. G., & Willingale, R. 1985, Nature, 317, 218
Warwick, R. S., Byckling, K., & Pérez-Ramírez, D. 2014a, MNRAS, 438, 2967
Warwick, R. S. 2014, MNRAS, 445, 66
Washino, R., Uchida, H., Nobukawa, M., Tsuru, T. G., Tanaka, T., Kawabata, N. K., & Koyama, K. 2016, PASJ, 68, 4
Watson, M. G., Willingale, R., Hertz, P.,& Grindlay, J. E. 1981, ApJ, 250, 142
Weidenspointner, G., Skinner,. G.K., Jean. P., et al. 2008, New Astronomy, 52, 454
Weinen. M., et al. 2015, A&A 579, 91
Worrall, D. M., Marshall, F. E., Boldt, E. A., & Swank, J. H. 1982, ApJ, 255, 111
Worrall, D. M., & Marshall, F. E. 1983, ApJ, 267, 691
Xu, X., Wang, Q. D., & Li, X. 2016, ApJ, 818, 136
Yamaguchi, H., Ozawa, M., Koyama, K., Masai, K., Hiraga, J. S., Ozaki, M., & Yonetoku, D. 2009, ApJ, 705, 6
Yamasaki, N. Y., Ohashi, T., Takahara, F.; Yamauchi, S., Kamae, T., Kaneda, H., Makishima,K., & Koyama, K. 1996, A&AS, 120, 393
Yamasaki, H., et al. 1997, ApJ, 481, 821
Yamauchi, S., Kawada, M., Koyama, K., Kunieda, H., & Tawara, Y. 1990, ApJ, 365, 532
Yamauchi, S.,& Koyama, K. 1993, ApJ, 404, 620
Yamauchi, S.,& Koyama, K. 1995, PASJ, 47, 439
Yamauchi, S., Kaneda, H., Koyama, K., Makishima, K., Matsuzaki, K., Sonobe, T., Tanaka, Y., & Yamasaki, N. 1996, PASJ, 48, 15
Yamauchi, S., Ebisawa, K., Tanaka, Y., et al. 2009, PASJ, 61, 225
Yamauchi, S., Shimizu, M., Nakashima, S., Nobukawa, M., Tsuru, T. G., & Koyama, K. 2014, PASJ, 66, 125
Yamauchi, S., Nobukawa, K. K., Nobukawa, M., Uchiyama, H., & Koyama, K. 2016, PASJ, 68, 59
Yasui, K., et al. 2015, PASJ, 67, 123
Yuasa, T., et al. 2008, PASJ, 60, 207
Yuasa, T., Makishima, K., & Nakazawa, K. 2012, ApJ, 753, 129
Yusef-Zadeh, F., Wardle, M., & Parastaran, P. 1997, ApJL, 475, L119
Yusef-Zadeh, F., Law, C., & Wardle, M. 2002a, ApJL, 568, L121
Yusef-Zadeh, F., Law, C., Wardle, M. Wang, Q. D., Fruscione, A., Lang, C. C., & Cotera, A. 2002b, ApJ, 570, 665
Yusef-Zadeh, F., Hewitt, J. W., & Cotton, W. 2004, ApJS, 155, 421
Yusef-Zadeh, F., Wardle, M., Muno, M., Law, C., & Pound, M. 2005, Advances in Space Research, 35, 1074
Yusef-Zadeh, F., Muno, M. Wardle, M., & Lis, D. C. 2007, ApJ, 656, 847
Zhang, S., et al. 2014, ApJ, 784, 6
Zhang, S., et al. 2015 ApJ 815, 132